学位論文

Giant Molecular Cloud Formation at the Interface of Colliding Supershells in the Large Magellanic Cloud

(大マゼラン雲におけるシェル衝突面での巨大分子雲形成　)

東京大学大学院理学系研究科
天文学専攻
藤井　浩介

平成 27 年 12 月 博士 (理学) 申請

Abstract

Giant molecular clouds (GMCs) are the principle site of the stellar cluster formation. Understanding the formation and the evolution of the GMCs are quite important to get a general understanding of the evolution of galaxies from the Local Group to the most distant Universe. Recent theoretical works of the GMC formation have argued that the filamentary GMCs formed at the stagnation point of the converging flows that are driven by supersonic turbulence and/or interstellar shocks. Compared to the observational works of the evolution of the GMCs, however, there is almost no observational work targeted on the kinematics of the GMC formation. Case studies that can prove theoretical predicts are now aspired.

Large Magellanic Cloud (LMC) is the nearest external galaxy (distance $\sim$ 50 kpc) and is relatively face-on to us (inclination $\sim$35°). It has a large population of super-bubbles and supergiant shells (SGSs) in its gaseous disk. Star-forming regions N48 and N49 are located at the high column density H I ridge between two kpc-scale SGSs, LMC 4 and LMC 5. Young massive GMCs ($> 10^6$ $M_\odot$), which is considered to be formed by the collision of two SGSs, are identified without any signs of massive cluster formation. The GMCs in the N48 and N49 is the one of the best target to investigate the GMC formation process via large-scale colliding flows driven by the SGSs. In this thesis, high-resolution observation of the atomic Hydrogen (H I) gas is performed towards the H I ridge, and the GMC formation process at the colliding area of the two SGSs are studied from the analysis of the large-scale kinematics of the H I gas.

Before analyzing the H I gas, the detailed structure of the GMCs are investigated by the ASTE and Mopra observation. With 7 pc spatical resolution of ASTE, it is revealed that the GMCs consists of a lot of envelope-less dense molecular clumps of $\sim$ 10 pc diameter within a characteristic separation of $\sim$ 40 pc. The N48 region is located in the high column density H I envelope at the interface of the two SGSs and the star formation is relatively evolved, whereas the N49 region is associated with LMC 5 alone and the star formation is quiet. The clumps in the N48 region typically show higher $n(H_2)$ ($\sim 2 \times 10^3$ cm^{-3}) and $T_{\rm kin}$ ($\sim$ 100 K) than the N49 clumps. The N48 clumps are more evolved than the N49 clumps but still in the early phase of cluster formation.

New H I 21 cm line observation is performed toward the ridge using Australia Telescope Compact Array (ATCA) with 1.5 km baseline configurations. The obtained data is combined with the archival shorter baseline data (Mao et al.), and the archival single dish data of Parkes telescope. Achieved beam size is 24.75″ by 20.48″, which corresponds to spatial resolution of $\sim$ 6 pc in the LMC, which is comparable to the ASTE resolution, and is quite high for the 21 cm line observation in the external galaxy. With this high-resolution observation, it is newly revealed that the structure of H I gas is highly filamentary, and the molecular clumps are distributed along the filamentary H I. From the channel maps of the new H I data, the identification of the filamentary features are performed by chaining the H I cores that are identified by the dendrogram. In total 39 filamentary features are identified, which implies that the H I gas structure of the ridge mainly consists of the composition of the filamentary features. Typical

width of the filamentary features is $\sim$ 21 (8–49) [pc], and the typical line mass is $\sim$ 90 (20–190) [$M_\odot$/pc]. Since the molecular clumps are found in the most prominent filamentary feature, the evolution of the filamentary features might lead to the formation of the molecular clumps.

The H I position velocity diagram perpendicular to the ridge show that the axi-symmetric, ellipse-like distribution at the colliding area of the shells (N48 region), and the molecular clouds are found at their central part. This is one suggestive evidence that the large-scale kinematics of H I gas around the GMCs are now gravitationally evolving. The characteristic separation and the typical mass of the N48 clumps ($\sim$ 40 pc, $\sim$ 2×10^4 $M_\odot$) can be explained by the Jeans length and the Jeans mass with theoretically predicted densities of shell-shocked atomic medium ($\sim$ 30–120 cm^{-3}). The mass of the GMCs and the molecular clumps can be doubled by the accretion of the H I envelope within 10^7 years. These suggests that the H I envelope of the GMCs are gravitationally bound, and the accretion of the H I is now non-negligible, even in the size scale of the molecular clumps.

Proposed formation scenarios of the GMCs in the N48 and N49 regions can be suggested as follows both in a large-scale and a high-resolution scale. At first in the large-scale, the expansion and the collision of the two SGSs aggregate and compress the diffuse medium into the high column density ridge. Secondly, the clumpy GMCs are formed via the instability induced by the shocks of the shells and their collision. And currently the H I gas surrounding the GMCs is getting to gravitationally bound to the GMCs and accretes onto them until the stellar cluster formation starts. On the other hand in the high-resolution scale, the structure of the H I gas is getting highly filamentary during its evolution. The molecular clumps are formed along the evolved filamentary H I gas. The H I gas around the molecular clumps are also getting to bound to the clumps, and the H I accretion onto the clumps are now non-negligible. These agree well with the theoretical predicts insisting that several times shocks are required to form GMCs, and newly suggest that the GMCs formation involves filamentary nature of the atomic medium and the gravitationally bound H I envelopes around the formed GMCs.

Contents

Chapter 1

Introduction

1.1 Giant Molecular Clouds and Star Formation

1.1.1 Star Formation Life Cycle

The universe consists of tremendous numbers of galaxies. The galaxy consists of the stars and the interstellar medium (ISM). A life of a single star begins from a dense core of the ISM. If the pre-stellar core is getting massive enough by the accretion of the surrounding matters, it starts to shine as a star by the nuclear fusion, that is, by conversing the atomic Hydrogen to the atomic Helium at its center. As the stars evolve, they lose their mass into the ISM. Most drastic mass loss occurs at their death. For the low mass stars that are similar to the sun, they lives more than 10 billion years and ejects the most of their outer layer into the ISM at their death. For the massive stars that is more than eight times heavier than the sun, they finish their main sequence in tens of million years and finally explodes as the supernova with ejecting a large amount of energy into the ISM. The supernova explosion also supplies heavy elements to the ISM and promote the chemical evolution of the galaxy. In the end the all stars give back to the ISM, which is the materials of the next generation stars. The galaxies are considered to evolve through this life cycle of the stars. These are why the study of the formation of the stars are quite important as an elementary step of understanding the evolution of the galaxies, and eventually the evolution of the universe.

The first step of the star formation is accumulation of the diffuse ambient ISM into rather dense and cold clouds. Such dense clouds of gas are the predecessor of the all stars in the galaxy. How the clouds of gas is formed from the ISM and evolved in the galaxy are the most basic questions of the study of the ISM. In this thesis, this basic step is focused on. As an introduction of the study, the fundamentals of the ISM and the clouds of gas are summarized in the following subsections.

1.1.2 Atomic Medium

Although materials that can be seen in our everyday life are consisted of variety of atomics and molecules, in the scale of the solar system or the entire universe, the Hydrogen gas is the dominant component. Typical mass abundance ratio of the universe is 74% of Hydrogen gas, 25% of Helium gas, and remaining 1% of other materials. In the Milky Way galaxy and the nearby galaxies, the majority of Hydrogen gas exist as constituent material of stars. A few to 10% mass of Hydrogen gas is distributed in the disk of typical spiral galaxies as interstellar gas. Half of them are atomic Hydrogen gas, and the others are molecular Hydrogen gas. At first in this subsection, the characteristics of interstellar atomic Hydrogen gas are summarized. And then the characteristics of interstellar molecular gas and molecular clouds are mentioned.

Radiation Mechanism of Atomic Hydrogen

Single atomic Hydrogen consists of one proton and one electron. Both particles are fermion, and have spin with spin angular momentum of $s = 1/2$. If each spin is in the same direction, the proton and the electron repel each other and the energy state is high. If the spin is in the opposite direction, the system is stable and the energy state is low (ground state). When the spin direction changes from parallel to anti-parallel, atomic Hydrogen emits an electromagnetic wave with the frequency (or wavelength) corresponds to the energy difference of two state, $E = h\nu$. Here h is Planck constant. The wavelength and the frequency are as follows,

$$\begin{aligned} \lambda &= 21.106114 \text{ cm}, \\ \nu &= 1420.405751786 \text{ MHz}. \end{aligned}$$

This emission line of Hydrogen is often called as "*hydrogen line*" or "*21 centimeter line*". 21 centimeter line was predicted in 1944 by Hendrik Christoffel van de Hulst, who is an astronomer in Holland, and was first detected in 1951 by Harold Irving Ewen and Edward Mills Purcell at Harvard University. The rest frequency of 1.4 GHz is in the radio frequency band, corresponding beam size is quite large even in a extremely large antenna ($\lambda/D \sim 7'$ for $D = 100$ m). However, deu to the loose restriction of the long wavelength band observation with large beam on a surface accuracy, pointing accuracy, and a low noise amplifier, a lot of large radio telescopes and arrays have targeted this frequency band from the early phase of the radio astronomy.

The transition of two state of the Hydrogen is a forbidden transition, and thus 21 centimeter line is a forbidden line. Here the higher energy state with parallel spin is described as subscript "u", and the lower energy state with anti-parallel spin is described as subscript "l". In the case of Hydrogen, Einstein A coefficient, which represents the probability of spontaneous transition, is

$$A_{\rm ul} = \frac{64\pi^4\nu^3}{3hc^3} \left|\mu_{\rm ul}\right|^2 = 2.86888 \times 10^{-15} \ [\mathrm{s}^{-1}]. \tag{1.1.1}$$

Here, $\mu_{\rm ul}$ is the magnetic moment of the atomic Hydrogen and has the value of $|\mu_{\rm ul}|^2 = 8.6\times10^{-41}$ erg^2 G^{-2}. The reciprocal of $A_{\rm ul}$ corresponds to the timescale of spontaneous transition of spin reversal, $t \sim A_{\rm ul}^{-1} \sim 10^7$yr, which is too long to see this transition for the single atomic Hydrogen. On the other hand, the probability of atomic Hydrogen colliding each other in the interstellar gas can be expressed as follows;

$$C \sim n({\rm H\,I})\sigma({\rm H\,I})\,\langle v\rangle \tag{1.1.2}$$

$$\sim 1.5\times10^{-11}\left(\frac{n}{1\ [{\rm cm^{-3}}]}\right)\left(\frac{T_k}{100\ [{\rm K}]}\right)^{1/2}\ [{\rm s^{-1}}]. \tag{1.1.3}$$

Here, $n({\rm H\,I})$ is number density of atomic Hydrogen, $\sigma({\rm H\,I})$ is the collision cross section of the atomic Hydrogen, and $\langle v\rangle$ is the average velocity of the thermal motion of the atomic Hydrogen. Here the parameters are normalized by the typical density and the temperature of the interstellar atomic Hydrogen, $n({\rm H\,I}) \sim 1$ cm^{-3} and $T_k \sim 100$ K. Typical timescale of the collision can be estimated from the reciprocal of the collision probability, $t_{\rm col} \sim C^{-1} \sim 2\times10^3$ yr, which is much smaller than the spontaneous transition timescale. Assuming that the radiation field is not unusually high (a good assumption for the most interstellar environments), the excitation of atomic Hydrogen is mainly due to the collision of two atomic Hydrogen with the thermal motion, and then the interstellar atomic Hydrogen gas is roughly in the thermal equilibrium state.

Derivation of Physical Parameters of Atomic Hydrogen Gas : Optically Thin Case

With an assumption of optically thin condition of H I gas for 21 cm line emission (optical depth $\tau_\nu < 1$), the line of sight column density (surface density) of H I gas can be derived from the observed line intensity (but dense part of atomic Hydrogen cloud is typically optically thick. See §1.1.2.). Here the parameters of the number density of the upper state atomic Hydrogen per unit volume $n_{\rm u}$, and that of the lower state as $n_{\rm l}$ are introduced. When the atomic Hydrogen emits 21 cm line emission isotropically toward whole solid angle 4π from unit volume dV, consider the emission energy per unit solid angle $d\Omega$ and unit time dt. Here line profile function $\phi(\nu)$ should be applied because the frequency of line emission is shifted due to proper and thermal motion of each atomic Hydrogen. Note that $\int\phi(\nu)d\nu = 1$, and the number density of atomic Hydrogen which can emit line with frequency of ν can be described as $n_\nu = n\phi(\nu)$.

Emission energy of spontaneous transition can be written as

$$dE_e = h\nu n_{\rm u}\phi(\nu)A_{\rm ul}\,dV\frac{d\Omega}{4\pi}dt. \tag{1.1.4}$$

For 21 cm line, ν equals to 1420 MHz, and $A_{\rm ul}$ is given in Eq. (1.1.1), which is an Einstein A coefficient representing a probability of spontaneous transition of two spin state of atomic Hydrogen.

Besides spontaneous emission, it is necessary to consider self absorption and stimulated radiation of 21 cm line with local radiation intensity I_ν. These effects can be

estimated by introducing Einstein B coefficient of $B_{\rm lu}$ for absorption, and $B_{\rm ul}$ for stimulated radiation. With local energy density $u_\nu = \frac{4\pi}{c} I_\nu$, $B_{\rm lu} u_\nu$ represents the transition probability per unit time for absorption, and $B_{\rm ul} u_\nu$ represents the transition probability per unit time for stimulated emission. Then the absorbed energy of atomic Hydrogen from local radiation intensity I_ν with whole solid angle can be written as

$$dE_a = h\nu n_{\rm l} \phi(\nu) B_{\rm lu} \frac{4\pi}{c} I_\nu \, dV \frac{d\Omega}{4\pi} dt, \tag{1.1.5}$$

and energy of stimulated emission with local radiation I_ν is

$$dE_s = h\nu n_{\rm u} \phi(\nu) B_{\rm ul} \frac{4\pi}{c} I_\nu \, dV \frac{d\Omega}{4\pi} dt. \tag{1.1.6}$$

Then the output intensity I_ν can be expressed as

$$I_\nu \phi(\nu) \, d\Omega \, d\sigma \, d\nu \, dt = dE_{\rm e} + dE_{\rm s} - dE_{\rm a}, \tag{1.1.7}$$

where $d\sigma$ is cross sectional area of unit volume dV toward solid angle $d\Omega$. When $dV = d\sigma dx$ and $I_\nu \phi(\nu) d\nu = dI_\nu$, radiative transfer equation can be expressed with Einstein coefficients,

$$\frac{dI_\nu}{dx} = \frac{h\nu}{c} (n_{\rm u} B_{\rm ul} - n_{\rm l} B_{\rm lu}) \phi(\nu) I_\nu + \frac{h\nu}{4\pi} n_{\rm u} A_{\rm ul} \phi(\nu). \tag{1.1.8}$$

Remember the basic expression of radiative transfer equation,

$$\frac{dI_\nu}{dx} = -\kappa_\nu I_\nu + \epsilon_\nu, \tag{1.1.9}$$

where κ_ν and ϵ_ν is absorption coefficient and emission coefficient per unit volume, respectively. And then compare Equations (1.1.8) and (1.1.9), absorption and emission coefficient can be written with Einstein coefficients,

$$\kappa_\nu = \frac{h\nu}{c} (n_{\rm u} B_{\rm ul} - n_{\rm l} B_{\rm lu}) \phi(\nu) \tag{1.1.10}$$

$$\epsilon_\nu = \frac{h\nu}{4\pi} n_{\rm u} A_{\rm ul} \phi(\nu). \tag{1.1.11}$$

It is known that there is a relationship between the Einstein coefficients,

$$g_{\rm l} B_{\rm lu} = g_{\rm u} B_{\rm ul} = \frac{c^3}{8\pi h \nu^3} g_{\rm u} A_{\rm ul}. \tag{1.1.12}$$

And here the atomic Hydrogen gas is in thermal equilibrium and the population of each state can be expressed by Boltzmann distribution,

$$\frac{n_{\rm u}}{n_{\rm l}} = \frac{g_{\rm u}}{g_{\rm l}} \, e^{h\nu / kT_{\rm s}}. \tag{1.1.13}$$

Using these two relations with approximation formula of Boltzmann distribution for $h\nu/kT_\mathrm{s} \ll 1$ ($h\nu/kT_\mathrm{s}$ is on the order of 10^{-4} for 21 cm),

$$\frac{n_\mathrm{u}}{n_\mathrm{l}} \sim \frac{g_\mathrm{u}}{g_\mathrm{l}}(1 - \frac{h\nu}{kT_\mathrm{s}}), \tag{1.1.14}$$

absorption coefficient is,

$$\kappa_\nu = \frac{c^2}{8\pi\nu^2}\frac{g_\mathrm{u}}{g_\mathrm{l}}A_\mathrm{ul}n_\mathrm{l}\frac{h\nu}{kT_\mathrm{s}}\phi(\nu). \tag{1.1.15}$$

Degeneracy factor g of spin is $g = 2F + 1$ where F is total spin angular momentum. For atomic Hydrogen, total spin angular momentum is sum of spin of proton s_p and electron s_e. When the spin is parallel $F = s_\mathrm{p} + s_\mathrm{e} = 1/2 + 1/2 = 1$, and when the the spin is anti-parallel $F = 1/2 - 1/2 = 0$. Then the degeneracy factors are $g_\mathrm{u} = 2F + 1 = 2 + 1 = 3$, and $g_\mathrm{l} = 2F + 1 = 1$. Putting these parameters in Equation (1.1.14) (Boltzmann distribution for small $h\nu/kT_\mathrm{s}$), $n_\mathrm{u} \sim 3n_\mathrm{l}$ is achieved. Then the total number density of atomic Hydrogen per unit volume is

$$n = n_\mathrm{u} + n_\mathrm{l} \sim 4n_\mathrm{l}. \tag{1.1.16}$$

Substitute this relation for Equation (1.1.15), then total number density is obtained

$$n\phi(\nu) = \frac{32\pi\nu kT_\mathrm{s}}{3c^2hA_\mathrm{ul}}\kappa_\nu. \tag{1.1.17}$$

Column density of atomic Hydrogen can be derived by integrating $n\phi(\nu)$ for line of sight direction of the H I cloud ($x = 0$–L, where L is the line of sight length of the cloud) and for frequency covering whole spectrum of the H I cloud ($\nu = \nu_1$–ν_2, where ν_1 and ν_2 should be chosen enough to cover the entire spectrum of the 21 cm line)

$$N(\mathrm{H\,I}) = \int_{\nu_1}^{\nu_2}\int_0^L n\phi(\nu)\,dxd\nu. \tag{1.1.18}$$

Substitute Equation (1.1.17) for this Equation,

$$N(\mathrm{H\,I}) = \frac{32\pi\nu kT_\mathrm{s}}{3c^2hA_\mathrm{ul}}\int_{\nu_1}^{\nu_2}\int_0^L \kappa_\nu\,dxd\nu. \tag{1.1.19}$$

Note that the assumption of isothermal condition (spin temperature T_s is uniform throughout the cloud), and ν is regarded as constant under $\nu_2 - \nu_1 \ll \nu$. Remember that spatial integration of absorption coefficient κ_ν corresponds to optical depth,

$$\tau_\nu = \int_0^L \kappa_\nu d\nu, \tag{1.1.20}$$

where τ_ν is line of sight optical depth of the H I cloud. For optically thin cloud ($\tau_\nu < 1$), observed brightness temperature is exact product of spin temperature and optical depth,

$$T_\mathrm{b} = T_\mathrm{s}(1 - e^{-\tau_\nu}) \tag{1.1.21}$$

$$\sim T_\mathrm{s}\tau_\nu, \tag{1.1.22}$$

then the T_s and τ_ν can be replaced by observed quantity. And finally convert the variable of frequency to radial velocity. In case the radial velocity of the cloud is effectively smaller than the light speed ($v \ll c$), the doppler relation of light can be written as $dv/c = d\nu/\nu$. So the displacement of frequency can be converted to that of radial velocity $d\nu = (\nu/c)dv$. Finally, the column density of the cloud can be expressed as follows:

$$N(\mathrm{H\,I}) = \frac{32\pi\nu^2 k}{3c^3 h A_{\mathrm{ul}}} \int_{v_1}^{v_2} T_{\mathrm{b}}\, dv. \tag{1.1.23}$$

Note that the values of the constants are $\nu \sim 1.420 \times 10^9$ [s^{-1}], $k \sim 1.381 \times 10^{-23}$ [m^2 kg s^{-2} K^{-1}], $c \sim 2.998 \times 10^8$ [m s^{-1}], $h \sim 6.626 \times 10^{-34}$ [m^2 kg s^{-1}], and $A_{\mathrm{ul}} \sim 2.869 \times 10^{15}$ [s^{-1}]. When the units of N(HI), T_{b}, and v are [cm^{-2}], [K], and [km s^{-1}], respectively, the column density is

$$N(\mathrm{H\,I}) = 1.823 \times 10^{18} \int_{v_1}^{v_2} T_{\mathrm{b}}\, dv. \tag{1.1.24}$$

This is the common equation of calculating the column density of the atomic Hydrogen cloud from the observed spectrum. But again note that this equation is derived with optically thin assumption, and another derivation is necessary to estimate actual column density for optically thick cloud.

Derivation of Physical Parameters of Atomic Hydrogen Gas : Optically Thick Component

The physical parameters of the H I gas have been rather difficult to be derived. This is due to the H I emission has a single observed quantity, intensity as a function of velocity, for two independent variables, spin temperature T_s and H I optical depth τ_{HI}. This does not allow us to determine each of these from a single observation.

H I medium consists of warm and cold components (for a review see Kalberla & Kerp 2009, Dickey & Lockman 1990). These components are usually called as a warm neutral medium (WNM) and a cold neutral medium (CNM). These construct a two-phase structure, characterized by a cloudy, dense structure of CNM, and a diffuse WNM. The mass of the warm H I gas, which has a spin temperature extremely higher than 100 K (several thousand kelvin), is measurable at reasonably high accuracy because the WNM is typically diffuse ($\lesssim 1$ cm^{-3}) so an optically thin approximation can be applied (T_s and τ_{HI} can be replaced by observed intensity T_{b}; see previous section). On the other hand, the cold components that has T_s of 20–80 K is typically not optically thin. So it is necessary to derive both variables of T_s and τ_{HI} to measure the mass of the CNM, which may not be easy. It is also difficult to extract only the component of the CNM since its emission is blended with the multiple WNM components, which are as bright as the CNM components and have large spectral widths.

One possible way to extract the cold H I gas components is to see the absorption spectra of H I toward bright background continuum sources. Heiles & Troland (2003a,b) has developed least-squares procedure of gaussian fitting to determine the opacity profile from the 21 cm line emission and absorption against 79 continuum sources. Their

Gaussians provide the CNM spin temperatures, upper limits on the kinetic temperatures for both CNM and WNM from the line widths and the column densities. For the opacity spectra, they assumed the minimum number of the Gaussians which is required to reproduce them to within the uncertainties as the best fit. The derived CNM spin temperature histogram peaks at about 40 K and its median weighted by the column density is 70 K. About 60% of all H I is the WNM. Dickey et al. (2003) has also studied the 21 cm absorption spectra and the corresponding emission spectra toward bright continuum sources in the test region ($326° < l < 333°$) of the Southern Galactic Plane Survey. They found that the median temperature is about 65 K, and the clouds with temperatures below 40 K are common, but not as common as the warmer clouds (40–100 K). For the extragalactic case, Marx-Zimmer et al. (2000) has studied the H I absorption in the Large Magellanic Cloud, by comparing the large beam single dish spectra with that of the long baseline interferometer data that only includes the small scale absorption feature. They found that the cool atomic phase of the interstellar medium is more abundant in the LMC ($f_c = 35\%$ for $T_c = 60$ K) relative to the WNM than in our Galaxy ($f_c = 24\%$ for $T_c = 60$ K). In the way using the absorption spectra of H I, unfortunately, the observed sample of the cold H I is limited only where the background continuum sources are available. Further efforts are still needed to better constrain the physical properties of the cold H I.

Fukui et al. (2014) and Fukui et al. (2015c) have constructed another way to estimate the true column density of the H I medium. They assumed that dust opacity should be highly correlated with the H I intensity if the H I is optically thin and the gas and the dust are well mixed with uniform properties. To examine this assumption, they analysed archival data sets of the optical depth at 353 GHz (τ_{353}) and the integrated intensity of H I ($W_{\rm HI}$). The Planck Legacy Archive (PLA) explanatory supplement (Planck Collaboration 2013) was used for τ_{353} data, and the GALFA-H I survey of the Arecibo telescope was used for H I data. Figure 1.1 is a scatter plot of τ_{353} and $W_{\rm HI}$ for the high latitude clouds MBM 53, 54, 55 and HLCG 92–35 (Figure 3 of Fukui et al. 2014). In Figure 1.1(a), τ_{353} should be highly correlated with $W_{\rm HI}$ if the H I is optically thin, but the correlation is poor and the scattering is fairly large with correlation coefficients of ~ 0.6. In Figure 1.1(b) and (c), $T_{\rm d}$ for every 0.5 K interval at each points in Figure 1.1(a) is indicated. The scatter plot shows clear trend with $T_{\rm d}$ and the slope k and the intercept (K km s^{-1}) for the plots of each temperatures becomes steeper and smaller as $T_{\rm d}$ increases. The H I gas associated with the highest $T_{\rm d}$ (> 21.5 K) is typically located at the diffuse part of the clouds, so it is optically thin with the highest possibility. So a relationship for the optically thin H I gas between H I column density and τ_{353} can be determined from the slope k of this temperature range;

$$N_{\rm HI}[{\rm cm}^{-2}] = 1.823 \times 10^{18} \cdot k \cdot \tau_{353}. \quad (1.1.25)$$

So the true column density map can be obtained from the τ_{353} map. The result shows that the H I is dominated by optically thick gas having a low spin temperature of 20–40 K and a density of 40–160 cm^{-3}. And the total mass of the H I envelope in this area is an order of magnitude larger than that of the CO clouds. The result of the whole

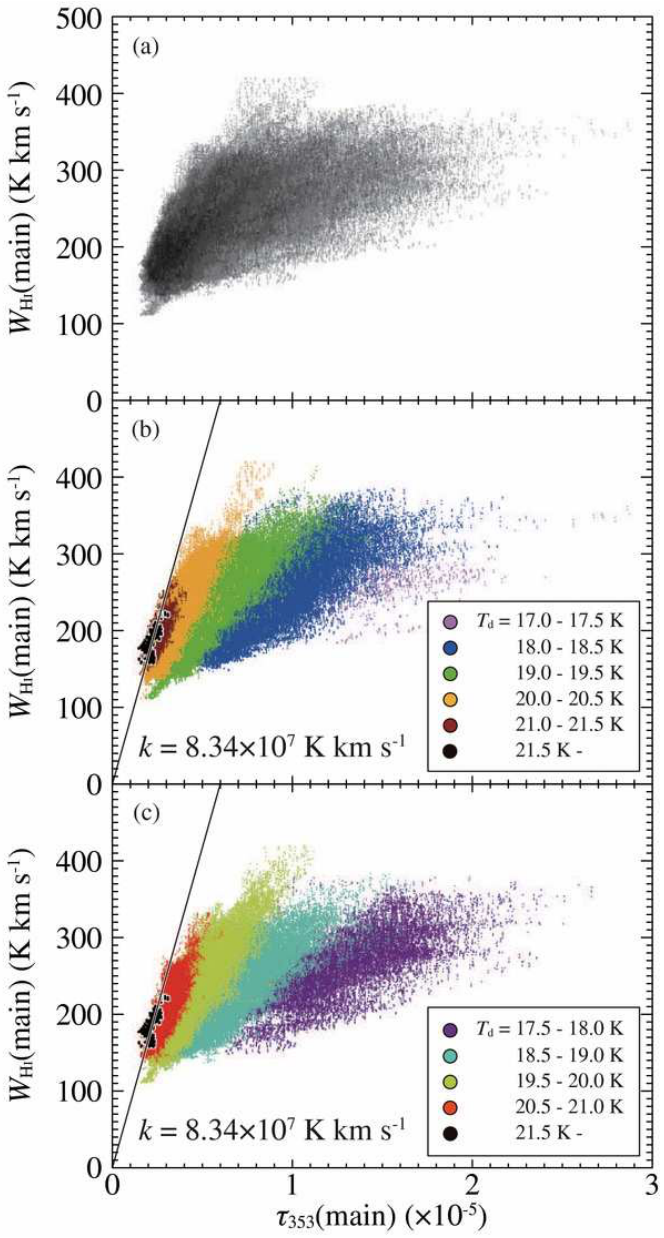

Figure 1.1: (a) A scatter plot of τ_{353} and $W_{\rm HI}$ for high latitude clouds MBM 53, 54, 55 and HLCG 92–35 (Figure 3 of Fukui et al. 2014). Specific areas where the relation of dust and H I seems to be different from the other area (like ionized medium) are masked (for detail see the paper). (b)(c) The same scatter plots for $T_{\rm d}$ in windows of 0.5 K intervals every 1 K.

galactic plane case (Fukui et al. 2015c) suggests that the average column density of H I is 2–2.5 times higher than that is derived on the optically thin assumption in the local ISM.

Formation of CNM

As mentioned in the previous section, H I gas consists of two-phase; a diffuse (< 1 cm^{-3}) WNM and a dense ($\sim$ 10–100 cm^{-3}) CNM. Since the intermediate phase is transient, it is important to understand how the phase-shift is triggered and how the CNM is formed. In the classical theory, the CNM is considered to be formed through gravitational instability derived by an efficient radiative cooling, when the medium is getting dense enough. A free fall time of spherical H I cloud is given by

$$t_{\rm ff} = \sqrt{\frac{3\pi}{32G\rho}}. \tag{1.1.26}$$

$t_{\rm ff}$ of an atomic medium of number density < 1 cm^{-3} is greater than 10^8 years. As explained in the following section, this is more than one order longer than the typical formation and evolution time scale of dense cloud (§1.1.4). The simple gravitational contraction of the WNM seems to be not a main scenario of the formation of the CNM.

In current theory, the CNM is also considered to be formed thorough a thermal instability induced by super sonic shock compressions. Many authors have studied and simulated the dynamical condensation processes of the CNM formation driven by thermal instability. Simple shock propagation model predicted the thermal instability is driven in the post -shock layer and the CNM is formed (Koyama & Inutsuka 2000, 2002, Inutsuka et al. 2005). Simulations of supersonic converging flows (or colliding flows in another expression) showed that thermal instability at the stagnation point can generate formation of dense clouds by piling up the WNM (e.g., Hennebelle & Pérault 1999, Audit & Hennebelle 2005, Hennebelle & Audit 2007, Heitsch et al. 2005, 2006, Inoue & Inutsuka 2012).

On the other hand, recent high-resolution magneto-hydrodynamical simulations of two-fluid dynamics with radiative cooling, radiative heating, and thermal conduction have shown that the magnetic pressure prevents the contraction of the clouds, so the formation of dense clouds of $> 10^3$ cm^{-3} is considered to require multiple episodes of supersonic compression (Inoue & Inutsuka 2008, 2009, Heitsch et al. 2009). Therefore, the formation process of the denser clouds than the CNM is not so simple. Further discussion of formation of such dense clouds will be done in the following session of molecular cloud formation (§1.1.4).

1.1.3 Giant Molecular Clouds

After a cool and dense cloud is formed from the diffuse WNM, formation rate of molecular Hydrogen in the cloud is getting to exceed the destruction rate, and so called "*molecular cloud*" is formed. Since the molecular cloud is the primary site of

the star formation, it is one of the most important object to be studied in order to understand how stars are formed in a galaxy. In this section the basic information of molecular clouds such as chemical composition, how to be observed, and derivation of the physical parameters are summarized. Their formation process, the statistical physical tendency, and the relation to the star formation is also discussed.

Molecular Cloud: Basic Information

When we look up the Milky Way in the night sky, we can see the dark area where stars seem to be less distributed. Such dark lane of the Milky Way is due to absorption of background starlight by dense interstellar medium, so called *dark clouds*. Where gas is cold ($T \sim 10$ K) and dense ($> 10^2$–10^3 cm^{-3}) like dark clouds, the interior gas is mainly in a form of a molecule. So such high density interstellar clouds are called as *molecular clouds*.

The main components of a molecular cloud are molecular Hydrogen (73% in mass), atomic helium (25%), dust particles (1 %, depending on metallicity), neutral atomic hydrogen (< 1 %), and a rich mixture of interstellar molecules (< 0.1 %). Mean molecular weight is thus 2.3 to 2.8 depending on whether the dust particles are included or not. However, molecular Hydrogen hardly emits any line emissions in the typical molecular clouds (below 10 K with density of 10^2–10^3 cm^{-3}). The first reason is molecular Hydrogen does not have a permanent dipole moment, so the transition probability (Einstein coefficient) of rotational/vibrational energy state is quite low and the emitted line is quite weak. Secondly, molecular Hydrogen is quite light molecule and has no low-lying rotational transitions. Lowest transition of rotational line corresponds to 510 K (para-state) and is located in the infra-red (28 μm), so it requires heated gas to be excited. Finally, the weakly emitted rotational transition line is strongly absorbed by the various molecules (includes H_2 itself) of the atmosphere of the earth. Therefore, line emissions of the other molecules such as carbon monoxide (CO) is often used to observe molecular clouds. The relative abundance of CO molecules is typically 1/10,000. CO is second abundant molecules in a molecular cloud next to molecular Hydrogen (and atomic Helium). CO has a permanent dipole moment, and the excitation energies of rotational transitions are low since it is a heavy molecule with low-lying rotational energy levels. CO can be rotationally excited in a cold environment lower than 10 K, and can emit rotational transition lines of mm to sub-mm wavelength. The lowest transition is often written as CO(J=1–0) (or ^{12}CO(J=1–0) to be distinguished from ^{13}CO), because this includes a transition of rotational quantum number J.

Giant Molecular Clouds

From the classical classification of molecular clouds in Goldsmith (1987), molecular clouds are classified as either giant molecular clouds or dark clouds according to their size and mass. Molecular clouds that have large mass enough to form massive stars (typically $> 10^4$ M$_\odot$) are called as giant molecular clouds (GMCs; for a review see

Fukui & Kawamura 2010). The observation of GMCs have performed from 1970s using ^{12}CO(J=1–0) line as a large survey toward the Galactic Plane (Dame et al. 1987, Solomon et al. 1987, Combes 1991, and references therein). The most near and common example of a GMC is Orion A and Orion B molecular clouds (for ^{12}CO(J=1–0) line observation, (Kutner et al. 1977, Maddalena et al. 1986, Wilson et al. 2005, Nishimura et al. 2015), which is the nearest active forming region of high and low mass stars (Genzel & Stutzki 1989, Chini et al. 1997, Megeath et al. 2012). The total mass of the Orion molecular clouds is $\sim 10^5$ M$_\odot$. On the other hand, less massive clouds ($< 10^4$ M$_\odot$) like Taurus dark cloud is a site of low mass stars of solar mass or less (Mizuno et al. 1995). The typical size of the GMCs is 50 pc to several hundred pc and the typical mass is 10^4–10^7 M$_\odot$ (Blitz 1993, Fukui et al. 1999, 2008). The GMCs is the principle site of stellar cluster and association formation (Blitz 1993), which includes intermediate to high mass stars of several to tens of solar mass (OB type stars). Since most stars form in clusters and associations (Roberts 1957), it is considered that the majority of stars in a galaxy are formed in the GMCs. It is therefore important to understand how the GMCs are formed and evolved in order to understand evolution of galaxies from the Local Group to the most distant Universe.

Physical Properties of the GMCs

It is of great interest to investigate the physical properties of GMCs, which are important in understanding the formation and the evolution of GMCs. The physical properties of GMCs have been discussed in a lot of works on the various types of galaxies (e.g., Blitz et al. 2007, Fukui & Kawamura 2010). Typical physical properties of the GMCs and their interpretations are summarized in a review of McKee & Ostriker (2007).

A distribution function of the mass of the GMC is called as a mass function, or a mass spectrum. The mass spectrum of the GMCs is offen given with a power law of the mass M,

$$f(M) = \frac{dN}{dM} \propto M^{-\gamma}. \tag{1.1.27}$$

The power γ is roughly between $1.4 < \gamma < 2.0$ in a mass range of $M \gtrsim 10^2$ M$_\odot$ from the observation of typical star forming regions in our Galaxy (e.g., Cygnus: $\gamma \sim 1.6$ (Dobashi et al. 1996), Cepheus and Cassiopeia: $\gamma \sim 1.7 \pm 0.3$ (Yonekura et al. 1997), Gemini and Auriga: $\gamma \lesssim 1.0$ Kawamura et al. 1998). Mass spectra of the cores, that are sub-structure of the GMCs, can be defined similarly, and they are good clues to understand the initial mass function (IMF) of the stars.

One of the most important information from the observation of GMCs using molecular lines is an extremely broad line width. Since the line width of the GMCs typically cannot be explained by thermal motions of the molecules within a order of ~ 10 K, GMCs are considered to be in a super sonic turbulence. A classical empirical relation between the size and velocity dispersion of GMCs are,

$$\sigma_v \propto R^\beta, \tag{1.1.28}$$

where σ_v is the velocity dispersion and R is the size (radius) of the cloud. This is often called as the size-linewidth relationship (the First scaling relationship of Larson (1981)). The most commonly accepted values of the exponents is $\beta \sim 0,5$ (e.g, Solomon et al. 1987), and $\sigma_v \propto R^{0.5}$ is one of the most famous relations so called Size-Linewidth relation. Note that σ_v is offen substituted by FWHM velocity width δv, where $\sigma_v = \delta v/\sqrt{8\ln(2)}$. This scaling relationship suggests that the structure of GMCs are highly hierarchical. In addition, Heyer et al. (2009) have found that the velocity dispersion does not depend simply on the size of the clouds, but on the square root of the column density as well. The revised relation is

$$\delta v \propto \Sigma R^{1/2}, \tag{1.1.29}$$

where Σ is mean column density of the cloud. Note that it is assumed that the clouds are in a gravitational equilibrium.

Larson's second relationship is gravitational equilibrium of the cloud. The mass of the sphere in gravitational equilibrium can be given by the virial theorem,

$$M_{\rm vir} = \frac{5\sigma_v^2 R}{G}, \tag{1.1.30}$$

where G is gravitational constant. This is called as virial mass. If the column density of GMCs are uniform, i.e., M/R^2 is constant, Equation (1.1.30) gives the size-linewidth relationship $\sigma_v \propto R^{0.5}$. If the GMC is in the gravitational equilibrium, the observed mass should be equal to their virial mass. The mass of the cloud can be derived from the observed intensity using a radiative transfer calculation if the observed line is optically thin. On the other hand, ^{12}CO(J=1–0), which is one of the strongest line emission and can trace the most diffuse edge of the cloud, is usually optically thick for typical column density of the GMCs. CO-to-H_2 conversion factor, $X_{\rm CO}$ [cm^{-2} (K km s^{-1})$^{-1}$], is often introduced to derive H_2 from ^{12}CO(J=1–0) luminosity $L_{\rm CO}$. Since there is a clear positive linear correlation between $L_{\rm CO}$ and virial mass of the cloud, by assuming the all GMCs are in the virial equilibrium, $X_{\rm CO}$ can be determined from the coefficient of the best fit line of the plot. When the unit of $L_{\rm CO}$ is given as [K km s^{-1} pc^2], which is useful expression for the observation of the GMCs in the Milky Way and the nearby galaxies, the luminosity mass of the GMC M_{H_2} is given by,

$$M_{H_2}\,[{\rm M}_\odot] = 4.4\,\frac{X_{\rm CO}}{2\times10^{20}\,[{\rm cm}^{-2}\,({\rm K\,km\,s}^{-1})^{-1}]}\,L_{\rm CO}\,[{\rm K\,km\,s}^{-1}\,{\rm pc}^2], \tag{1.1.31}$$

where a factor of 1.36 is included to account for the mass contribution of helium. If the relatively optically thin line, such as ^{13}CO and C^{18}O is used for the GMC observation, the actual luminosity mass can be derived by calculating a radiative transfer equation. This makes it possible to compare the luminosity based mass to the virial mass and to check whether the GMCs are in the gravitational equilibrium or not. Surveys of molecular clouds in ^{13}CO in the Milky Way suggested that the degree of the gravitational relaxation depends on $M(H_2)$ and that the ^{13}CO clouds of $M(H_2)$ greater

than 10^4 $M_\odot$ are consistent with the virial mass (Yonekura et al. 1997, Kawamura et al. 1998). The GMCs with $M(H_2)$ greater than $\sim 10^5$ $M_\odot$ are likely gravitationally relaxed (Kawamura et al. 1998, Heyer et al. 2009).

The comparisons of these physical parameters throughout the galaxy between the Local Group including the Milky Way have been performed in a lot of works (e.g., Blitz et al. 2007, Hughes et al. 2013, and for a review see Fukui & Kawamura 2010). Although some dependences of the GMC mass on the metallicity of the galaxy can be seen, the X_{CO} factor, the size-linewidth relation, the GMC mass spectra are roughly similar among these galaxies, suggesting that the GMCs share similar properties and the physics of formation process in the Local Group.

1.1.4 Formation and Evolution of GMCs

Evolution of GMCs

As mentioned in the previous section, the GMCs is the principle site of the stellar cluster formation and their formation and evolution process are important clue to understand the evolution of galaxies. The evolution of GMCs have been discussed in many works, mainly by the survey observation of GMCs in nearby galaxies (e.g., Blitz et al. 2007, Kawamura et al. 2009). A strong point of the survey of external galaxies is that the uncertainties due to distance error and fore-/back-ground emission are low.

Blitz et al. (2007) and Kawamura et al. (2009) have suggested a GMC evolution process using the 272 samples of the GMCs in the Large Magellanic Cloud (LMC). They classified the GMCs in three types according to their star formation activity: "massive-starless" molecular clouds in the sense that they are not associated with H II regions or young clusters (Type I); molecular clouds with H II regions (Type II); and molecular clouds with H II regions and young clusters (Type III). The example of these three types are shown in Figure 1.2. They argued that these types indicate an evolutionary sequence; i.e., the youngest phase is Type I, followed by Type II, and the last phase is Type III, where the most active star formation takes place leading to cloud dispersal. A comparison among the three Types indicates that the GMC size and mass tend to increase from Type I/II to Type III, indicating that the GMC is evolved by accretion from the surrounding H I envelope (Fukui et al. 2009). They considered that the number of the three types of GMCs should be proportional to their timescale. By adopting the timescale of the youngest stellar clusters of 10 Myr, and by estimating the timescale of cluster associated cloud (Type III) is $\sim$ 7 Myr from the associated fraction of the young clusters in the entire LMC, they roughly estimated the timescales of Types I, II, and III to be 6 Myr, 13 Myr, and 7 Myr, respectively. This corresponds to a lifetime of of the GMCs with mass $> 5 \times 10^4$ $M_\odot$ (mass limit of their samples) is 20–30 Myr. This is currently the most reliable estimate of the lifetime of the GMCs. Similar lifetime is also obtained from the similar population analysis of M33 (Miura et al. 2012). Fukui et al. (2009) analyzed H I envelopes associated with GMCs in the LMC, which supplements the GMC evolution scenario above. Using average

line width of the H I envelope of 14 km s^{-1} and the mean density in the envelope of 10 cm^{-3}, they argued that the H I envelopes are gravitationally bound by GMCs, and a continual increase in the mass of GMCs via H I accretion at an accretion rate of 0.05 $M_\odot$ yr^{-1} over a timescale of 10 Myr.

Formation of GMCs

How and where GMCs are formed in a galaxy is possibly more important than the evolution of GMCs, because once the GMCs are formed, their physical properties are roughly similar within scaling relationships. However, the formation of a GMC is a quite difficult physical process to be probe from the observation, mainly due to the complex nature of the atomic medium (inseparable mixture of WNM and CNM). Thus, theoretical works of GMC formation are always prior to the observation from the past. In principle, a GMC is considered to be formed by coagulations of cold H I clouds, by which the cloud gradually increases the mean size and mass until that of a (self-gravitating) GMC is reached (e.g., Field & Saslaw 1965). The main difficulty with this scenario is that it is too slow to form a GMC (it requires $\gtrsim 2 \times 10^8$ years for the peak of the mass distribution to exceed 10^5 $M_\odot$, Kwan 1979). In the 1980s, the focus shifted to large-scale instabilities in the diffuse ISM (e.g., Elmegreen 1979, 1995). Classically, this includes a Parker instability of a disk (Parker 1966, Shu 1974), and self-gravitating instabilities. However, numerical simulations have shown that the Parker instability is not able to create structures resembling GMCs (e.g., Kim et al. 2002). Spiral arms are also the most favorable regions for self-gravitating instabilities (Elmegreen 1994), because the characteristic (thin-disk) growth rate $\propto G\Sigma_{\rm gal}/c_S$ is highest there. Observations of external spiral galaxies show that most of the molecular gas is concentrated in the spiral arms (e.g., Helfer et al. 2003, Schinnerer et al. 2013), and within the Milky Way the most massive clouds are strongly associated with spiral arms (e.g., Stark & Lee 2006, Sawada et al. 2012). The observed relationship between GMCs and spiral structure suggests that the GMCs are preferentially born in the high density gas that makes up the arms; this is consistent with theoretical expectations because growth rates for all proposed mechanisms increase with the gas surface density.

As introduced in the former section of CNM formation, recent numerical simulations focus on the GMC formation induced by super sonic shock compression. Two types of shocks are often considered in the simulations; simple shock propagation (e.g., Koyama & Inutsuka 2000, 2002, Inutsuka et al. 2005), and supersonic converging flows (or colliding flows) (e.g., Hennebelle & Pérault 1999, Audit & Hennebelle 2005, Hennebelle & Audit 2007, Heitsch et al. 2005, 2006, Inoue & Inutsuka 2012). The colliding flow is currently the most accepted model of the GMC formation, but note that two types of shocks are essentially the same, they both mean that the shock compression of the medium induce dense gas behind the shock. Locally, on scales up to $\sim$ 100 pc, it is considered that the stellar feedback processes (expansion of H II region and super nova blast wave, see §1.2) are main driver of interstellar shocks and/or converging streams of gas (Dobbs et al. 2014), and formation of up to a few times 10^4 $M_\odot$ mass clouds

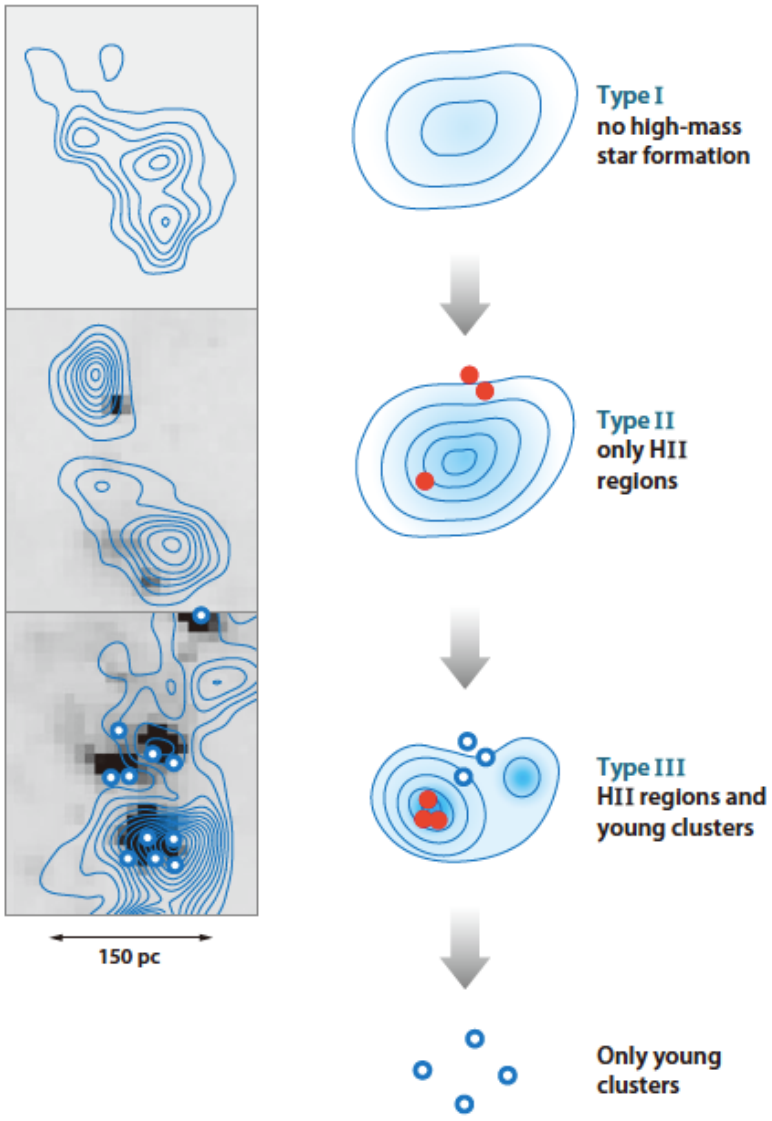

Figure 1.2: Figure 7 of Fukui & Kawamura (2010) that shows the evolutionary sequence of the GMCs. (for the original discussion see Blitz et al. 2007, Kawamura et al. 2009). The left panels are the examples of the LMC GMCs. They are Type I (GMC 225, LMC N J0547-7014 in Fukui et al. (2008)), Type II (GMC 135, LMC N J0525-6609), and Type III (the northern part of GMC 197, LMC N J0540-7008) GMCs from the top panel, respectively. Each panels presents Hα images with the NANTEN ^{12}CO(J=1–0) contours. Open blue circles indicate the position of young clusters. The right panels are cartoon illustrations for each evolutionary stages. Open blue circles and filled red circles represent young clusters and H II regions, respectively.

can be explained by this localized flows. More massive clouds ($\gtrsim 10^4$ $M_\odot$), which is the most part of the GMCs, can be produced by large-scale conversing flows. There are three possible drivers of large-scale shocks; global instability of a disk (e.g., Wada et al. 2000, Kim et al. 2002, Tasker & Tan 2009), spiral arms (e.g., Kim & Ostriker 2006, Dobbs & Pringle 2013), and large expanding shells and bubbles (e.g., McCray & Kafatos 1987, Hartmann et al. 2001, Ntormousi et al. 2011). A basic concept of first two drivers is that accumulation of gas to the large-scale structure of spiral arms enhances the frequency of the gas collision. The third one is only one which can drive the interstellar shocks even in a interarm region of a spiral galaxy, and in a low mass galaxies in which large scale spiral arms are not at work.

A converging flow is not by itself sufficient to form a GMC, must combine with thermal instability to produce fast cooling. As mentioned before, recent high-resolution magneto-hydrodynamical simulations have shown that the magnetic pressure prevents the contraction of the clouds (Inoue & Inutsuka 2008, 2009, Heitsch et al. 2009). The formation of dense clouds of $> 10^3$ cm^{-3} seems to require multiple episodes of supersonic compression. Taking these facts into account, Inutsuka et al. (2015) have constructed an expanding-bubble dominated picture of the formation of molecular clouds. They argued that the all molecular clouds formation can be explained by the feedback effects (H region and supernova), by estimating the shock compression frequency of 1 Myr (at least several times shocks per GMC formation timescale of 10 Myr) and the velocity coincidence of shock propagating speed ($\sim$ 10 km s^{-1}) and the velocity dispersion of the clouds ($\lesssim$ 10 km s^{-1}). Repeated episodes of shock compression allow clouds to be built up incrementally from pre-existing denser gas.

1.1.5 Massive Star and Stellar Cluster Formation in GMCs

General Problems of Massive Star Formation

A canonical model of formation process of low mass stars whose mass is comparable to or less than the sun contains two problems when it is applied to the formation of massive stars. The first one is a timescale problem. Typical accretion rate of a low mass star is $\sim 10^{-5}$ $M_\odot$ yr^{-1}. However, a typical lifetime of massive stars is known to be a few Myr, then the mass of the formed star is no greater than ~ 30 $M_\odot$ even if the mass accretion continues to the end of the lifetime. The second problem is feedback effects. In the model, the central star becomes a main sequence star if it's mass is getting to ~ 8 $M_\odot$. Thereafter, the mass accretion is largely limited by the strong radiation from the star. Conditions for the formation of massive stars considering this feedback effects are given in Wolfire & Cassinelli (1987). The upper limit of the formed star is $\sim$ 10–20 $M_\odot$ in spherical accretion with typical accretion rate of $\sim 10^{-5}$ $M_\odot$ yr^{-1}. In other words, rapid accretion $\gtrsim 10^{-4}$ $M_\odot$ yr^{-1} is required to form massive stars.

In the case of massive stellar cluster, the situation is more serious. Especially, super star clusters (SSCs) are the most massive clusters in the Galaxy, with stellar densities exceeding 10^4 stars pc^{-3} in their cores within a 10 pc, with mass range of 10^4 to 10^7

$M_\odot$ (e.g., Miocchi et al. 2013). One famous example of the SSCs is Westerlund 2, which is an unusually rich and compact young cluster located close to the tangent of the Carina arm. It is one of the youngest known clusters in the Galaxy (2–3 $\times 10^6$, Piatti et al. 1998) with total stellar mass of $\sim$ 1–3 $\times 10^4$ $M_\odot$ in the form of stars of 1 to 120 $M_\odot$ (e.g., Ascenso et al. 2007). In the Large Magellanic Cloud, R136 is known to one of the most prominent SSCs in the Local Groups. R136 has $\sim 10^6$ stars within a few parsecs, and contains unusual amount of O3 type stars of $\gtrsim$ 120 $M_\odot$ (Hunter et al. 1995, Massey & Hunter 1998). In such SSCs, extremely high mass accretion rate of $\gtrsim 10^{-2}$ $M_\odot$ yr^{-1} is required.

Possible Massive Star Formation Scenario: Accretion of Dense Cores

Initially, two main theories for the massive star formation is proposed; core accretion (or turbulent core model; e.g., McLaughlin & Pudritz 1996, McKee & Tan 2003) and competitive accretion (e.g., Bonnell et al. 2001, Wang et al. 2010). The turbulent core accretion model suggests that massive near-virial-equilibrium starless cores will collapse to form individual stars with non-thermal (turbulence and/or magnetic fields) Jeans mass. Competitive accretion also involves fragmentation of massive gas clumps, but initial masses of protostellar seeds are only of the order of the thermal Jeans mass and eventually become high–mass stars later accretion of previously unbound gas. In both case, observational evidences are reported in recent high resolution observations of infrared dark clouds (e.g., Peretto et al. 2013, Tan et al. 2013).

Possible Massive Star Formation Scenario: Cloud–Cloud Collision

Two scenario described above is concentrated on the local dynamics of the dense cores of typically smaller than 1 pc. Another aspect of the cluster formation is collapse of dense clumps in GMCs within a size scale of a few to ten parsecs. The cluster formation in GMCs is considered to be dynamically triggered by external events, as outlined in Elmegreen (1998). Among the possible external events, collisions of two clouds (cloud–cloud collision) is currently believed to be the most plausible formation scenario of massive stars and clusters, and especially SSCs in GMCs.

Basic concepts of the massive star and cluster formation via cloud-cloud collision is similar to the GMC formation induced by colliding flows, but the initial density is quite high, more than 10^3 cm^{-3}. Recent observation of GMCs around the Galactic SSCs Westerlund 2, NGC 3603, and RCW 38 have argued that these SSCs are formed via cloud–cloud collision (Furukawa et al. 2009, Ohama et al. 2010, Fukui et al. 2014, 2015b). These authors identified a pair of two GMCs with $\sim 10^5$ $M_\odot$ associated with each SSC, where the two clouds have a large velocity separation of 10–30 km s^{-1}. These velocity separations cannot be explained by expanding motion of the gas driven by stellar winds or supernovae. They argued that the strong shock compression of the molecular gas by a collision led to the formation of the massive clusters in a short time less than 1 Myr. Not only the SSCs, but also the formation of a single O star

and proto clusters by cloud-cloud collision is also reported for M20 (Torii et al. 2011), RCW120 (Torii et al. 2015), Serpens South infrared dark cloud (Nakamura et al. 2014), and Galactic center (50 km s^{-1} molecular cloud, Tsuboi et al. 2015). In the Large Magellanic Cloud, the ALMA observations revealed the formation of a 40 $M_{\odot}$ star in N159W south triggered by collision between two filamentary clouds at a relative velocity of $\sim$ 10 km s^{-1}, for the first time in the external galaxy.

For theoretical aspects, Inoue & Fukui (2013) discuss the mechanism of massive star formation via cloud-cloud collision by using three-dimensional, isothermal, magnetohydrodynamics simulations with the effect of self-gravity. They demonstrate that massive, gravitationally unstable, molecular cloud cores are formed behind the strong shock waves induced by the collision. The massive molecular cloud cores formed by the cloudcloud collision are filamentary and magnetic fields perpendicular to the filaments play an important role on threading them. They also find that the massive molecular cloud cores have large effective Jeans mass owing to the enhancement of the strength of magnetic field by shock compression and turbulence in the compressed layer. So the colliding molecular gas can indeed create the dense and massive cloud cores, precursors of the high-mass stars, in the shock-compressed interface.

1.2 Feedback from Massive Stars and Their Effects on the Star Formation

Stars formed in molecular clouds, especially massive stars whose mass is more than a few times greater than the solar mass, give large feedback on surrounding interstellar medium by strong radiation, mass ejection, and Supernova explosion at the end of their life. Such stellar feedback strongly affects the interstellar medium as expanding shock, offen disperses the parental molecular clouds, and triggers next generation star formation by shock compression of interstellar gas. In this section, feedback events from massive stars and their effects on star formation is summarized.

1.2.1 Feedback from a Single Massive Star

H II region

Massive stars emit far ultraviolet (FUV) photons and strongly affect the surrounding interstellar medium (ISM). FUV photons with energy of $h\nu > 13.6$ eV can ionize ambient neutral Hydrogen gas. Stars with spectral types earlier than B0 have an ability of producing such FUV photons necessary to appreciably ionize the surrounding ISM. Spherically inonized area created by massive stars is commonly called as "H II region".

FUV photons with energy smaller than 13.6 eV reaches to the outer layer with teh neutral atomic and molecular medium. They photo-dissociate the molecules and ionize atomics whose ionization energy is smaller than atomic hydrogen, like atomic carbon. Such a boundary layer between the H II region and the molecular cloud is called as "Photo-Dissociation Region" (PDR). OB type stars, which are the main supplier of FUV photons, are generally formed in the dense molecular clouds, so the PDR is commonly seen around the H II regions or the active star forming regions.

H II regions can be observed soon after the massive stars are formed and they emit FUV photons. Since the massive stars are in general formed in a dense part of the ISM, H II regions are typically very dense and compact at the beginning. Such young H II regions are called as compact H II regions or ultra-compact H II regions, and are often regarded as indicators of a very young massive star formation. After the birth of the massive star, the H II region expands as it evolves. At the beginning, ionization front of the H II region is rapidly getting forward until the equilibrium between the ionization and the recombination of atomic Hydrogen is achieved. This spherically ionized area is called as Strömgren sphere, and the relationship between the density of the interstellar gas, the temperature of the star, and the radius of the region which it ionizes is often denoted as Strömgren radius, which can be roughly estimated by the following way. In the Strömgren sphere, the number density of the ionized atomic Hydrogen is not so differ from the initial state of the neutral Hydrogen, so the total number density of the ionized medium (including electrons) is almost doubled compared with the external neutral medium. In addition, the temperature of the gas inside the H II region is getting higher (more than 10,000 K) due to the absorption of FUV photons

and the redistribution of the excess energy above the ionisation limit. So the internal pressure of the H II region is much higher than the external medium, and the H II region experiences the second phase expansion by the pressure. It expands with a shock front just outside the ionization front, until the pressure equilibrium between the ionized gas and the ambient neutral medium is achieved. The size of the H II region at the final phase is roughly one hundred times of the Strömgren radius.

If one O7 type star is formed in the homogeneous molecular hydrogen medium whose density is 5×10^4 cm^{-3}, the first expansion timescale to the Strömgren sphere is several tens of year, and the terminal radius of this phase is about 0.03 pc. The second phase expansion to the pressure equilibrium is much longer and it takes several million years to expand to the terminal radius of ~ 2 pc. From here, the timescale of ultra-compact H II region, i.e., the timescale of H II region smaller than 0.1 pc in radius can be estimated about several $\times 10^4$ years. But actually, about 10 % of O type stars in our galaxy are in the phase of ultra-compact H II region. So if the O star formation is steady, the timescale of the ultra-compact H II region seems to be several $\times 10^5$ years. This is regarded as one curious paradox of the lifetime of the ultra-compact H II region.

A schematic view of a spherical H II region expanding into a homogeneous medium (Deharveng et al. 2010) is shown in Figure 1.3(top). As young H II regions begin their expansion, they interacts with the surrounding interstellar medium and the molecular clouds. The strong radiation field form the massive star disperses the parental cloud, which is considered to be one important driver of the death of the molecular clouds (negative feedback). On the other hand, since the expansion of a H II region is associated with the supersonic shock front, the interacted interstellar medium and molecular clouds are compressed and accumulated into a dense shell around the H II region. This induces the formation of the next generation molecular clouds and stars (positive feedback), which is often called as triggered star formation (Elmegreen & Lada 1977). This will be summarized in the following section (see §1.2.1)

Stellar winds

A star loses its mass by ejecting its outer layer, so called stellar winds. A massive star ($\gtrsim$ 30–40 M$_\odot$) will lose a substantial fraction of its mass in strong stellar winds with terminal velocity of $\sim$ 2,500 km s^{-1}, giving a net mechanical energy of $\sim 10^{51}$ ergs (Abbott 1982). This net energy is corresponds to the thermal energy of the H II region around them, and the energy input by the supernova explosion. So the effects of the stellar winds on the ISM are also significant, and they are also considered to be the driver of the triggered star formation.

Supernovae

It is known that the massive star heavier than ~ 8 M$_\odot$ explodes violently at the end of its life, which is called as supernova explosion (Core-collapse Type supernova). In this explosion much of the envelope of the original star, amounting to many M$_\odot$, is ejected at

the speeds of up to 10^4 km s^{-1}. The ejected envelopes are expanding in the interstellar medium and cause a strong shock wave in front of them. A nebula that consists of the ejected envelope and the swept-up interstellar matter is called as a supernova remnant (SNR). A SNR is filled with the warm ionized gas heated by a strong shock wave, that is often observed by the embedded thermal X-ray and/or non-thermal radio continuum. The SNRs are sometimes associated with a shell of interstellar medium that is swept-up and compressed by the shock wave of it's expansion. The SNRs are also considered to be a driver of triggered star formation, however, since the typical lifetime of the SNR is $\sim 10^5$ yr, it is too short to directly trigger the formation of the new stars around them (Desai et al. 2010). The terminal radius of the shock of the SNR is considered to reach to ~ 100 pc, as it expands even after the internal hot gas of the SNR disappeared. The shock compression itself might affect the ISM significantly, and play an important role of the formation of the molecular clouds (Inutsuka et al. 2015).

Triggered Star Formation

As seen in above, feedbacks from the massive stars trigger the next generation star formation. There are roughly two types of triggered star formation by a feedbacks of massive stars (Elmegreen 1998). The first one is globule squeezing, in which pre-existing dense clumps are compressed, either by the high ambient pressures in the H II regions or by the shock waves propagating from the supernovae. The second one is collect and collapse, in which the gas accumulated into a shell or ridge by the expanding H II regions, stellar winds or supernovae collapses to form new dense clumps and stars.

Globule squeezing is also known as radiative driven implosion (RDI). There are a lot of numerical simulations of this mechanism (e.g., Bisbas et al. 2011, Haworth & Harries 2012). The compression of the strong radiation field creates a pillar-like dense cloud, and next generation stars are formed in the pillar. Good examples in our galaxy are the fingers of Eagle nebula (White et al. 1999), and W5 region (Deharveng et al. 2012). Collect and collapse process is represented by a dense shell surrounding a H II region, which is shown schematically in Figure 1.3(top). The examples are RCW 32 (Yamaguchi et al. 1999), Sh2-219 (Deharveng et al. 2005), and W40 (Pirogov et al. 2013). Here the collection process requires pre-existing dense materials, like molecular clouds, since swept-up area and mass is quite small for a single H II region. From a model calculation of the GMC formation via collect and collapse of the ambient diffuse medium, it requires much larger size scale with longer timescale (radius $\sim$ 100–300 pc, McCray & Kafatos 1987). Such an large-scale feedback event will be mentioned in the next section.

Note that, as summarized in Dale et al. (2015), it is quite difficult to distinguish that the observed next generation stars are formed actually by the triggered star formation, or formed just spontaneously without any external events. Although a lot of observational works and numerical simulations discussed the triggered star formation, it is still controversial how and what degree does it affect on the star formation.

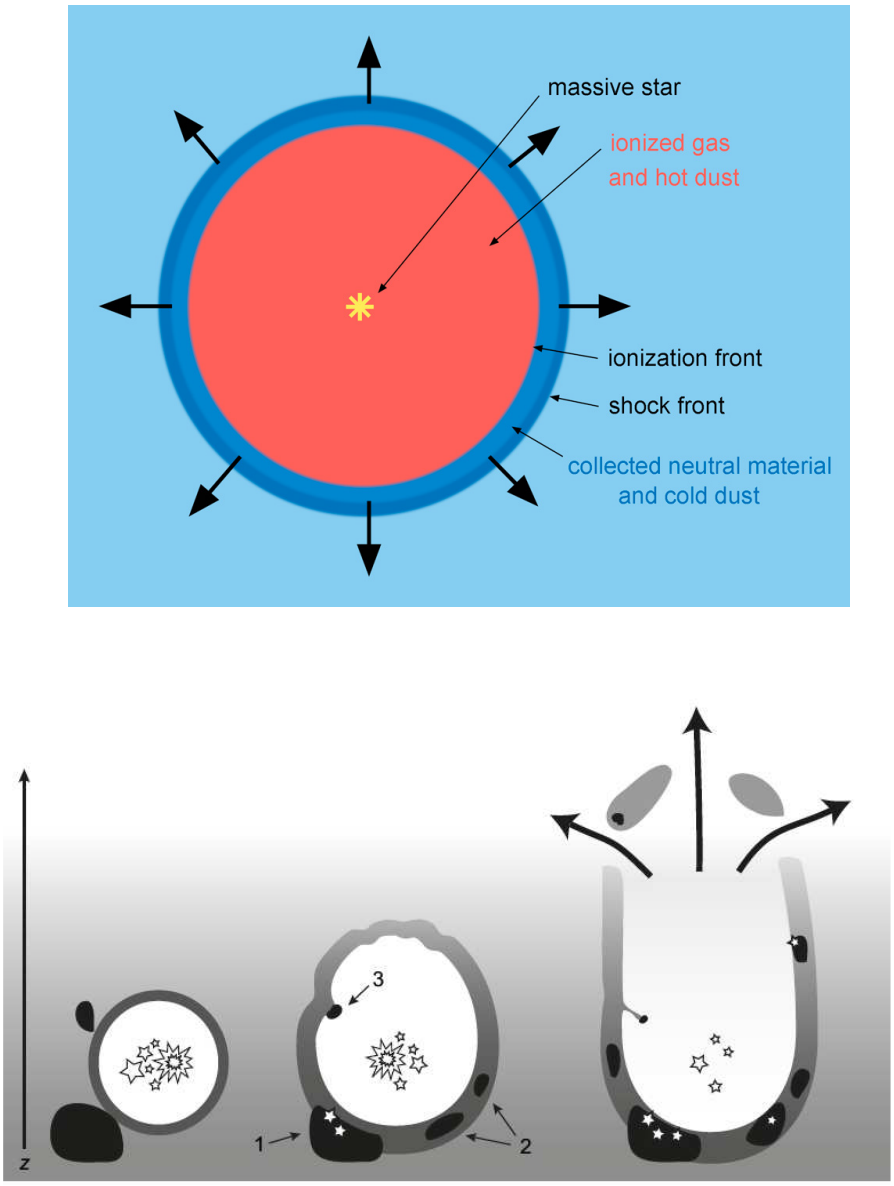

Figure 1.3: (top) A schematic view of a spherical H II region expanding into a homogeneous medium (Figure 1 of Deharveng et al. 2010). The ionized region is surrounded by a shell of dense neutral material collected during the expansion phase. (bottom) A schematic view showing an edge-on view of the evolution of a supershell in the Galactic Plane (Figure 1 of Dawson 2013). Time sequence is from left to right, illustrating the ways in which the large-scale stellar feedbacks can affect the interstellar medium. Here black blocks represent molecular clouds and the greyscale is the ambient atomic ISM. Labels 1 is an example of the triggering star formation in the existing molecular gas, label 2 is the formation of new molecular clouds, and label 3 is the disruption and entraining of the existing molecular clouds.

1.2.2 Superbubble and Supershell

Observations of the ISM in a galaxy have revealed the existence of large-scale spherically ionized area which is too large to be formed by a single massive star or supernova (e.g., McClure-Griffiths et al. 2002, Taylor et al. 2003). And also, there are numerous shell or hole features in the ISM of a galaxy, whose size is reached to hundreds of parsecs or even kilo-parsec scale. Such features are often called as "*superbubble*" or "*supershell*", and are considered to be formed by feedback of tens of, or even hundreds of massive stars. They also affect the interstellar medium in the similar way to the H II regions and SNRs, i.e., they compress and accumulate the surrounding medium while they are expanding, and trigger the formation of next generation stars. Conventionally, the one that is actively expanding with pressure of internal hot gas is called as superbubble, and the ones that is also expanding but internal hot gas is already dispersed away is called as supershell.

The classical analytical model for a stellar wind bubble expanding into a uniform medium was derived by Weaver et al. (1977), and modified for a system formed by multiple stellar winds and supernovae by McCray & Kafatos (1987). Their expansion mechanisms are similar to the H II regions and the SNRs, their size scale is much greater (typically $\gtrsim$ 100 pc). It is required more than 10 Myr to create them with energy requirements of $\gtrsim 10^{52}$–10^{53} ergs (e.g., McClure-Griffiths et al. 2000), corresponding to tens to hundreds of supernova explosion. Their expansion velocity is on the order of 10 km s^{-1} (e.g., Kim et al. 1999). A schematic view of the evolution of a supershell is shown in Figure 1.3(bottom) (see also Dawson (2013)). In the figure, time sequence is from left to right, illustrating how the large-scale stellar feedback affects the interstellar medium. The supershell is expanding with accumulating a surrounding diffuse interstellar medium into a dense shell. As the shell expands, it will encounter a pre-existing molecular clouds. The shell compress the clouds and trigger the star formation in them (Label 1 in the Figure). After the shock of the shell pass through the cloud, pillar-like feature remains (Label 3). And also, an initially atomic shell accumulate sufficient material to high column density enough to collapse into molecular clouds (Label 2). Since the expansion speed of the shell is faster toward diffuse directions, a shell with sufficient energy expands rapidly along the disk vertical density gradient, eventually breaking out and venting their hot interior gas into the Halo. If a shell is so large that it completely breaks out the disk, it will be observed as a hole of atomic gas. Such large shells whose diameter reaches to kilo-parsec are called as Supergiant shells (SGSs: Meaburn 1980) and are often observed in the disk of external galaxies (e.g., LMC: Kim et al. 1999, IC 2574: Walter & Brinks 1999, Weisz et al. 2009). This will be mentioned later section (§1.3.1).

Figure 1.4 shows the examples of superbubble and supershell. LHα 120-N 44 (N44; Henize (1956)) in the Large Magellanic Cloud (NGC 1929) is one of the most beautiful examples of superbubble (Figure 1.4(a)) whose diameter is $\sim$ 70 pc. Massive stars in the central cluster produce intense radiation, or intense shocks of supernovae, and expel the interstellar matter at high speeds. Hot gas heated by the internal clusters

is seen in X-rays by Chandra (blue). Accumulated interstellar dust and cold gas by the superbubble (red) and relatively cool optical ionized gas (yellow) is surrounding the hot gas. 1.4(b) is a Galactic supershell GSH 277+00+36 (McClure-Griffiths et al. 2003). This supershell is more than 600 pc in diameter, and extends at least 1 kpc above and below the Galactic mid-plane. It grows larger than the disk of the Galaxy and forms a chimney. A swept-up mass is $\sim 3 \times 10^6$ $M_\odot$ with expanding velocity of ~ 20 km s^{-1}, indicating that the supershell is created by several hundreds of massive stars between 1–2 $\times 10^7$ yr. However, in contrast to the N44 in the LMC, there is no remaining cluster of O and B stars was possible.

The triggered formation of molecular clouds and stars around superbubbles and supershells are also reported. For the N44 in the LMC, Chen et al. (2009) found that the alignment of YSOs within a peak of the molecular cloud along the southwest rim of the superbubble, indicating that their formation is triggered by the expansion of the bubble. Dawson et al. (2011) analyzed the molecular cloud fraction in and around the galactic supershells GSH 277+00+36 and GSH 287+04–17, and found increased molecular cloud production due to the influence of the supershells, which is the first direct observational evidence of the triggered molecular cloud formation by the supershells.

1.3 Large Magellanic Cloud

Magellanic Clouds (or Magellanic System) are two sets of irregular dwarf galaxies, Large Magellanic Cloud (LMC) and Small Magellanic Cloud (SMC), visible from the southern hemisphere. They are members of our Local Group and are one of the nearest external galaxies orbiting our Milky Way galaxy. Their distances are well defined from the observation of Cepheid variables, Mira variables, and eclipsing-binaries (LMC: $\sim$ 50 kpc (e.g., Pietrzyński et al. 2013), SMC: $\sim$ 60 kpc (e.g., Hilditch et al. 2005)). Since these close location and the relatively face-on inclination to us ($\sim 35°$; van der Marel & Cioni 2001), the Magellanic Clouds are studied in various wavelength with the highest spatial resolution for the external galaxies.

The LMC is consists of the bar and the disk, although it is classified as irregular galaxy in the Hubble sequence. Total mass of the LMC is $\sim 2 \times 10^{10}$ $M_\odot$ (van der Marel & Kallivayalil 2014), with atomic Hydrogen mass of 3×10^8 $M_\odot$ (Luks & Rohlfs 1992), and molecular Hydrogen mass of 1.4×10^8 $M_\odot$ (Cohen et al. 1988). The environments, such as metallicity, in the LMC are different from those in the Galaxy (e.g., $Z \sim 1/2\, Z_\odot$; Dufour Structure and Evolution of the Magellanic Clouds, ed. S. van den Bergh and K. S. de Boer (Dordrecht: Reidel). Stellar clusters called "populous clusters," which are self-gravitating like Galactic globular clusters, are found by photometric studies (e.g., Hodge 1961). This is represented by the famous SSC R136 which is one of the most prominent SSCs in the Local Groups as introduced above. From the NANTEN ^{12}CO(J=1–0) survey, in total 272 GMCs are identified in the LMC (Mizuno et al. 2001, Fukui et al. 2008). This large sample of GMCs gives us a special understanding of the GMC evolution within 20–30 years (Blitz et al. 2007, Kawamura et al. 2009).

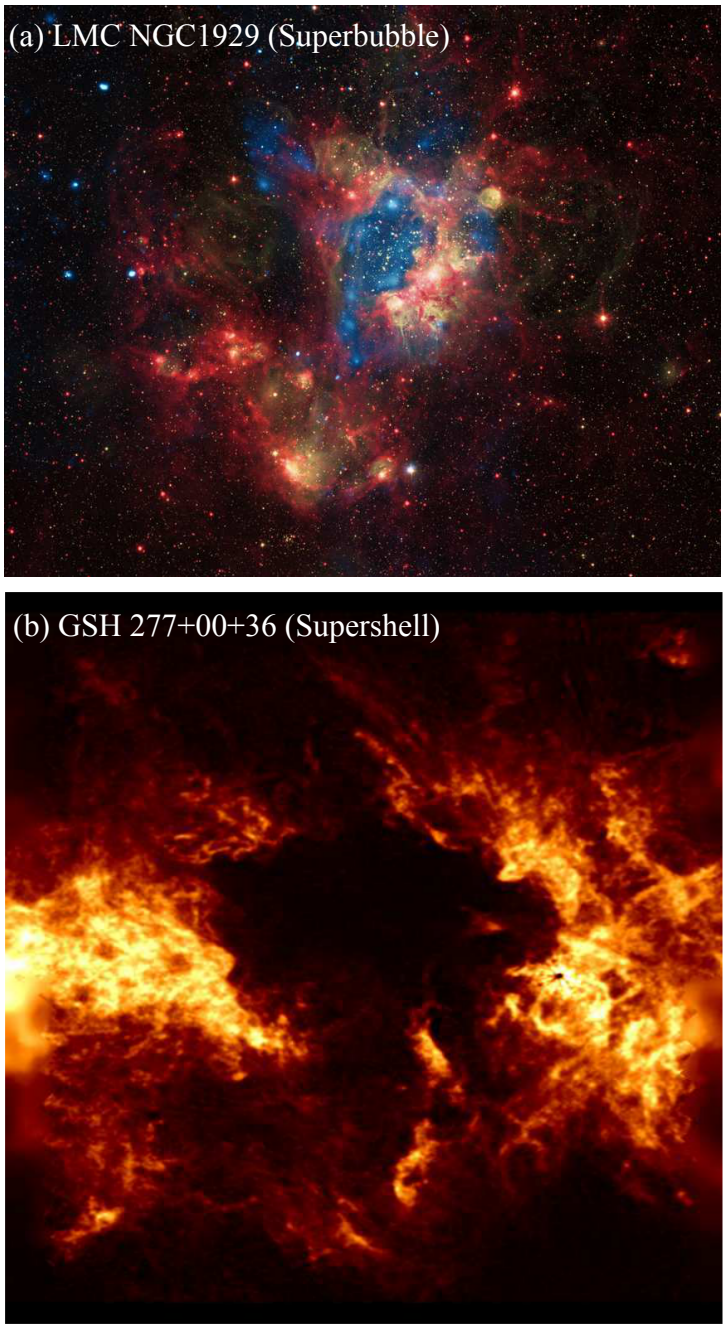

Figure 1.4: (a) 3 color image of superbubble LHα 120–N 44 in the LMC (from Chandra web site). Blue is X-rays by Chandra (NASA/CXC/U.Mich./S.Oey), yellow is optical (ESO/WFI/2.2-m), and red is infrared (NASA/JPL). X-ray (blue) traces hot gas heated by the winds and the shocks, while infrared data (red) outline where the dust and the cooler gas are found. The optical light (yellow) shows ultraviolet radiation from the ionized gas in the nebula. (b) Color image of Galactic supershell GSH 277+00+36 (ATCA and Parkes image in H I by N. McClure-Griffiths and the Southern Galactic Plane Survey team, provided courtesy of CSIRO McClure-Griffiths et al. (2003)). Color scale is H I of the Australia Telescope Compact Array and the Parkes Radiotelescope as part of the Southern Galactic Plane Survey.

1.3.1 Supergiant Shells

One of the prominent feature in the ISM of the LMC is kilo-parsec scale giant holes called as Supergiant shells (SGS: Meaburn 1980, Kim et al. 1999, and for a review see Tenorio-Tagle & Bodenheimer 1988, Dawson 2013). Since the size is quite large, the SGSs usually break out the disk and are seen as giant holes. The requiring input energy is $\gtrsim 10^{53}$ ergs, which is equivalent to the combined energy input of more than 100 typical core collapse supernovae and the stellar winds of their progenitors. The most simple formation model of the SGSs is similar to the supershell case, but it requires much more numbers of supernovae (Weaver et al. 1977, McCray & Kafatos 1987). Other than this simple model, various formation mechanisms of the SGSs are suggested: self-propagating star formation (Domgoergen et al. 1995, Glatt et al. 2010), gamma-ray burst (Efremov et al. 1998), and impacts of high velocity clouds (Tenorio-Tagle 1981).

Figure 1.5 shows the SGSs in the LMC. In the figure, the SGSs identified from the optical morphology (Fig. 1.5(a); Meaburn 1980), and those identified from the H I dynamics (Fig. 1.5(b); Kim et al. 1999, Dawson et al. 2013) are shown. Meaburn (1980) has identified nine SGSs on the Hα plate, by linking the diffuse filaments and the bright H II regions (Fig. 1.5(a)). In contrast to the other Hα shells (most of them are the diffuse H II regions and the superbubbles), these nine SGSs are prominently larger in diameter, typically $\gtrsim$ 600 pc. He also estimated the formation time scale and the expansion velocity of the SGSs as $\gtrsim$ 10 Myr and $\sim$ 10 km s^{-1}, respectively. Kim et al. (1999) have comprehensively identified the shell-like feature by seeing the dynamics of the H I, using their high resolution H I survey data. They identified 23 H I SGSs with diameter greater than the disk thickness ($\sim$ 380 pc). Their estimation of the formation time scale and the expansion velocity suggested the SGSs are rather short lived ($\lesssim$10 Myr with $\sim$ a few $\times$ 10 km s^{-1}), but the expansion features (receding and/or approaching components) are rather ambiguous about a half of the H I SGSs. Dawson et al. (2013) re-analyzed the H I data and identified 11 H I SGSs by rejecting several SGSs of Kim et al. (1999) as false detections, and by refining the positions, velocities, and extents of some others (Fig. 1.5(b))

Impacts of the Supergiant Shells on the Star Formation

Previous observational studies have pointed out that the SGSs, the largest structure formed by stellar feedbacks, do indeed trigger the star formation at their rims. In the LMC, Yamaguchi et al. (2001b) investigated a spatial correlation between the nine Hα SGSs, GMCs identified by NANTEN, and the young clusters (Fig. 1.5(a)). They found that the surface number and the mass densities of the CO clouds are higher by a factor of 1.5–2 at the edge of the SGSs than elsewhere, and young stellar clusters are more actively formed on the side of the CO clouds facing to the center of the SGSs, suggesting that the cluster formation is triggered by the dynamical effects of the SGSs. Book et al. (2009) analyzed the distribution of the Spitzer YSO candidates around

the four Hα SGSs in the LMC. They found the enhancement of the number density of the YSOs at the periphery of the SGSs as the evidence of triggered star formation. Dawson et al. (2013)) examined the molecular fraction in and out of the H I SGSs (Fig. 1.5(b)). They revealed the enhancement of the molecular fraction in five out of nine SGSs (Number 2, 3, 4, 5, and 9), indicating the SGS does on average have a positive effect on the molecular gas fraction. They also argued that $\sim$ 10% of the molecular ISM in the LMC is likely formed as a direct result of the accumulation of the ISM in these expanding superstructures. These studies suggest that the SGSs are the driver of the formation of the molecular clouds and the stars on the size scales of the GMCs (size $\sim$ 10–100 pc, mass $\sim$ 10^5–10^7 $M_\odot$; Fukui et al. 2008). Since the global gravitational instabilities and/or the spiral shocks are not effective drivers of star formation in the interarm regions and the low-mass galaxies, the impact of large-scale stellar feedback upon the star formation and the gas dynamics is considered to be significant (e.g., Mac Low & Ferrara 1999).

It is also notable that the collision of the SGSs is expected to drive violent episodes of star formation, and may be one of the processes by which super-star clusters such as R136 in 30 Doradus are formed (Chernin et al. 1995). In addition, 2D models of colliding supershells suggest that small ($<$ 1 pc), dense (up to 10^4 cm^{-3}), cold ($<$100 K) gas clumps and filaments are formed naturally by thermal instabilities in the highly turbulent and compressed collisional zone (Ntormousi et al. 2011). Since the colliding shell is essentially equivalent to the collision of the dense H I clouds, it triggers the formation of a GMC via the shock of the collision. In the case of the collision of the SGSs, it involves the massive GMC formation since the total mass of the accumulated gas is quite large ($\sim$ kpc shell corresponds to $\sim$ 10^7 $M_\odot$ of diffuse H I gas). And if the GMCs are formed at the rim of the shell before the collision, the shell collision can be a driver of the cloud-cloud collision and triggers the formation of massive stellar clusters (see the model of Inutsuka et al. 2015).

The N48 and N49 Region: Interface of two SGSs

The star forming regions N48 and N49 in the LMC (Henize 1956), which are located between two optically identified SGSs, LMC 4 and LMC 5 (Meaburn 1980:see also Figure 1.6). This situation is similar to 30 Doradus, including the R 136 cluster, which is located toward the interface between two SGSs, LMC 2 and LMC 3 (Tenorio-Tagle & Bodenheimer 1988). Both LMC 4 and LMC 5 consist of diffuse Hα filaments and bright H II regions (Meaburn 1980), and giant holes in the H I gas (Dopita et al. 1985, Kim et al. 1999) and interstellar dust (Meixner et al. 2006). LMC 4 is the largest SGS in the LMC, with a size of 1.0×1.8 kpc in Hα (Meaburn 1980), and LMC 5 is located northwest of LMC 4 with a diameter of $\sim$ 800 pc in Hα (Meaburn 1980). Of all SGSs in the LMC, the LMC4/LMC5 region shows the strongest evidence for the enhanced formation of molecular clouds due to the action of the shells on the ISM (Dawson et al. 2013).

The current expanding motions of LMC 4 and LMC 5 are investigated from the

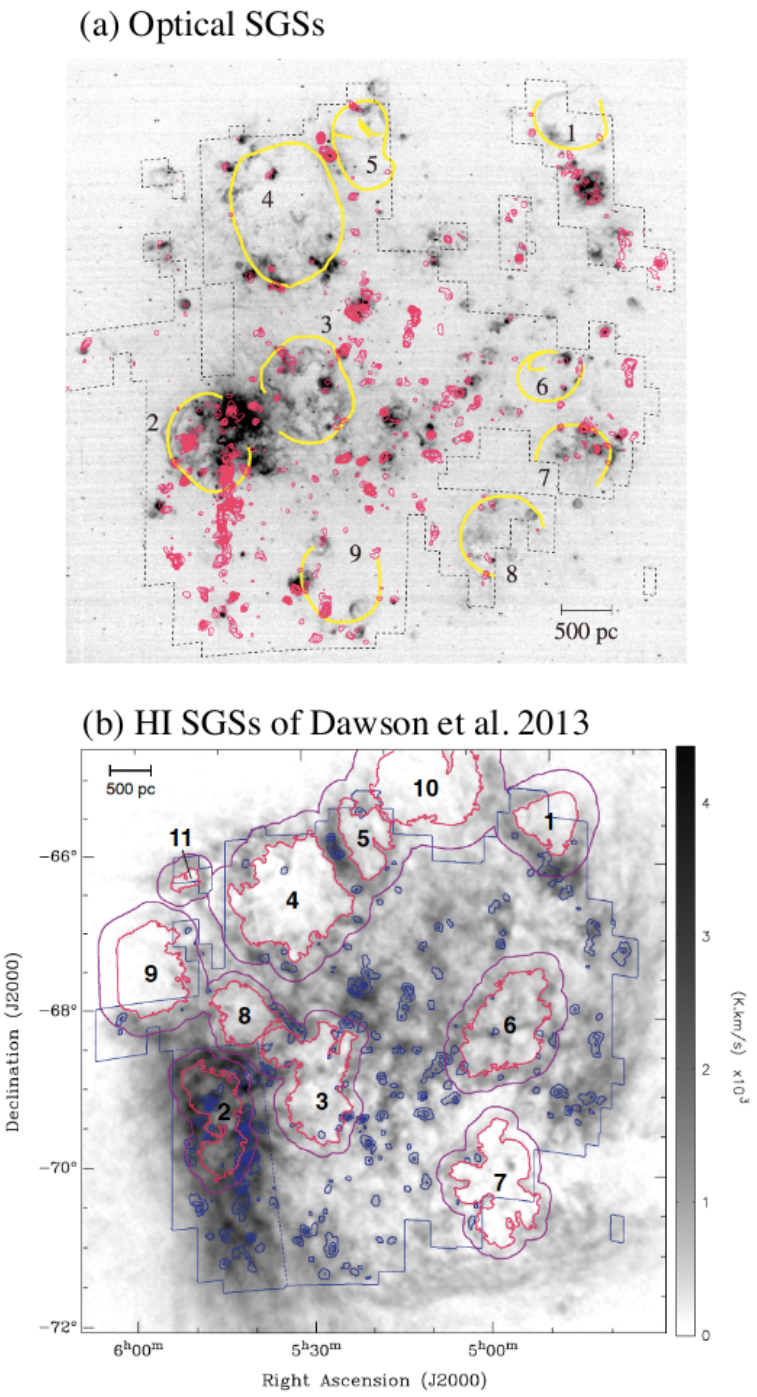

Figure 1.5: (a) Figure 1 of Yamaguchi et al. (2001b). Grayscale image is Hα flux, and red contours are the NANTEN CO. Nine optically identified SGSs (Meaburn 1980) are shown in yellow lines. (b) Figure 1 of Dawson et al. (2013). Grayscale image is H I integrated intensity of Kim data smoothed to a resolution of 2.6′, and blue contours are the NANTEN CO. Eleven H I SGSs that are identified them are shown by dark pink lines (inner rims) and purple lines (outer boundaries).

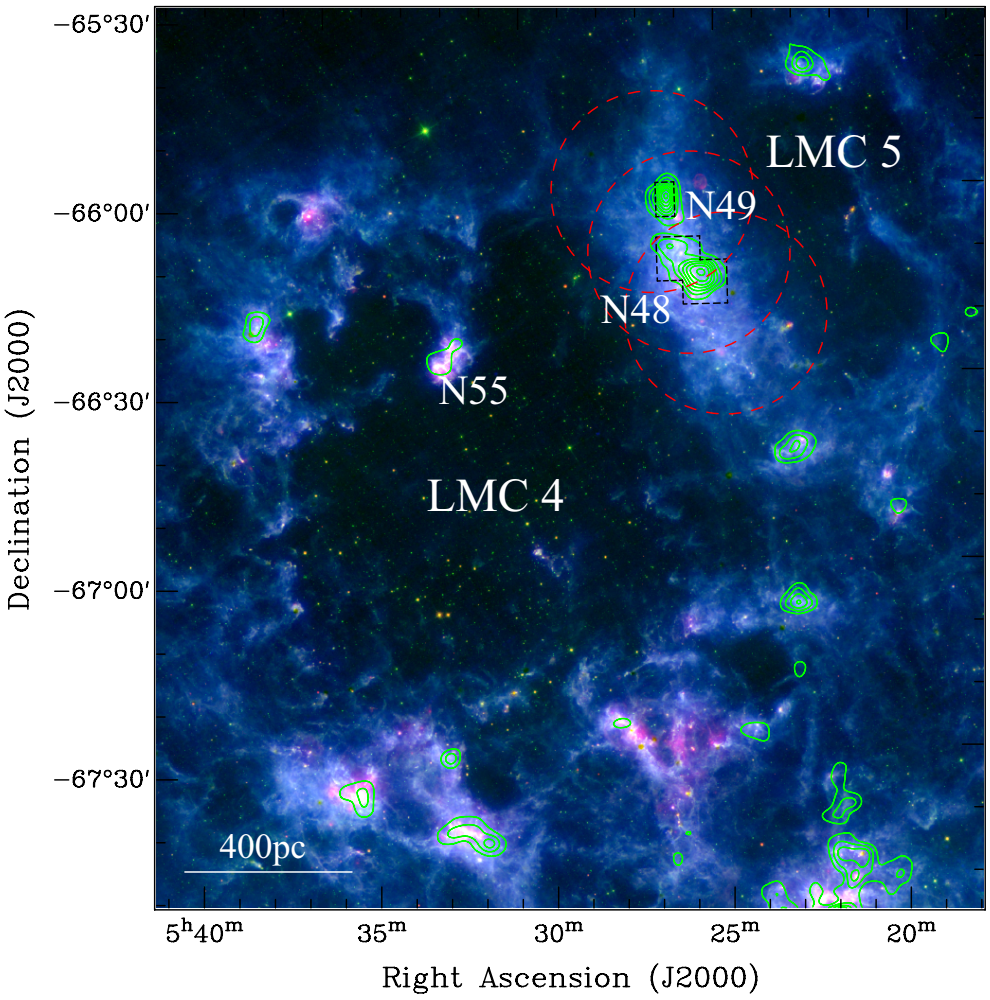

Figure 1.6: Spitzer three-color image (R: 24μm, G: 8.0μm, B: 160μm; Meixner et al. 2006) of LMC 4 and LMC 5. Green contours are the NANTEN ^{12}CO(J=1–0) integrated intensity (Fukui et al. 2008). The contours start at 1.2 K km s^{-1} and are incremented in steps of 1.2 K km s^{-1}. Black dashed lines indicate the region observed with the ASTE, and red dashed circles are three position of the mosaicking with the ATCA (for detail see §2.1.1 and 2.3.1).

kinematics of H I gas (Dopita et al. 1985, Kim et al. 1999, Book et al. 2008). With low resolution H I data, the expanding velocity of LMC 4 is roughly estimated to 36 km s^{-1} by fitting a velocity ellipsoid in the velocity-projected distance space (Dopita et al. 1985). With 60″ resolution interferometer data, Kim et al. (1999, 2003) examined the expanding velocity of the SGSs by seeing approaching and receding components in the position velocity diagrams. Although the expansion velocity of LMC 4 was estimated to 36 km s^{-1} that is the same value as previous study, the expansion velocity of LMC 5 could not be derived in this work. Book et al. (2008) have re-analyzed the H I kinematics of the optically identified SGSs in the LMC using the Kim data, and estimated the expanding velocity of the shells by seeing the position velocity diagrams. As opposed to Kim et al., these authors have concluded that there is no expansion feature for LMC 4, but LMC 5 is expanding with velocity of $\sim$ 30 km s^{-1}. So the current expanding motions of LMC 4 and LMC 5 in the H I gas dynamics are somewhat controversial, but they are roughly estimated in the order of 10 km s^{-1}.

The dynamical ages of LMC 4 and LMC 5 have been estimated as 4–15 Myr, and 5–7 Myr, respectively, using the current observed expansion velocities of the H I gas (Dopita et al. 1985, Kim et al. 1999, Book et al. 2008). However, these dynamical ages give roughly lower limits for the shell formation timescales, because these are derived under the assumption that the SGS is formed as a single expanding shell by feedback from a single generation of stellar clusters. There is alternative theory that the large SGSs might be formed by several generations of star formation (Efremov & Elmegreen 1998), and the age estimates based on stellar population studies in individual SGSs have indicated ages of typically 10–20 Myr (e.g., Dopita et al. 1985, Points et al. 1999, Glatt et al. 2010). Particularly in LMC 4, there is an extended stellar arc ($\sim$ 600 pc) in Constellation 3, which is located in the central area of the H I hole, and it has been argued that this arc was formed in the gas swept up by the first generation stellar feedback within the triggering timescale of $\sim$ 14 Myr (Efremov & Elmegreen 1998). The arc itself is also an energy source via second generation stellar feedback. Thus, the ages of the two SGSs are in the order of 10 Myr.

In the N48, N49 regions, two massive GMCs whose total mass is $\sim 1.5\times10^6$ $M_\odot$ have been identified with the NANTEN telescope (catalogued alternatively as LMC/M5263–6606 and LMC/M5253–6618 in Mizuno et al. (2001), or LMC N J0525–6609 in Fukui et al. (2008)). These GMCs are located within a high column density H I envelope that is distributed more than 500 pc long like a large-scale ridge between the two SGSs . Since they correspond to 50% of the total mass of molecular clouds associated with LMC 4 (Yamaguchi et al. 2001a), and the region shows a high ratio of molecular to atomic gas ($\sim$ 60%; Mizuno et al. 2001), they are considered to have formed efficiently within the dense H I ridge swept up by the two SGSs. Although they contain small H II regions (N48) and a single SNR (N49), both of them are located at the peripheries of the GMCs. Therefore they are considered to be early-stage cluster-forming clouds Mizuno et al. 2001. In addition, Cohen et al. (2003) have identified a large, dense ridge-shaped photodissociation region that lies between the two SGSs, and argued that the feature is a strong candidate for secondary star formation by the interaction of two

SGSs. These regions are excellent targets in which to investigate how the action of SGSs and their interaction affect the physical properties of dense molecular clumps.

1.4 Goal of This Thesis

1.4.1 Scientific Aspects

A main goal of this thesis is to prove the theoretical prediction of the GMC formation mechanism by the observations. Observational studies of the GMC formation are now aspired. As discussed above, several times of shock compressions are required to form molecular clouds from diffuse ambient medium. Although there are a lot of theoretical works that argue the GMC formation via shocks such as converging flows, there are few observational works that focus on the physics and the kinematics of the atomic medium to the GMCs. In the large-scale case, there are three possible drivers of the shocks; global instability, spiral arms, and expanding shells and bubbles, as seen in section 1.1.4. First two drivers are equivalent to the large-scale accumulation of the material by the spiral structure of the galaxy. The spatial correlation between the GMCs and the spiral arms have been observationally confirmed in the external galaxies (for example M51; e.g., Schinnerer et al. (2013)), indicates that the GMCs are more effectively formed at the spiral arms. For the expanding shells, Dawson et al. (2013) have clarified that the molecular fractions are certainly heightened around the rim of the SGSs, but only $\sim$ 12–25% of the molecular mass can apparently be attributed to the formation for presently visible shell activity. These studies suggest that the large-scale structure of the galaxy surely works on the formation of the GMCs in the galaxy. However, these studies have not discussed the formation process of the GMCs itself, do these GMCs are actually formed by the arms or shells, and how the GMCs are formed from the atomic medium. This is partly because the correlation between the detailed kinematics of the GMC formation and the large-scale structure is difficult to prove.

The importance of the gravitational evolution and the H I mass accretion to the GMCs are still controversial (e.g., Inutsuka et al. 2015), As mentioned before, Fukui et al. (2009) have performed statistical analysis of the dynamical correlation between the GMCs and their H I envelopes with the entire sample of the GMCs in the LMC with 40 pc resolution. One of the important implications of their work is that the H I envelopes are gravitationally bound to the GMCs, and the GMCs seem to increase their mass via continuous H I accretion over a timescale of $\sim$ 10 Myr within a mass accretion rate of 0.05 M yr^{-1}. This is good observational evidence of the gravitational evolution of the GMCs on the scales of $\sim$ 50–100 pc.

Colliding shells may offer the good laboratory to investigate the kinematics of the GMC formation. Typical velocity of the shocks in the theoretical works is estimated to be on the order of 10 km s^{-1}. Observed expansion velocity of the supershell is also on the order of 10 km s^{-1} (e.g., Kim et al. 1999), and also the propagation speed of the shocks drived by stellar feedback is (Hosokawa & Inutsuka 2006, since it is essentially

determined by the sound speed of ionized gas with temperature of $\sim 10^4$ K). In our galaxy, Dawson et al. (2015) have investigated the origin of the GMC at the stagnation point of the two supershells–GSH 287+0417 and the Carina OB supershell. They argued that the GMC is pressure confined and is formed from a combination of warm atomic gas together with some pre-existing denser material, indicates the presence of previous shock compressions. For the external case, the N48 and N49 regions in the LMC are the only one site of colliding Supergiant Shells (see §1.3.1). Although the spatial agreement of the GMC and the two shells is the clearest, the kinematic aspects of the GMC formation, like how the diffuse WNM is converted to the observed GMCs, are still unclear and untouched in these regions.

One notification here is that the colliding shell is not a special case of the possible GMC formation process; but just a one aspect of the interstellar colliding flows, i.e., the interstellar shocks. Observationally unveiling the kinematics of the GMC formation process at the shell colliding area will lead to the general understanding of the GMC formation in the galaxy.

1.4.2 Goals and Methods

In this thesis, observational study of the colliding large expanding shells is carried out in order to understand the GMC formation scenario from diffuse atomic medium. The N48 and N49 regions in the LMC are selected as the best laboratory of the detailed observational study of gas dynamics at the shock compressed area.

Questions to be answered in this study are as follows:

- Do colliding flows actually induce the formation of GMCs from the ambient neutral medium?
- What are the characteristics of the morphology of the gas and the clouds at the colliding area? Are they filamentary or clumpy, or taking more complicated distribution?
- How are the GMCs formed at the SGSs colliding area? Is just a collision induced instability enough for their formation, or further evolution by mass accretion of ambient atomic medium necessary?

To answer these questions, high resolution observations of H I 21 cm line is carried out toward the H I ridge in the N48 and N49 regions. Not only the atomic Hydrogen gas is important as the pre-GMC phase medium, but it is the best tracer of the dynamics of large expanding shells since it is diffuse and comprises the bulk of the ambient interstellar medium. The detailed kinematic structure and the dynamics of the ridge will be discussed with this high-resolution H I data, and then they will be compared with the morphology and the physical state of the molecular clumps. Through the analysis using these data sets, I aim to construct a scenario of the GMC formation process of this area, as the first case study of the H I kinematics around the GMCs.

In Chapter 2, the detailed information of the observations and the data reductions that are performed for this thesis is summarized. At first, CO transition line observations with the ASTE and the Mopra telescope are mentioned. Then, H I line observation of the ATCA is introduced, including interferometric imaging and data combine with single dish data. In Chapter 3, the main results of the observations are summarized. For the CO data sets, the physical properties of the molecular clumps in the N48 and N49 regions are reviewed that are necessary to understand their formation process. For the H I data sets, specific morphological characteristics of the high resolution H I map and the channel maps are shown. In Chapter 4, three physical analyses of the H I data are introduced. First one is the opacity correction of the H I using the archival dust opacity data. Second one is the identification of filamentary features that can be seen in the high-resolution H I channel maps. The last one is the large scale gas dynamics of the ridge that is revealed by the position velocity diagrams. In Chapter 5, the possible GMC formation process in this region is proposed and discussed. The summary of this thesis is shown in Chapter 6.

Chapter 2

Observation

In this section, details of observations that are performed for this study are summarized. Three telescopes were used in this thesis, ASTE, Mopra, and ATCA.

2.1 ASTE Observation

The Atacama Sub-millimater Telescope Experiment (ASTE) is a 10 m radio telescope at Pampa la Bola in Chile (Ezawa et al. 2004). The ASTE has a unique capability to perform high sensitivity observation at sub-millimater wavelength (0.1 to 1 mm) in southern hemisphere, prior to the ALMA. The typical half-power beam width is measured to be 22″ at 345 GHz by observing the planets.

2.1.1 ^{12}CO(J=3–2) Observation

Observations of the ^{12}CO(J=3–2) transition towards the N48 and N49 regions were made with the ASTE 10 m telescope, in September 2006 and September 2011, respectively. Both observations were performed in the On-the-fly (OTF) mapping mode.

In 2006, the giant molecular cloud LMC/M5263–6606 (Mizuno et al. 2001) in the N49 region is observed. The size of the ^{12}CO(J=3–2) mapped area was 3.0′ × 5.5′ (45 × 83 pc), which covered the entire cloud. Along each row of the OTF field, individual spectra were recorded every 1.5″ and the spacing between the rows was 6″, so that the 22″ beam of the telescope was oversampled. The OTF scan was performed along the right ascension and declination directions. In this period, a single cartridge-type double-side-band (DSB) SIS receiver, SC345 (Kohno 2005) is installed. The spectrometer was an XF-type digital autocorrelator MAC (Sorai et al. 2000) and the wide-band mode with a bandwidth of 512 MHz with 1024 channels is used. The corresponding velocity coverage and channel spacing were 450 and 0.44 km s^{-1} at 345 GHz, respectively. The chopper-wheel technique was employed to calibrate the antenna temperature $T_{\rm a}^{*}$. The typical system noise temperature including atmospheric effects during the observation was $\sim$ 500 K in DSB. The typical pointing error was measured to be within 5″

(peak to peak) by observing the CO point sources R Dor ($\alpha_{\rm B1950}$ = 4h 36m 45.84s, $\delta_{\rm B1950} = -62^\circ\ 04'\ 35.70''$) or o Cet ($\alpha_{\rm B1950}$ = 2h 19m 20.8s, $\delta_{\rm B1950} = -2^\circ\ 58'\ 40.70''$) every two hours during the observing period. N159W ($\alpha_{\rm B1950}$ = 5h 40m 3.7s, $\delta_{\rm B1950} = -69^\circ\ 47'\ 00.0''$) is also observed every two hours to check the stability of the intensity calibration. The average and the standard deviation of the antenna temperature $T_{\rm a}^*$ of N159W was 5.48 ± 1.42 K. So the intensity variation during the observation was estimated to be less than 26%. The observational data taken in 2006 is scaled to $T_{\rm mb}$ scale with a scaling factor of 2.538 so that the average value of observed $T_{\rm a}^*$ of N159W is consistent with the main beam temperature of N159W $T_{\rm mb}$ = 13.9 ± 0.7 K, which was estimated by Minamidani et al. (2011).

In 2011, the giant molecular cloud LMC/M5253–6618 (Mizuno et al. 2001) in the N48 region was observed. The cloud was covered by two OTF area of $7' \times 7'$ (105 × 105 pc) square. The separation of spectra records was $1.6''$ and the spacing between the each OTF row is $7.5''$, so that the $22''$ beam of the telescope is oversampled. The mapping was performed both along the right ascension and declination directions. In this period, the waveguide-type sideband-separating SIS mixer receiver for single side band (SSB) operation, CATS345 (Ezawa et al. 2008, Inoue et al. 2008) was used. The image rejection ratio at 345 GHz was estimated to be ∼ 10 dB. The spectrometer was an XF-type digital autocorrelator MAC (Sorai et al. 2000) and the high-resolution mode was used, which has a bandwidth of 128 MHz with 1024 channels. The corresponding velocity coverage and the channel spacing at 345 GHz were 125 and 0.11 km s^{-1}, respectively. Typical system noise temperatures including atmospheric effects during the observation were 500 K in SSB. The pointing error was measured to be within $5''$ by observing the CO point source R Dor every two hours. N159W was also visited every two hours to check stability. The average and standard deviation of the antenna temperature was found to be 7.58 ± 0.26 K on a $T_{\rm a}^*$ scale. The intensity variation was therefore estimated to be less than 3%. The observational data in 2011 was scaled to $T_{\rm mb}$ scale with scaling factor of 1.835.

Both data were reduced with the software package NOSTAR, which comprises tools for the OTF data analysis, developed by the National Astronomical Observatory of Japan (Sawada et al. 2008). Linear baselines were subtracted from the spectra. The raw data were re-gridded to $10''$ per pixel, and smoothed by Bessel∗Gaussian smoothing kernel of FWHM $20''$. This gives an effective spatial resolution of approximately $27''$, which corresponds to 7 pc at the distance of the LMC. The data sets taken along the right ascension and declination directions were co-added by the Basket-weave method (Emerson & Graeve 1988) to remove any effects of scanning noise. In addition a fifth order polynomial function was fitted to the baseline and subtracted in order to reduce the effects of baseline ripples. The 2011 data was binned to a channel spacing of 0.44 km s^{-1}, which corresponds to the channel spacing of the MAC wide-band mode used in the 2006 data.

2.1.2 ^{13}CO(J=3–2) Observation

Observations of the ^{13}CO(J=3–2) transition were made with the ASTE in August 2013. Seven peaks of ^{12}CO(J=3–2) molecular clumps in the N48 and N49 regions were covered by $2' \times 2'$ OTF patch (N48–Clump–1) and 9 points (3×3) position switching observation (N48–Clump–2, 3, 0, 6, 7, and N49–Clump–1) (for clump number see Table3.1). The aim of this 9 points observation is to derive 45″ beam ^{13}CO(J=3–2) intensity towards each clump peak, in order to calculate intensity ratio with the Mopra results with 45″ beam. Separation of each point was set to 20″.

In this period the receiver and the spectrometer were the same as 2011 observation (CATS345 and MAC). The spectrometer was operated in the high-resolution mode with a bandwidth of 128 MHz with 1024 channels, which corresponds to the velocity coverage and the channel spacing 125 and 0.11 km s^{-1}, respectively at 330 GHz. Typical system noise temperatures during the observation were 500 K in SSB including atmospheric effects. The pointing error was within 5″, which was measured by observing the CO point source R Dor every two hours. N159W was also observed every two hours to check stability of detected intensity. The $T_{\rm a}^*$ scale average and standard deviation of the antenna temperature was found to be 2.2 ± 0.1 K. The intensity variation during the observing period was therefore estimated to be less than 3%. The observational data is scaled to $T_{\rm mb}$ scale with scaling factor of 1.455 so that the observed $T_{\rm a}^*$ of N159W is consistent with the main beam temperature of N159W $T_{\rm mb}$ = 3.2 ± 0.3 K (Minamidani et al. 2011).

The data was reduced with the software package NEWSTAR, which comprises tools for the position switch data analysis, developed by the National Astronomical Observatory of Japan (Sawada et al. 2008). Linear baselines were subtracted from the spectra. Weighted average (1/rms^2) was taken of data at the same point. Gaussian smoothing was applied to the reduced data in order to convolve the data to 45″ beam. The data was also binned to a channel spacing of 0.44 km s^{-1}, which corresponds to the channel spacing of the other CO data.

2.2 Mopra Observation

The Mopra telescope is a 22 m radio telescope located at the edge of the Warrumbungle Mountains near Coonabarabran in Australia. It is part of the Australia Telescope National Facility (ATNF), operated by the CSIRO. Mopra is equipped with three receivers for the single-dish observation, 3 mm band, 7 mm band, and 12-mm band. And the spectrometer allows to cover 8 GHz band, which can be split four 2.2 GHz sub-band and sixteen 138 MHz zoom bands (four in each sub-band). Mopra is a unique single dish telescope that has a capability to observe lowest transition of CO rotational line in southern hemisphere. The half-power beam width at the 3 mm band is 33″.

Figure 2.1: The photo of the ASTE (taken by author).

2.2.1 ^{12}CO(J=1–0) and ^{13}CO(J=1–0) Observations

Observations of the ^{12}CO(J=1–0) and ^{13}CO(J=1–0) transitions using the Mopra telescope in June to July 2012. Eleven $2' \times 2'$ areas covered the prominent parts of the ^{12}CO(J=3–2) clumps. The observations were performed in the OTF mapping mode. The individual spectra were recorded every $6''$ and the spacing between rows wass $9''$, so that the $33''$ (FWHM) telescope beam was oversampled.

The 3mm MMIC receiver was used, that can simultaneously record dual polarization data. The spectrometer was the Mopra Spectrometer (MOPS) digital filter bank. It was used in the zoom-band mode, which can record up to sixteen 137.5 MHz zoom bands positioned within an 8 GHz window. The spectrometer provided a velocity coverage and channel spacing of 376 km s^{-1} and 0.09 km s^{-1} at 3 mm, respectively. Typical system noise temperatures during the observations were 600 K at the frequency of the^{12}CO line, and 250 K at the frequency of the ^{13}CO line, including atmospheric effects. The pointing error was measured to be within $10''$ by observing the SiO maser of R Dor ($\alpha_{\rm J2000}$ = 4h 36m 45.61s, $\delta_{\rm J2000} = -62^\circ\ 04'\ 37.92''$) every one to two hours during the observing period. Orion KL ($\alpha_{\rm J2000}$ = 5h 35m 14.5s, $\delta_{\rm J2000} = -5^\circ\ 22'\ 29.56''$) was also observed once a day to check the stability of the intensity calibration. The average and the standard deviation of Orion KL antenna temperatures was 47.9 $\pm$ 3.1 K in $T_{\rm a}^*$ scale, then the intensity variation during the observation was estimated

Figure 2.2: The photo of the Mopra (from the Mopra website, Credit: CSIRO).

to be less than 7%. The beam efficiencies assumed for CO are the "extended beam efficiency" $\eta_{\rm xb}$ discussed by Ladd et al. (2005), which includes the effects of coupling to the inner error beam for sources larger than $\sim 2'$. We determined $\eta_{\rm xb} = 0.48$ by dividing the observed peak antenna temperature by 100 K, which is the corrected peak CO main beam temperature for Orion KL given by Ladd et al. (2005).

Data reduction was performed using the ATNF's *Livedata*, and *Gridzilla* software packages. *Livedata* performs off-source subtraction from the original on-source spectra, then fits and subtracts a linear baseline. *Gridzilla* takes the spectra and grids them onto a data cube using a Gaussian smoothing kernel of FWHM $33''$, comparable to that of the Mopra primary beam. The spectra were weighted by the inverse of the system temperature when gridding. The resulting effective spatial resolution is approximately $45''$, which corresponds to 11 pc at the distance of the LMC. Then a fifth order polynomial function was fitted and subtracted from the baseline to reduce the effects of baseline ripples. The channel width was binned up to 0.44 km s^{-1}, which matches the channel spacing of ASTE data. Finally, the data was re-gridded to a spacing of $10''$ (to match with the ASTE grid) using the ATNF's *MIRIAD* software.

2.3 ATCA Observation

The Australia Telescope Compact Array (ATCA) is an array of six 22m diameter antennas located at the Paul Wild Observatory near Narrabri. The ATCA is also a part of the Australia Telescope National Facility (ATNF), operated by the CSIRO. The

array has a T-shape tracks of a 6 km-long east-west track (3 km for each direction) with a 214m northern spur. Five antennas can be moved along these tracks. The sixth antenna at a fixed position 3 km to the west of the east-west track, therefore the longest possible baseline is 6 km. The array can be used for observations in five wavelength bands between 27 cm and 3 mm, between frequencies of approximately 1.1 GHz and 105 GHz. The ATCA is a unique interferometer that can observe 21cm line of atomic Hydrogen in southern hemisphere, prior to the ASKAP and the SKA. The ATCA primary beam at 1.419 GHz is $34'$.

Figure 2.3: The photo of the ATCA (from the ATCA website, Credit: CSIRO).

2.3.1 21 cm Observation

The ATCA observations were performed towards the N48 and N49 regions on 27th January(1.5B configuration); 1st May (1.5D); and 7th November 2014 (1.5A). The targeted region was mosaicked in 3 pointing centers separated by 16.8 arcminutes (Fig. 1.6). The observation time per day was 12 hours (January 27, November 7) and 10 hours (May 1), which provides excellent u-v coverage for each array configuration. Each pointing centre was observed for 20 seconds at a time, and the full set of three positions were observed 20 times between each standard calibrator scan. The primary calibrator, PKS B1934-638 (assumed flux density 14.9 Jy at 1.419 GHz), was observed for bandpass and absolute flux-density calibration with 5 minutes integration at the start of each observing day. The secondary calibrators, PKS B0515-674 (assumed flux density 1.18 Jy at 1.419 GHz) and PKS B0407-658 (assumed flux density 15.5 Jy at 1.419 GHz) were observed for gain and phase calibration. PKS B0515-674 was observed every 40 minutes with 5 minutes integration time (January 27th), and PKS B0407-658 was observed in every 60 minutes with 2 minutes integration time (May 1st, November 7th). The Compact Array Broadband Backend (CABB) was tuned for the CFB 1M-0.5k mode, which provides a bandwidth of 2 GHz with 2048 1-MHz channels and a fine resolution of 0.5 kHz (2048 channels across 1 MHz) in up to 16 zoom bands in each IF. The observing band was the zoom band centered on 1.419 GHz, which is centred on the source velocity (local standard of rest) of 285 km s^{-1} with a coverage of 211.3 km s^{-1} per zoom band. The intrinsic velocity resolution is 0.1 km s^{-1}.

Shorter baselines have been provided by archival observations with the EW352 and 750A array configurations that cover the entire the LMC 5 region, including the N48 and N49 regions (project C2648, Ann-Mao, S.A., Dawson, J.R. et al.). Including these shorter baseline data sets, the number of different baselines is 42, ranging from 31 m to 1469 km.

Calibration and imaging were performed using standard routines from the ATNF ' s *MIRIAD* software package (Sault & Killeen 2009). Calibration, 0th-order polynomial baseline subtraction, and Doppler correction were carried out in the u–v domain. The individual pointings were linearly combined and imaged using the *MIRIAD* task *INVERT*; a standard grid and fast Fourier transform technique. A Brigg 's visibility weighting robustness parameter of 0.5 was adopted. Deconvolution was performed using the maximum entropy-based deconvolution algorithm *MOSMEM* (Sault et al. 1996), and the images were restored using the task *RESTOR*. The pixel size of the image is 10″, and the velocity channel width is 0.4 km s^{-1}. The effective beam size is 24.75 by 20.48 arcsec with a position angle of −35 degrees.

Zero spacing data is provided by Parkes 64-m Radio Telescope archival data from the Galactic All-Sky Survey (GASS; McClure-Griffiths et al. 2009, Kalberla et al. 2010). GASS is a 21-cm line survey covering the southern sky for all declinations $\delta \lesssim 1°$, including entire the LMC area, with a velocity range of $|V_{\rm lsr}| \lesssim 468$ km s^{-1}. The intrinsic FWHM beam size of the data is 14.4′ (FWHM) and the effective velocity resolution is 1.0 km s^{-1}. The GASS data were regridded to match the ATCA data,

and the two were then linearly combined in the Fourier domain using the *MIRIAD* task *IMMERGE*. In order to perform the combination of the Parkes and the ATCA observations, we need to ensure that the flux calibration between the two data types are consistent. This calibration factor has been estimated by examining data in the Fourier plane between 20 and 50 m–data in this annulus are well measured by the Parkes and mosaicked ATCA observations. Before calibration, it is necessary to extract the area of high resolution data in order to get a better calibration of these data sets. A rectangle area with bottom left position of [5h 29m 30.83s:−66° 35′ 47.7″] and top right position of [5h 22m 9.16s:−65° 44′ 44.7″] is extracted ($\sim 34' \times 52'$ area, corresponds to 500×800 pc at the LMC distance). This box is corresponds to the least size rectangle that can contain total area of HPBW field of view of three mosaic points. Then the Single dish and interferometer data are combined by *IMMERGE*. A scale factor of 1.125 is required to scale the single dish image, so the calibration of the two data sets goes quite well within a reasonable calibration factor.

Finally, the unit of the is converted to Kelvin using following relation,

$$T_{\rm B}\,[{\rm K}] = 1.222 \times 10^6 \left(\frac{\theta_{\rm maj}}{\rm arcsec}\right)^{-1} \left(\frac{\theta_{\rm min}}{\rm arcsec}\right)^{-1} \left(\frac{\nu}{\rm GHz}\right)^{-2} (S\,[{\rm Jy/Beam}])\,. \qquad (2.3.1)$$

For the 24.75 by 20.48 arcsec beam, conversion coefficient is $\sim 1.198 \times 10^3$.

2.3.2 Flux Consistency

For the LMC, there is an archival H I survey data taken with the Australia Telescope Compact Array (Kim et al. 1998) and the Parkes single-dish telescope (Staveley-Smith et al. 2003), combined by an image feathering (linear merging) approach (Kim et al. 2003, hereafter Kim data). The data cube covers the entire LMC at a spatial resolution of 60″ and a pixel size of 20″, and has a 1σ noise level of 2.4 K in a 1.65 km s^1 velocity channel. Flux consistency between the Kim data with high resolution data of this work (hereafter new data) should be checked, since although the used telescopes are the same, the spacing of the interferometer is different each other. Before the comparison, the beam size of the new data is smoothed to 60″, and spatial grid of the Kim data is unified to the new data (10″).

Total flux of the new data within a rectangle area defined above is 3.5×10^5 Jy/Beam km s^{-1}, and that of the Kim data is 3.9×10^5 Jy/Beam km s^{-1}. Note that here the unit of the data is Jy/Beam, not Kelvin, in order to eliminate unnecessary error due to the different conversion factor to Kelvin between the two data. Total flux of the Kim data is more than 10% greater than the new data. This is due to negative side-lobes of the new data. Negative side-lobes are appeared in the new data because the large dynamic range of H I between the ridge and the cavity of the shells, within a small area covered by three mosaic points. If the negative components in the cavity of the shell are masked, total flux is quite consistent between the two data sets.

Figure 2.4 is a pixel to pixel comparison of H I integrated intensity (Jy/Beam km s^{-1}) of the new data and the Kim data (hereafter $W_{\rm new}$ and $W_{\rm Kim}$). The correlation

of these two data sets is quite well within a best fit line of $W_{\rm Kim} = 0.98 W_{\rm new} + 0.55$ with correlation coefficient 0.73. Note that the 3σ rms noise level is ~ 0.26 Jy/Beam km s^{-1} for both data. In the low intensity area ($\lesssim 3$ Jy/Beam km s^{-1}), the intensity difference is quite large more than a factor of 2. This is due to the low accuracy of the new data in intensity recovery around the negative side-lobes. From middle intensity area ($\gtrsim 5$ Jy/Beam km s^{-1}), the difference of two data sets is typically within 10% ($\lesssim$1 Jy/Beam km s^{-1} at 10 Jy/Beam km s^{-1}). In total, the flux recovery of high resolution data is consistent with the previous archival data.

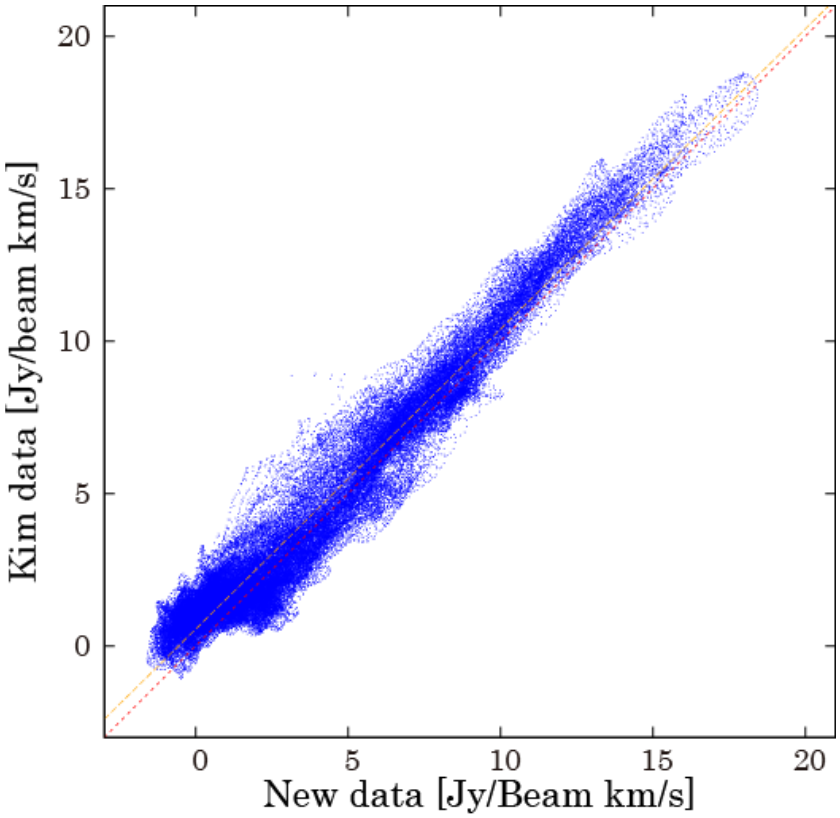

Figure 2.4: A pixel comparison plot of H I integrated intensity (Jy/Beam km s^{-1}) between the new data and the Kim data (Kim et al. 2003). The spatial grid (and the map area) is unified to the new data. The beam size of the new data is smoothed to $60''$ that is the beam size of the Kim data. Red line is $W_{\rm Kim} = W_{\rm new}$, and orange dotted line is the best fit line, $W_{\rm Kim} = 0.98 W_{\rm new} + 0.55$.

Chapter 3

Results of the Observations

3.1 Results of the ASTE Observation

3.1.1 Review of the ASTE ^{12}CO(J=3-2) Results

In this section, the main results of ASTE ^{12}CO(J=3-2) is reviewed. The major results are reported in Fujii et al. (2014). The results that are important for the discussion of this paper and a few additional analyses are introduced here.

Main Results

Figure 3.1(a) shows the ^{12}CO(J=3–2) integrated intensity image of the N48 and N49 regions. With higher resolution and higher density tracer observation, the GMCs are revealed to consist of a lot of molecular clumps. Total luminosity of ^{12}CO(J=3–2) is 4.3×10^4 K km s^{-1} pc^2 for the N48, and 1.1×10^4 K km s^{-1} pc^2 for the N49. These corresponds to the luminosity H_2 mass of 6.6×10^5 $M_\odot$ and 1.4×10^5 $M_\odot$, respectively, assuming that the CO-to-H_2 conversion factor of 7×10^{20} cm^{-2} (K km s^{-1})$^{-1}$ (Fukui et al. 2008), and mean CO(J=3–2) to CO(J=1–0) intensity ratios of 1.0 and 0.8 respectively (see §3.1.1). Total detected luminosity mass is about a half of the total mass of the GMCs in the previous ^{12}CO(J=1-0) observation ($\sim 1.5 \times 10^6$ $M_\odot$ for NANTEN and SEST; Fukui et al. 2008, Yamaguchi et al. 2001a, and $\sim 1.3 \times 10^6$ $M_\odot$ for Mopra; Wong et al. 2011). This indicates that total mass of the dense clouds is about a half, and remaining half is diffuse envelope of the clouds in these regions.

To discuss the physical properties, ^{12}CO(J=3–2) clumps are identified in the way described in Minamidani et al. (2008). Identification criteria are as follows: (1) Identify local peaks in the integrated intensity map that are greater than the 10 σ noise level ($\geq$4.0 K km s^{-1} for the N48 region, and $\geq$6.8 K km s^{-1} for the N49 region). (2) Select those local peaks that have a peak brightness temperatures greater than the 3 σ noise level of the spectrum ($\sim$ 0.90 K for the N48 region, and $\sim$ 1.0 K for the N49 region), then draw a contour at one-half of the peak integrated intensity level and identify it as a clump unless it contains other local peaks. (3) When there are other local peaks

inside the contour, draw new contours at the 70% level of each integrated intensity peak. Then, identify clumps separately if their contours do not contain another local peaks (the boundary is taken at the minimum integrated intensity between the peaks), or else identify a clump using the contour of the highest peak as a clump boundary. (4) if a spectrum has multiple velocity components with a separation of more than 5 km s^{-1}, identify those components as being associated with different clumps.

In total, 18 clumps in the N48 region and 3 clumps in the N49 region are identified. The parameters of the identified clumps are listed in Table 3.1. Deconvolved clump sizes, $R_{\rm deconv}$, are defined as $[R^2_{\rm nodeconv} - (\theta_{\rm HPBW}/2)^2]^{0.5}$. $R_{\rm nodeconv}$ is the effective radius defined as $(A/\pi)^{0.5}$, where A is the observed total cloud surface area. $V_{\rm LSR}$ and the composite line width, $\Delta V_{\rm clump}$, are derived using a single Gaussian fit to the spectrum obtained by averaging all spectra within a single clump.

The virial mass is estimated as

$$M_{\rm vir}[{\rm M}_\odot] = 190\,\Delta V^2_{\rm clump}[{\rm km\,s^{-1}}]\,R\,[{\rm pc}], \tag{3.1.1}$$

which assumes that the clumps are spherical with density profiles of $\rho \propto r^{-1}$, where ρ is the number density and r is the distance from the cloud center (MacLaren et al. 1988).

The ^{12}CO(J=3–2) luminosity of the cloud $L_{\rm CO(J=3-2)}$ is the integrated flux scaled by the square of the distance,

$$L_{\rm CO}\ [{\rm K\ km\ s^{-1}\ pc^2}] = D^2 \left(\sum T_i\right) \delta v \delta x \delta y, \tag{3.1.2}$$

where T_i is the ^{12}CO(J=3–2) brightness temperature of an individual voxel, D is the distance to the LMC in parsecs (taken to be 5×10^4), δx and δy are the angular pixel dimensions in radians, and δv is the width of one channel in km s^{-1}.

Finally, ^{12}CO(J=3–2) luminosity mass of the clump $M_{\rm lum,3-2}$ is derived by using CO-to-H_2 conversion factor, $X_{\rm CO}$, of ^{12}CO(J=1–0). In order to convert $L_{\rm CO(J=3-2)}$ to the luminosity of ^{12}CO(J=1–0), a region-averaged ^{12}CO(J=3–2) to ^{12}CO(J=1–0) ratio $R_{3-2/1-0}$ is used. $M_{\rm lum,3-2}$ can be derived from $L_{\rm CO(J=3-2)}$ with these parameters,

$$M_{\rm lum,3-2}\,[{\rm M}_\odot] = 4.4\,\frac{X_{\rm CO}}{2\times10^{20}\,[{\rm cm^{-2}\,(K\,km\,s^{-1})^{-1}}]}\,R_{3-2/1-0}\,L_{\rm CO(J=3-2)}. \tag{3.1.3}$$

$X_{\rm CO}$ of the LMC is estimated in a lot of works (e.g., Fukui et al. 2008, Hughes et al. 2010, Leroy et al. 2011). Here the 7×10^{20} [cm^{-2} (K km s^{-1})$^{-1}$] of Fukui et al. (2008), which is one of the highest value, is adopted. Averaged $R_{3-2/1-0}$ is 1.0 and 0.8 for the N48 and N49 region, respectively.

Mean values (and minimum–maximum values) of the N48 and N49 clumps are $R_{\rm deconv} \sim 4.7$ pc (1.2–8.4 pc), $\Delta V_{\rm clump} \sim 4.3$ km s^{-1} (2.8–8.6 km s^{-1}), $M_{\rm vir} \sim 1.8 \times 10^4$ M$_\odot$ (0.17–9.3 $\times 10^4$ M$_\odot$), $L_{\rm CO(J=3-2)} \sim 1.2 \times 10^3$ K km s^{-1} pc^2 (0.25–3.5 $\times 10^3$ K km s^{-1} pc^2), and $M_{\rm lum,3-2} \sim 1.8 \times 10^4$ M$_\odot$ (0.39–5.4 $\times 10^4$ M$_\odot$). Comparisons of these values with the other molecular clumps in the LMC are shown in the following section.

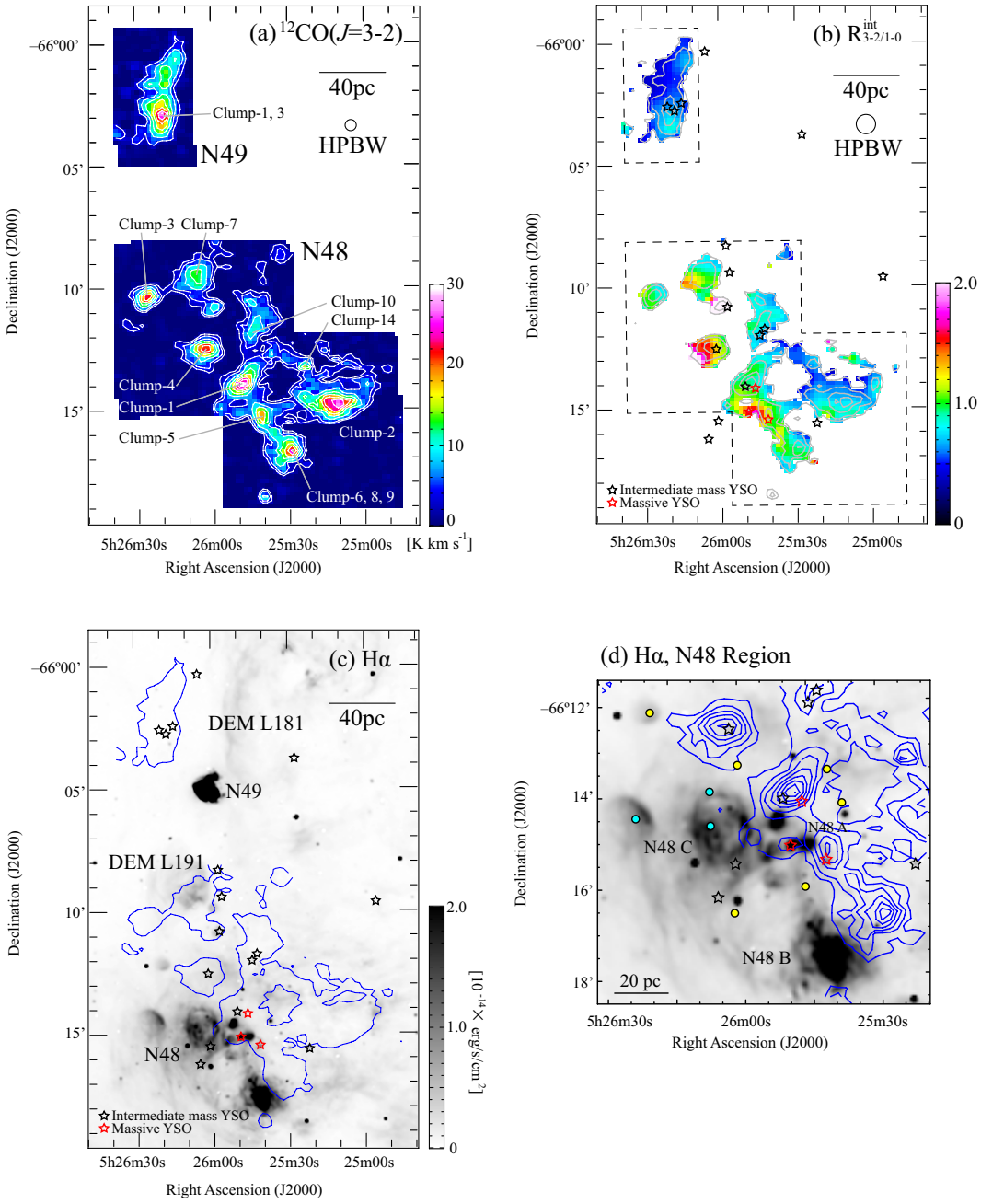

Figure 3.1: (a) ^{12}CO(J=3–2) integrated intensity maps of the N49 (north) and N48 (south) regions. In the N49 region, the integration range is 279.8 to 300.1 km s^{-1}, and the contour levels are 5σ, 10σ noise levels (3.4, 6.8 K km s^{-1}), and thereafter run in steps of 4.0 K km s^{-1}. In the N48 region, the integration range is 275.0 to 310.1 km s^{-1}, and the contour levels are 2.0, 4.0 K km s^{-1} and thereafter run in steps of 4.0 K km s^{-1}. The circle shows the ASTE effective beam size (27″). (b) Color map of the ^{12}CO(J=3–2) to ^{12}CO(J=1–0) (MAGMA Data Release 3, Wong et al. 2011) integrated intensity ratio of 45″ beam. Gray contours are the ^{12}CO(J=3–2) integrated intensity (started from 3.4 K km s^{-1} in steps of 4.0 K km s^{-1}). Black dashed lines are the observed area of the ASTE. Red and black stars in the first two maps are Spitzer YSO candidates (Whitney et al. 2008, Gruendl & Chu 2009). Red ones indicate massive YSOs (>10 M$_\odot$), and black ones indicate intermediate mass YSOs (3–10 M$_\odot$). (c) Grayscale image of Hα flux (Smith & MCELS Team 1999). Blue contours are the lowest contour of ^{12}CO(J=3–2) shown in (a). (d) Close-up view of the H II region N48. In addition to (c), blue and yellow circles of O-type and B-type stars (Will et al. 1996) are over-plotted.

Table 3.1: Parameters of the ^{12}CO(J =3–2) Clumps

	Peak Position		Physical Properties					
Clump	α(2000)	δ(2000)	$R_{\rm deconv}$	$V_{\rm LSR,clump}$	$\Delta V_{\rm clump}$	$M_{\rm vir}$	$L_{\rm CO(J=3-2)}$	$M_{\rm lum,3-2}$
ID	(h:m:s)	(d:′:″)	[pc]	[km s^{-1}]	[km s^{-1}]	[$10^4 M_\odot$]	[10^3 K km s^{-1}pc^2]	[$10^4 M_\odot$]
(1)	(2)	(3)	(4)	(5)	(6)	(7)	(8)	(9)
				N48				
1	5:25:47.9	−66:13:58.9	3.5	286.6	5.1	1.7	1.7	2.6
2	5:25:09.8	−66:14:48.9	6.6	292.4	8.6	9.3	3.5	5.4
3	5:26:25.8	−66:10:18.9	3.8	298.1	7.6	4.2	1.3	2.0
4	5:26:02.7	−66:12:28.9	4.4	287.5	3.9	1.3	1.7	2.6
5	5:25:41.3	−66:15:08.9	3.9	291.9	3.5	0.91	1.2	1.8
6	5:25:29.7	−66:16:48.9	2.9	285.1	4.0	0.88	1.0	1.5
7	5:26:06.0	−66:09:18.9	7.0	285.1	3.3	1.4	1.9	2.9
8	5:25:34.7	−66:16:08.9	5.4	291.7	3.7	1.4	1.4	2.2
9	5:25:34.7	−66:17:08.9	2.9	289.3	3.2	0.56	0.53	0.82
10	5:25:44.6	−66:11:48.9	5.8	280.6	5.6	3.5	1.0	1.5
11	5:24:58.3	−66:13:58.9	2.8	291.6	6.1	2.0	0.42	0.65
12	5:25:57.8	−66:14:58.9	1.2	288.7	2.7	0.17	0.28	0.43
13	5:25:24.7	−66:13:18.9	1.7	297.9	3.1	0.31	0.27	0.42
14	5:25:21.4	−66:13:48.9	3.5	297.5	3.1	0.64	0.44	0.68
15	5:25:46.2	−66:10:38.9	2.3	294.0	5.0	1.1	0.29	0.45
16	5:25:29.7	−66:12:58.9	5.4	298.0	3.7	1.4	0.64	0.99
17	5:25:59.4	−66:10:48.9	3.2	295.3	4.5	1.2	0.40	0.62
18	5:25:33.0	−66:08:48.9	3.5	298.1	2.8	0.52	0.25	0.39
				N49				
1	5:26:18.2	−66:02:53.0	6.6	285.2	4.2	2.2	3.0	3.7
2	5:26:16.6	−66:01:33.0	8.4	287.3	4.1	2.7	2.7	3.3
3	5:26:19.9	−66:02:53.0	3.9	292.2	2.6	0.5	0.58	0.71

Col.(1): ID numbers of ^{12}CO(J=3–2) clumps. Col.(2): ID numbers of ^{12}CO(J=3–2) local peaks corresponding to the clump. Col.(3)–(4): Positions of observed point of local peak. Col.(5)–(9): Observed physical properties of ^{12}CO(J=3–2) clumps. The deconvolution radius, $R_{\rm deconv}$, the velocity at the spectrum peak, $V_{\rm LSR,clump}$, the FWHM line width for the composite spectra within the clumps, $\Delta V_{\rm clump}$, the virial mass, $M_{\rm vir}$, the ^{12}CO(J=3–2) luminosity of the clump, $L_{\rm CO(J=3-2)}$, the ^{12}CO(J=3–2) luminosity mass of the clump, $M_{\rm lum,3-2}$ are shown.

Star Formation around the Clumps

Figure 3.1(b) shows the ^{12}CO(J=3–2) to ^{12}CO(J=1–0) integrated intensity ratio (hereafter $R_{\rm int}^{3-2/1-0}$). The ASTE data is smoothed to the same effective resolution as the Mopra maps (45″) before the ratio is taken. The ^{12}CO(J=1–0) data for the ratio map was the Mopra data (§2.2) in Fujii et al. (2014), but the observed area was limited around the major peak of the ^{12}CO(J=3–2). Here the ^{12}CO(J=1–0) data is taken from the latest version (Data Release 3) of the Magellanic Mopra Assessment (MAGMA, Wong et al. 2011), in order to see the distribution of the ratio for the entire clouds. $R_{\rm int}^{3-2/1-0}$ is apparently higher in the N48 region than in the N49. Mean values of $R_{\rm int}^{3-2/1-0}$ are 1.1 for the N48 region and 0.6 for the N49 region. Since $R_{\rm int}^{3-2/1-0}$ is getting high when the density and/or temperature of the cloud is high, this trend implies that these parameters are higher in the N48 region.

Figure 3.1(c) shows Hα (Smith & MCELS Team 1999) flux distribution with plots of Spitzer YSO candidates. H II regions and an SNR identified by Henize (1956) and Davies et al. (1976) are indicated in the figure. The Hα emission nebulae take a spatial offset from the clumps, and the clumps have no prominent Hα emission inside them. This indicates that prominent H II regions have not formed yet inside the clumps. Spitzer YSO candidates are distributed in and around the molecular clumps, suggesting that young star formation has occurred in both the N48 and N49 regions. It is notable that massive YSO candidates are only found in the N48 region. Figure 3.1(d) shows a zoomed-in view of 3.1(c) around the N48 Hα nebulae with additional plots of OB stars of NGC 1948 (Will et al. 1996). These OB stars are located away from the molecular clumps, which indicates that their parental clouds have already been dispersed by UV radiation or stellar winds. On the other hand the YSO candidates are preferentially located inside the clumps. The ages of these OB stars are estimated to be 5–10 Myr, and the age of the YSOs is estimated to be $\sim$ 1 Myr, assuming a YSO formation timescale of 0.2 Myr (Whitney et al. 2008). These features are well interpreted as a time sequence or an age gradient of the star formation activity in this area.

There is no clear relation between the distribution of $R_{\rm int}^{3-2/1-0}$ and those of Hα emission and YSO candidates. One exception is around the massive YSOs besides the H II region N48. So the direct heating by the massive stars are not so significant on high $R_{\rm int}^{3-2/1-0}$ in the entire N48 clumps.

^{12}CO(J=3–2) Distribution of the GMCs

Figure 3.2 shows the ASTE ^{12}CO(J=3–2) integrated intensity map of the N48 and N49 regions, and that of the GMCs observed in Minamidani et al. (2008). The GMCs that is observed in Minamidani et al. (2008) are 30 Doradus, N159, N171, N166, N206, N206D, and GMC225. These GMCs are located in the the “CO Arc” along the south-eastern optical edge (Fukui et al. 2008). The GMCs are sorted by three GMC types of Kawamura et al. (2009) according to their star formation activity, Type I: Starless GMCs with no associated O star capable of ionizing an H II region, which does not

exclude the possibility of associated young stars later than B type, Type II: GMCs with small H II regions, Type III: GMCs with H II regions and stellar clusters. It is clear from the figure that the star formation activity of the N48 and N49 regions is not so high as that of the cluster forming GMCs (Type III). The shape of the ^{12}CO(J=3–2) clouds of the N48 is characteristic. Each clouds are separately distributed without diffuse envelope components, and within a certain separation. This clumpy distribution is one of the most interesting feature in this area.

Total mass of the GMCs ranges between 0.4 and 10 $\times 10^6$ $M_\odot$ (N48+N49: $\sim$ 1.5 $\times 10^6$ $M_\odot$, 30 Dor: $\sim$ 0.7 $\times 10^6$ $M_\odot$, N159+N171: $\sim$ 10 $\times 10^6$ $M_\odot$, N166 $\sim$ 2 $\times 10^6$ $M_\odot$, N206 $\sim$ 0.9 $\times 10^6$ $M_\odot$, N206D $\sim$ 0.4 $\times 10^6$ $M_\odot$, GMC225: $\sim$ 1 $\times 10^6$ $M_\odot$; Fukui et al. 2008). Although the mass of the GMCs in the N48/N49 region is comparable to the other GMCs, the physical properties of the clumps in the N48/N49 region (size, linewidth, virial mass and luminosity) all tend to be smaller, and the number of identified clumps in the N48 region is notably large (18 for N48, 3 for N49, 5 for 30 Dor, 16 for N159 and N171, 5 for N166, 2 for N206, 1 for N206D, and 3 for GMC225). This suggests that the GMCs in the N48 and N49 regions consists of a concentration of compact clumps, which was also indicated by the quite clumpy distribution of the ^{12}CO(J=3–2) emission.

Comparisons of Physical Properties of the Clumps

Figure 3.3(a) is size-linewidth relation of the ^{12}CO(J=3–2) clumps. The clumps in the N48 and N49 regions, and the clumps of Minamidani et al. (2008) show prominently high line width above the classical fit line of the Milky Way clouds with similar radius (Solomon et al. 1987). Both the radius and the line width of the N48 and N49 clumps tend to be smaller than the Minamidani clumps. This also shows that the GMCs in the N48 and N49 regions consist of small clumps. Although the tracer and the definition of the clump are relatively concentrated on a dense part of the clumps, the underestimation of the clump radius is no more than factor 2, so this is not significant reason of the high line width. High line width trend in the size-linewidth relation is sometimes due to high column density of the sample clouds (Heyer et al. 2009), but the mean surface density of the clumps are comparable to the Milky Way clouds ($\sim 2 \times 10^{22}$ cm^{-2}). Thus, the clumps in the LMC have higher line width than the typical Milky Way clouds. The clumps in the N48 and N49 regions show smaller radius and line width than those of Minamidani et al. (2008). There is no clear difference on the size-linewidth trend between these clumps, and the slope of the distribution is that of the Milky Way clouds ($\Delta V \propto R^{0.5}$). The N48, N49 clumps show relatively smaller intercept than the Minamidani clumps, implying they have relatively smaller line width for their size.

Figure 3.3(b) shows $M_{\rm vir}$ versus $M_{\rm lum,3-2}$ of the ^{12}CO(J=3–2) clumps. The N48 and N49 clumps are not so massive than the Minamidani clumps. These clumps show similar relation of $M_{\rm vir}$ to $M_{\rm lum,3-2}$. Compared with the N48 and N49 clumps, Minamidani clumps show relatively high $M_{\rm vir}$ than the $M_{\rm lum,3-2}$. Median values of virial param-

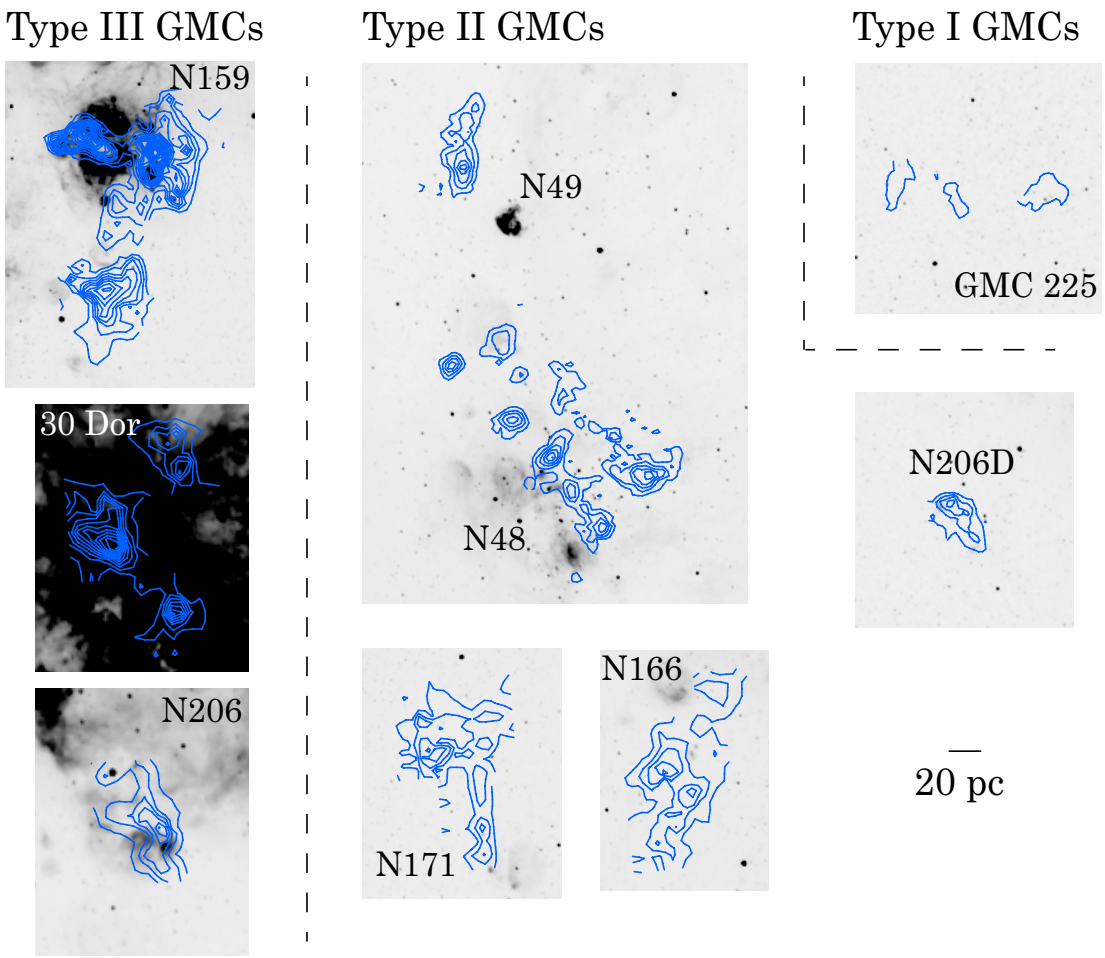

Figure 3.2: ASTE ^{12}CO(J=3–2) integrated intensity maps of the N48 and N49 regions, and those of the GMCs located around the CO Arc in the LMC observed in Minamidani et al. (2008) (30Dor, N159, N171, N166, N206, N206D, and GMC225). Contours are ^{12}CO(J=3–2) integrated intensity, and gray scale is Hα flux (Smith & MCELS Team 1999). The GMCs are sorted by three GMC types of Kawamura et al. (2009). The angular size scale is unified in all regions. The contours are started from 5 K km s^{-1} within a step of 5 K km s^{-1}. The beam size is 27″ for the N48 and N49 regions, and 22″ for the other GMCs (The difference is due to the difference of the observation method; On-the-fly for the N48 and N49, and the Position switching for the other GMCs Minamidani et al. 2008).

eter $\alpha \sim 1.12 \times M_{\rm vir}/M_{\rm lum,3-2}$ are 1.3 and 4.0 for N48, N49 clumps and Minamidani clumps, respectively. $\alpha > 1$ indicates that the clumps are relatively in the turbulent predominant state. Small virial parameter of the N48 and N49 clumps is mainly due to the smaller size-linewidth relation of the N48, N49 clumps. These imply that the N48, N49 clumps tend to be more gravitationally relaxed than the Minamidani clumps. Note that the $M_{\rm vir}$–$M_{\rm lum,3-2}$ relation is changed if another $X_{\rm CO}$ value is adopted for the $M_{\rm lum,3-2}$ estimation. For example, Leroy et al. 2011 gives smaller $X_{\rm CO}$ for the LMC ($\sim 3 \times 10^{20}$ cm^{-2} (K km s^{-1})$^{-1}$), and with this $X_{\rm CO}$, virial parameters are getting high by more than a factor of 2. Even in this case, it can be said that the clumps tend to be in the turbulent predominant state.

Separation between the Clumps in the N48 Region

The molecular clumps in the N48 region show characteristic clumpy distribution with a certain separation. Spatial separations of the peak of the clumps to the nearest neighbor are shown in Table 3.2 for the main 10 clumps (No. 1 to 10 of Table 3.1). Note that the clump 6, 8, and 9 are located in a similar spatial positions with different velocity peaks, so the three clumps are merged to 1 clump for the calculation of the separation. And also note that the projection effects, and the inclination of the LMC are not considered in the calculation. Typical separation without projection correction is $\sim$ 32 pc (without duplication of the nearest clump pare) but rather wide spread within 20 pc to 44 pc. Since the total elongation of the molecular clumps in the N48 region ($\sim$ 200 pc) is longer than the width of the high column density part of the H I ridge (equal to the depth of the ridge) of $\sim$ 100 pc, inclination between the clumps is not so significant, may be within $\sim$ 30 degree. Since the inclination of the LMC is also $\sim$ 35 degree from north to south, total underestimation of the clump separation is typically $\sim$ 20–30 %. Considering this underestimation, the typical separation of the clumps is roughly estimated to be $\sim$ 40 pc distributed within 30 pc to 50 pc.

3.1.2 Results of the ^{13}CO(J=3–2) Observation

The densities and the temperatures of the clumps can be derived from a large velocity gradient analysis (LVG analysis; Goldreich & Kwan 1974, Scoville & Solomon 1974) of the CO rotational transitions. In Fujii et al. (2014), three CO rotational transitions, ^{12}CO(J=3–2), ^{12}CO(J=1–0), and ^{13}CO(J=1–0) are used. However, the LVG analysis with these three transitions contains a significant amount of errors, sometimes more than one order of magnitude (see Minamidani et al. 2008, Fujii et al. 2014). On the hand, the LVG analysis with ^{13}CO(J=3–2) transition instead of ^{12}CO(J=1–0) gives more clear solutions (Minamidani et al. 2011), which may be due to the similarity of the critical densities of the three transitions. In this section, the results of the LVG analysis with newly obtained ^{13}CO(J=3–2) data is summarized.

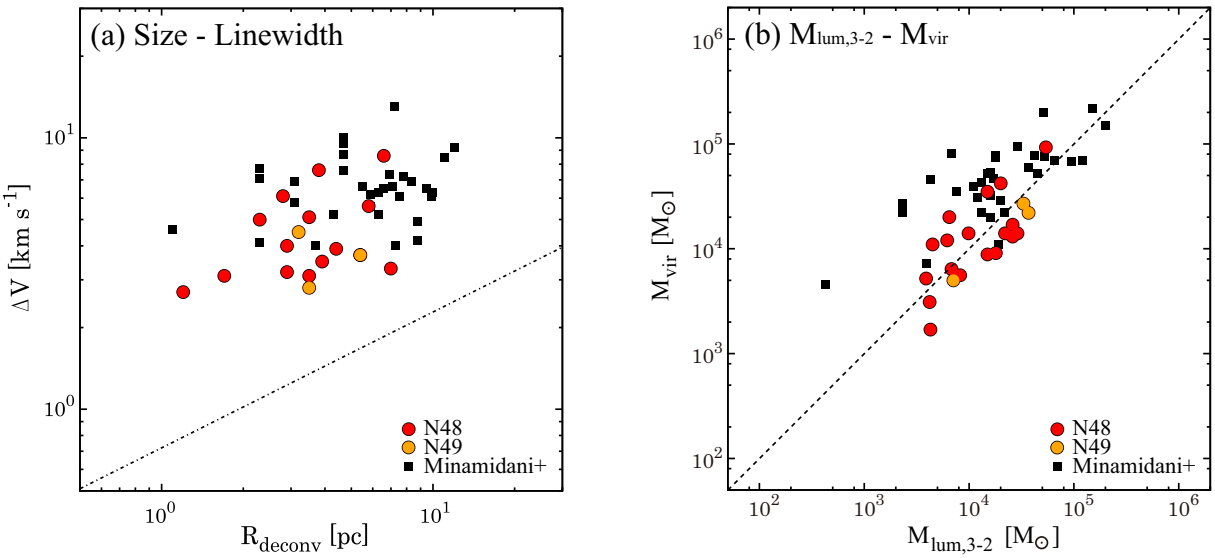

Figure 3.3: (a) Size–linewidth relation of the ^{12}CO(J=3–2) clumps. Red and orange filled circles indicate the clumps in the N48/N49 regions, and black filled boxes indicate the clumps of Minamidani et al. (2008). Dotted line is $\sigma_v = 0.72R^{0.5}$ that is the fit to the Milky Way clouds reported by Solomon et al. (1987). (b) Virial mass ($M_{\rm vir}$) to luminosity mass ($M_{\rm lum,3-2}$) relation of the ^{12}CO(J=3–2) clumps.

Table 3.2: Typical Separation of the ^{12}CO(J =3–2) Clumps

Clump ID (1)	Peak Position α(2000) (h:m:s) (2)	Peak Position δ(2000) (d:′:″) (3)	Neighbor ID (4)	Separation (pc) (5)
1	25:47.9	−66:13:58.9	5	20
2	25:09.8	−66:14:48.9	6,8,9	44
3	26:25.8	−66:10:18.9	7	43
4	26:02.7	−66:12:28.9	10	30
5	25:41.3	−66:15:08.9	1	20
6,8,9	25:33.0	−66:16:42.2	5	26
7	26:06.0	−66:09:18.9	3	43
10	25:44.6	−66:11:48.9	4	30

Col.(1): ID numbers of ^{12}CO(J=3–2) clumps. Col.(2)–(3): Positions of observed point of local peak. Col.(4)–(5): ID number of the nearest clump and the separation between them.

LVG analysis

The LVG radiative transfer code simulates a radiation from a spherically symmetric cloud of an uniform density and temperature with a spherically symmetric velocity gradient proportional to the radius. It employs a Castor's escape probability formalism (Castor 1970). The LVG model requires three independent parameters to computer emission line intensities: the kinetic temperature, $T_{\rm kin}$, the density of molecular hydrogen, $n(\rm H_2)$, and $X(\rm CO)/(dv/dr)$. $X(\rm CO)/(dv/dr)$ is the abundance ratio of CO to $\rm H_2$ divided by the velocity gradient in the cloud.

The LVG model calculations is performed over a grid of temperatures in the range $T_{\rm kin}$ = 5–200 K and densities in the range $n(\rm H_2)$ = 10–10^6 cm^{-3}, with grid spacings of $10^{0.02}$ K and $10^{0.125}$ cm^{-3}, respectively. This produced sets of line intensity ratios, $R^{13}_{3-2/1-0}$ and $R^{12/13}_{3-2}$. The model includes the lowest 40 rotational levels of the ground vibrational state and uses the Einstein A and $\rm H_2$ impact rate coefficients of Schöier et al. (2005). The higher energy levels are not included, which would require including populations in the lower vibrationally excited states. This imposes a limit of $T_{\rm kin} \sim 200$ K in the present study.

To solve for the temperatures and densities that best reproduce the observed line intensity ratio, a chi-squared is calculated as

$$\chi^2 = \sum_{i=1}^{N-1} \sum_{j=i+1}^{N} \frac{[R_{\rm obs}(i,j) - R_{\rm LVG}(i,j)]^2}{\sigma(i,j)} \tag{3.1.4}$$

where N is the number of transitions of the observed molecule (in this case $N = 3$), i and j refer to different molecular transitions, $R_{\rm obs}(i,j)$ is the observed line intensity ratio from transition i to transition j, and $R_{\rm LVG}(i,j)$ is the ratio between transitions i and j, estimated from the LVG calculations. The standard deviation, $\sigma(i,j)$, for $R_{\rm obs}(i,j)$ is estimated from the noise level of the observations and the calibration uncertainties.

Results of the LVG Analysis

The LVG analysis was applied to the clumps which are covered by the ASTE ^{13}CO(J=3–2) observations. The selected clumps are N48–1, 2, 3, 4, 6, 7, and N49–1 (Hereafter N4849 clumps). The method and the parameters of the LVG analysis is the same as those described in Minamidani et al. (2011). Observational values of $R^{13}_{3-2/1-0}$ and $R^{12/13}_{3-2}$ were obtained from the ratios of the peak main beam temperature values, where the ^{12}CO(J=3–2) and ^{13}CO(J=3–2) data has been smoothed to the resolution of the Mopra data (45″). Uniform fractional abundance ratios [^{12}CO/$\rm H_2$] of 1.6 × 10^5, [^{12}CO/^{13}CO] of 50 were adopted ((Mizuno et al. 2010, Minamidani et al. 2011)). The mean velocity gradient is estimated be $dv/dr = \Delta V_{\rm clump}/2R_{\rm deconv}$. The uncertainties of the two ratios are estimated to be 17%–34% and 16%–33%, respectively, calculated by combining the calibration errors and the formal errors on the gaussian model fits. The values of the parameters used in the LVG analysis are summarized in Table 3.3.

The lowest values of χ^2 are regarded as the best solution for the temperatures and the densities of the clumps. Error bars are defied as $\chi^2 < 3.84$, which corresponds to the 5% confidence level of the χ^2 distribution with one degree of freedom. Contour plots of the LVG analysis on the $n(H_2)$–T_{kin} plane are summarized in Figure 3.4 and the derived values are summarized in Table 3.4. The results of the clumps in Minamidani et al. (2011) is also listed in the table (30Dor–1, 3, 4, N159–1, 2, 4, N206D–1, GMC225–1, see also table 2 of Minamidani et al. 2011: Hereafter M11 clumps).

The output of the LVG calculations are shown as $n(H_2)$–T_{kin} plots in Figure 3.5(a)(b). The N4849 clumps are typically warm (greater than 50 K), with moderate density (1–3×10^3 cm^{-3}). $n(H_2)$ and T_{kin} of the N48 clumps tend to be higher than those of the N49 clumps. In figure 3.5(b), the M11 clumps are colored according to their parent GMC types defined in Kawamura et al. (2009) (see also §1.1.4) The clumps of the massive cluster forming GMCs (Type III: 30 Dor, N159) tend to be warm and dense, and the clumps of the starless GMCs (Type I: GMC225) tend to be colder and less dense. This tendency suggests an evolutionary sequence in terms of increasing density leading to star formation and increased star formation activity leading to intense FUV photons that heat the clouds, as discussed in Minamidani et al. (2008, 2011). The $n(H_2)$–T_{kin} plots of the N4849 clumps are distributed between those of the M11 clumps hosted by Type I/II and Type III GMCs. This implies that the N4849 clumps may be just at the stage of evolving to the cluster forming clumps. This is consistent with the suggestion of the GMCs in the N48/N49 region are in the early stage of a cluster-forming cloud (Mizuno et al. 2001).

These indications strengthen the previous findings reported in Fujii et al. (2014), since the accuracy of the estimated value is significantly improved. It is notable that the N4849 clumps are clearly not as dense as the clumps in the Type III GMCs (30 Dor and N159). So the N4849 clumps are surely in the evolving phase.

3.1.3 Interacting Area of the SGSs

The H I distribution suggests that the N49 clumps are associated with only one SGS, LMC5, whereas the N48 clumps are located right in the boundary of the two SGSs where the column density of H I is getting high. Comparisons of these two regions therefore provides insight into the differences between the physical effects of a single shell and the interaction of two SGSs on the molecular clump properties and the star formation activities. As seen in the previous section, star formation activity is more active at the N48 region, which is also clearly seen in the Figure 3.7. And the N48 clumps are denser and warmer than the N49 clumps, indicating that the N48 clumps are more evolved. These differences of the molecular clump properties and the star formation evolutionary stage suggest that the formation of dense molecular clumps and massive stars is enhanced in the region of high-density gas swept up by the two SGSs, and this SGS interaction has worked more efficiently to create stars from the ISM than the effect of a single SGS. This is one of the most important results that is reported in Fujii et al. (2014).

Table 3.3: Parameters of the LVG Analysis

Region	Clump	$T_{\rm mb}(K)$			Line Ratio		dv/dr
Name	No.	^{13}CO(J=3–2)	^{13}CO(J=1–0)	^{12}CO(J=3–2)	$R^{13}_{3-2/1-0}$	$R^{12/13}_{3-2}$	(km s^{-1})
(1)	(2)	(3)	(4)	(5)	(6)	(7)	(8)
N48	1	0.35±0.06	0.31±0.04	3.3±0.2	1.1±0.20	9.4±1.7	0.7
	2	0.12±0.02	0.19±0.03	2.5±0.2	0.63±0.15	21±4.0	0.7
	3	0.10±0.02	0.11±0.03	1.7±0.2	0.91±0.31	17±4.0	1.0
	4	0.45±0.07	0.30±0.04	3.6±0.3	1.5±0.30	8.0±1.4	0.4
	6	0.19±0.03	0.14±0.04	2.3±0.2	1.4±0.40	12±2.0	0.7
	7	0.29±0.04	0.21±0.04	2.7±0.2	1.4±0.30	9.3±1.5	0.2
N49	1	0.30±0.04	0.56±0.06	3.6±1.0	0.54±0.09	12±4.0	0.3

Col.(1)–(2): Names of the region and ID numbers of the ^{12}CO(J=3–2) clumps that are used for the LVG analysis. Col.(3)–(5): Peak main beam temperatures of ^{13}CO(J=3–2), ^{13}CO(J=1–0) , ^{12}CO(J=3–2) lines. Col.(6)–(7): Line intensity ratios that we have used in LVG analysis. Ratio of ^{13}CO(J=3–2) and ^{13}CO(J=1–0), $R^{13}_{3-2/1-0}$, and ratio of ^{12}CO(J=3–2) and ^{13}CO(J=3–2), $R^{12/13}_{3-2}$, are shown. Col.(8): Averaged velocity gradients of the clumps.

Table 3.4: Results of the LVG Analysis

Region	Clump	$n(\rm H_2)$ (10^3 cm^{-3})		$T_{\rm kin}$ (K)		Min. χ^2
Name	No.	$\chi^2 < 3.84$	at Min. χ^2	$\chi^2 < 3.84$	at Min. χ^2	
(1)	(2)	(3)	(4)	(5)	(6)	(7)
N48	1	1.8–3.4	2.4	38–87	63	0.021
	2	0.55–1.7	1.0	35–200	87	0.18
	3	0.91–2.9	1.8	24–200	69	0.027
	4	1.6–3.2	2.4	56–181	91	0.25
	6	1.4–2.9	1.8	46–200	110	0.069
	7	0.96–1.9	1.3	86–200	191	0.12
N49	1	0.68–2.5	1.3	23–143	50	0.16

Col.(1)–(2): Names of the regions and ID numbers of the clumps. Col.(3)–(6): Derived number density, $n(\rm H_2)$ cm^{-3}, and kinetic temperature, $T_{\rm kin}$, of the clumps are shown. The ranges of the values for that χ^2 is less than 3.84, and the values at the point where χ^2 is minimum are shown. Col.(7): Value of minimum χ^2 is shown.

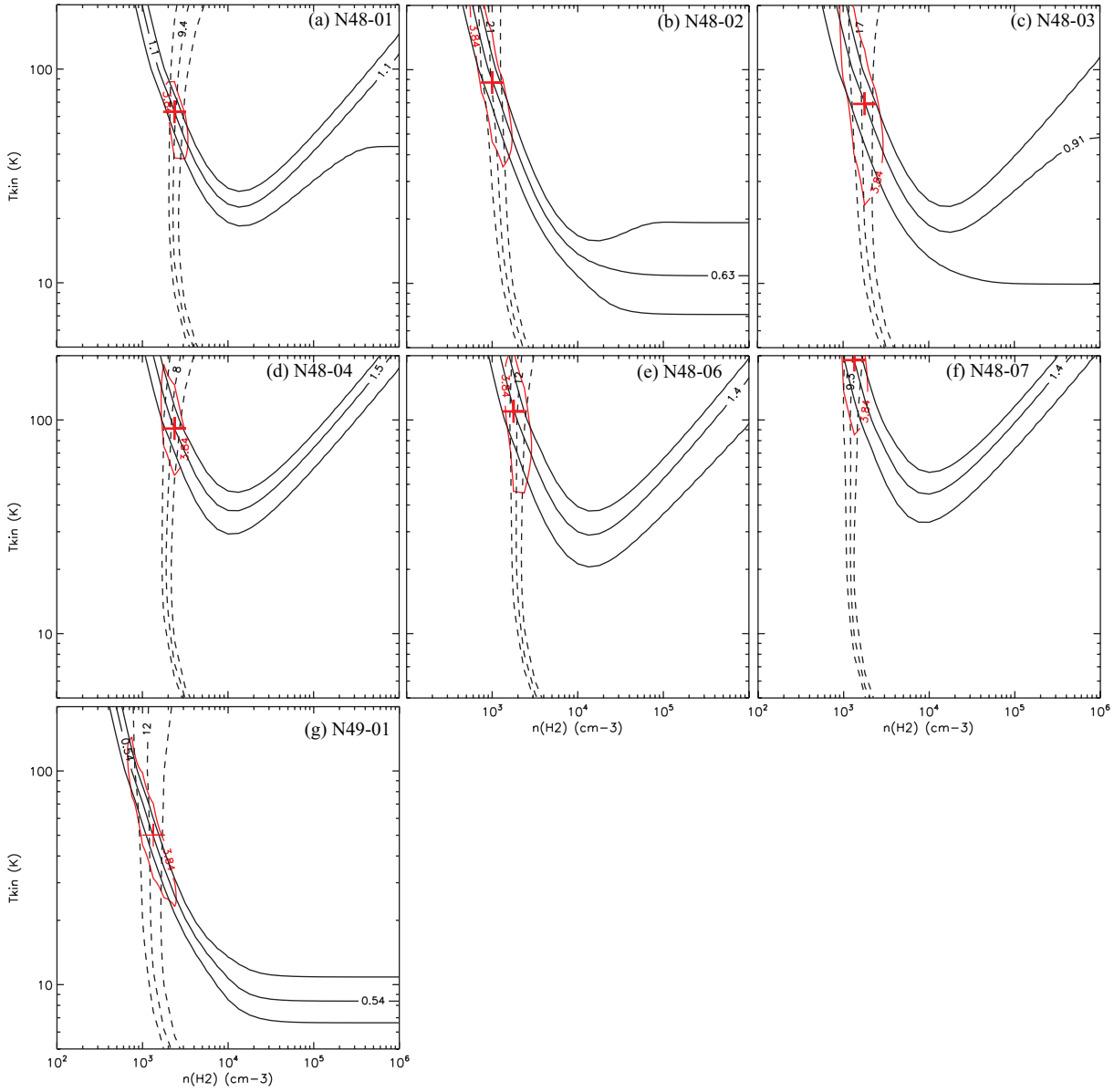

Figure 3.4: The results of the LVG analysis for the N48 and N49 regions. Crosses denote the points of lowest chi-square χ^2. Red contours indicate $\chi^2 = 3.84$, which corresponds to the 5% confidence level of the χ^2 distribution with one degree of freedom. Black lines show the intensity ratios: $R^{13}_{3-2/1-0}$ (solid lines), $R^{12/13}_{3-2}$ (dashed lines). Each consists of the observed intensity ratios (center) and uncertainty envelopes (outer two lines) that are estimated to be 17%–34% for $R^{13}_{3-2/1-0}$ and 16%–33% for $R^{12/13}_{3-2}$.

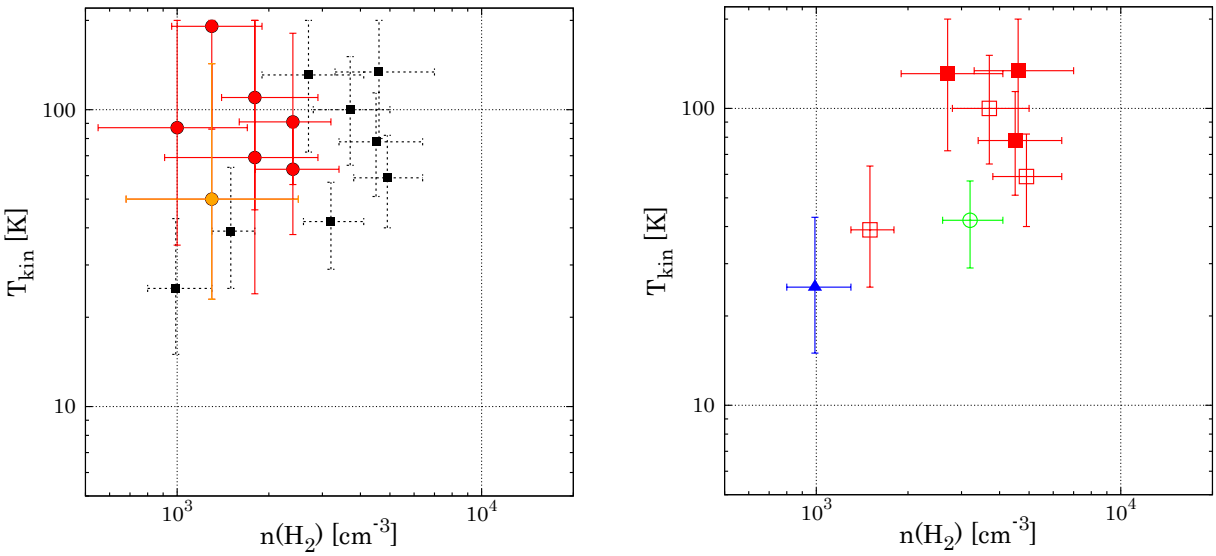

Figure 3.5: Plots of the molecular hydrogen density ($n(H_2)$) and the kinetic temperature (T_{kin}) of the clumps derived via the LVG analysis. (left) Red and orange filled circles indicate the clumps in the N48/N49 regions (N4849 clumps), and black filled boxes indicate the clumps of Minamidani et al. (2011) (M11 clumps). Error bars (solid line for N4849 clumps and dotted line for M0811 clumps) are the range of values for which χ^2 is less than 3.84. (right) A $n(H_2)T_{kin}$ plot of the M11 clumps. Different symbols indicate the various regions in which the clumps are located (filled square: 30 Dor, open square: N159, open circle: N206D, triangle: GMC225). Each mark and error bar is colored according to the types of their parental GMCs; Type I in blue (GMC 225), Type II in green (N206D), Type III in red (30 Dor, N159).

3.2 Results of the H I Observation

3.2.1 High-resolution H I Map

Figure 3.6 is integrated intensity maps of an archival ATCA+Parkes H I data (Kim et al. (2003); Kim data), and the high-resolution new H I data (new data). Angular resolutions are 60″, and 24.7″ × 20.5″, respectively. These resolutions correspond to the spatial resolution of 15 pc and 6 × 5 pc, respectively. This spacial resolution is usually high for the H I data around the star forming region in the external galaxies. The spatial resolution of the new data is slightly higher than the FWHM beam size of the ASTE ^{12}CO(J=3–2) data ($\sim$ 27″, $\sim$ 8 pc). Roughly, the H I intensity distribution of two images are similar, so the new observation seems to successfully reproduce the previous imaging. In more detailed scale, the new data resolved the finer structure of the H I than those from the Kim data. Although the H I distribution of the central part of the ridge is still unclear, the structure of diffuse component around the ridge is more resolved than the Kim data.

The Figure 3.7 shows comparison plot of the new data with tracers of star formation activities, i.e., Hα and 8 μm emissions. Hα data is from the Magellanic Cloud Emission-Line Survey (MCELS; (Smith & MCELS Team 1999)), and 8 μm data is taken from the Spitzer Legacy Program "SAGE" (Meixner et al. 2006) with the Infrared Array Camera (IRAC; Rieke et al. 2004). Names of H II regions and supernova remnants identified by Henize (1956) and Davies et al. (1976) are indicated in the figure. The difference of the resolution is quite clear around the hole of the SNR N49 ($\sim$ 5h 26m:−66° 05′) and the H II region N48 ($\sim$ 5h 26m:−66° 25′). The other Hα emitters not show clear correspondance with the H I integrated intensity.

H I intensity is sharply depressed toward the LMC 4 (east) but rather elongated toward the LMC 5 (west). This may be related to the diffuse filament of the Hα, that is smoothly distributed along the ridge toward the rim of the LMC 4, but is a bit complicatedly distributed toward the LMC 5 rim. To understand why such structures are formed is not simple, so no discussion about it will be done here. One implication from these features is that some kind of external ionization mechanisms are at work in both sides of the ridge, so there seem to be still radiative pressures from the cavities of both shells.

Two clear absorption features of compact background continuum sources are newly detected in the north part of the image ([5h 26m 25.9s; −65° 56′ 19.0″] and [5h 26m 32.9s; −65° 49′ 7.9″]). These objects can not be seen in the Hα map, but 1.4 GHz continuum emission is detected with total flux $\sim$ 0.2 Jy. These objects are identified as radio continuum sources as N49 C and N49 D in Filipovic et al. (1998), but there is no information about what kind of sources they are. The H I absorption toward these sources has not been reported before except for Marx-Zimmer et al. (2000) just referred that one H I absorption feature was detected around this area, but there is no detailed publication about it until now. Their angular sizes are rather greater than beam size of the new data ($\sim$ 40″ × 60″ and $\sim$ 40″ × 50″, respectively), so they have some angular

extent about $\sim 30''$ to $50''$, considering $\sim 25''$ beam of the new data.

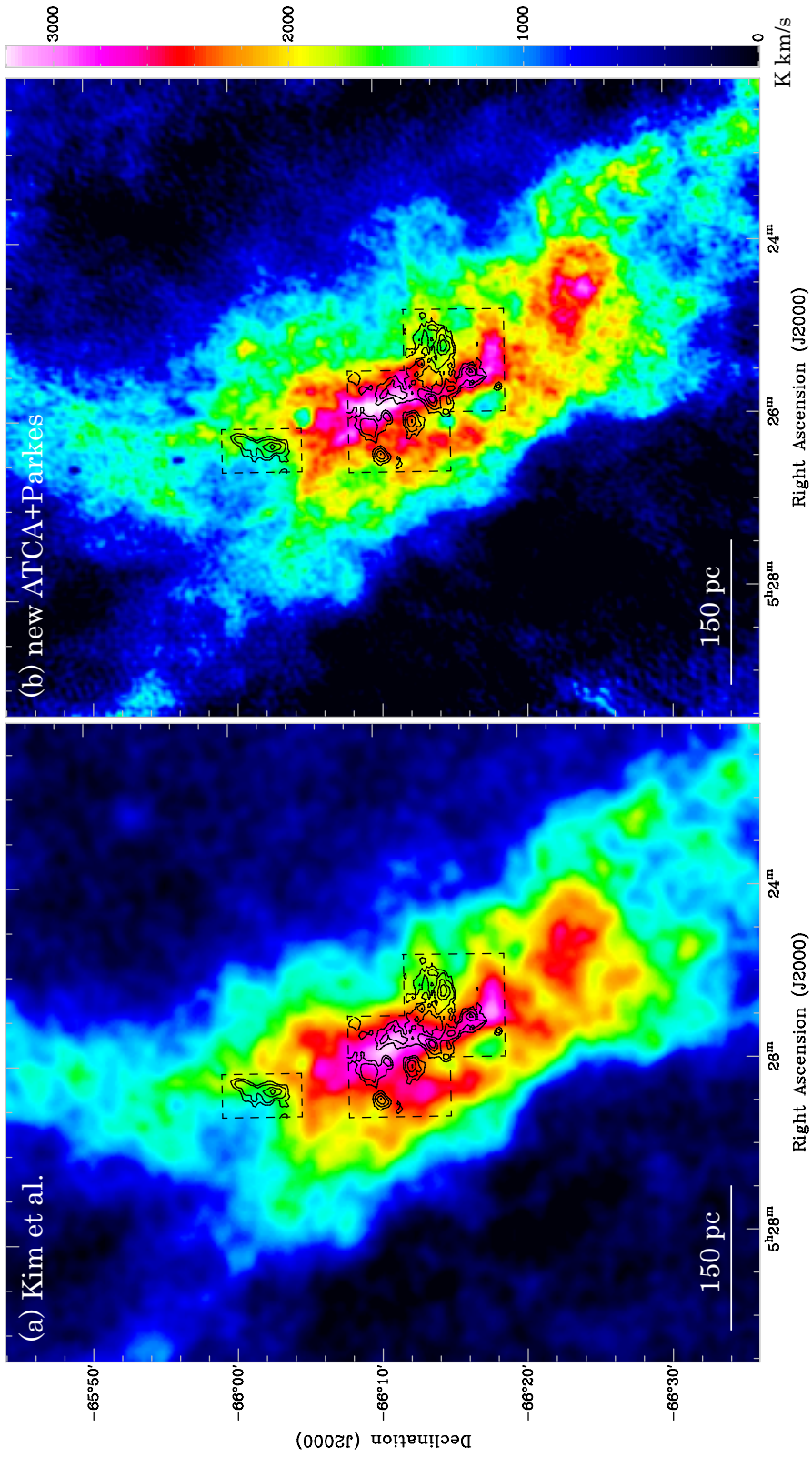

Figure 3.6: (a) A color map of the H I integrated intensity of Kim et al. (2003) (Kim data) with 60″ beam. Black contours are the ASTE ^{12}CO(J=3–2) integrated intensity, and black dotted boxes are the ASTE observed area. (b) A color map of the H I integrated intensity of the new ATCA+Parkes data (new data) with 24.7″ × 20.5″ beam. Contours and boxes are the same as (a).

3.2.2 High-resolution H I Spectra and Channels

Typical line spectra at the molecular clump peaks of the N48 and the N49, and at the peak position of H I integrated intensity are shown in Figure 3.8. The H I spectra of the Kim data and the new data are roughly similar shape, so peak temperatures of the spectra do not change so much even the resolution is different. This indicates that the H I is optically thick around the spectra peaks at these points, and the structure is still smoothly distributed even in the high resolution image. On the other hand, at the peak position of the H I, the spectrum of the new data shows clearer double component than the Kim data. The spatial distribution of each H I component is more resolved with higher angular resolution in such positions. The CO spectra distribute roughly around the peak velocity positions of the H I spectra, but the spectral shapes of the CO are different from those of the H I. This may be due to the complex composition of the H I components, and the deformation of the H I spectra with the optically thick condition.

Figures 3.9 to 3.12 are channel maps of the new data. The H I is distributed from 260 km s^{-1} to 330 km s^{-1}. Bright H I ($>$ 50 K, roughly the half of the brightest intensity) can be seen in the 276 km s^{-1} to 310 km s^{-1} channels. Each channel shows complicated structures of the H I, and their spatial distribution is different each other. This indicates that the H I ridge consists of a lot of sub-components. Most of the sub-components look quite filamentary, so the H I ridge possibly consists of the composition of H I filaments. Detailed analysis of this filamentary H I feature will be done in §4.2.

The CO emission is detected in the channels from 276 km s^{-1} to 305 km s^{-1}. The H I is quite luminous in these CO detected channels . In the 286 km s^{-1} and 291 km s^{-1} channels, where the CO is the most luminous, dense molecular clouds are distributed along the filamentary H I feature. It can be interpreted as the main part of the molecular clouds are formed in the luminous filamentary H I structures. This is one of the most important suggestion of this high-resolution H I observation. Note that there are strong H I regions without CO clouds. In such regions, actual density of the H I medium might not be high enough to form molecular clouds.

In the velocity range from 340 km s^{-1} to 370 km s^{-1}, high-velocity H I component are found from the north part of the N48 region to the west part of the N49 region. The velocity difference from the main component is roughly 60 km s^{-1}. In the western part of the N49, there are supernova remnants N49 and N49B. It is possible that such high-velocity components might be accelerated by these SNRs. Further analysis is required, but it is not related to the main goal of this thesis so no detailed discussion will be mentioned here.

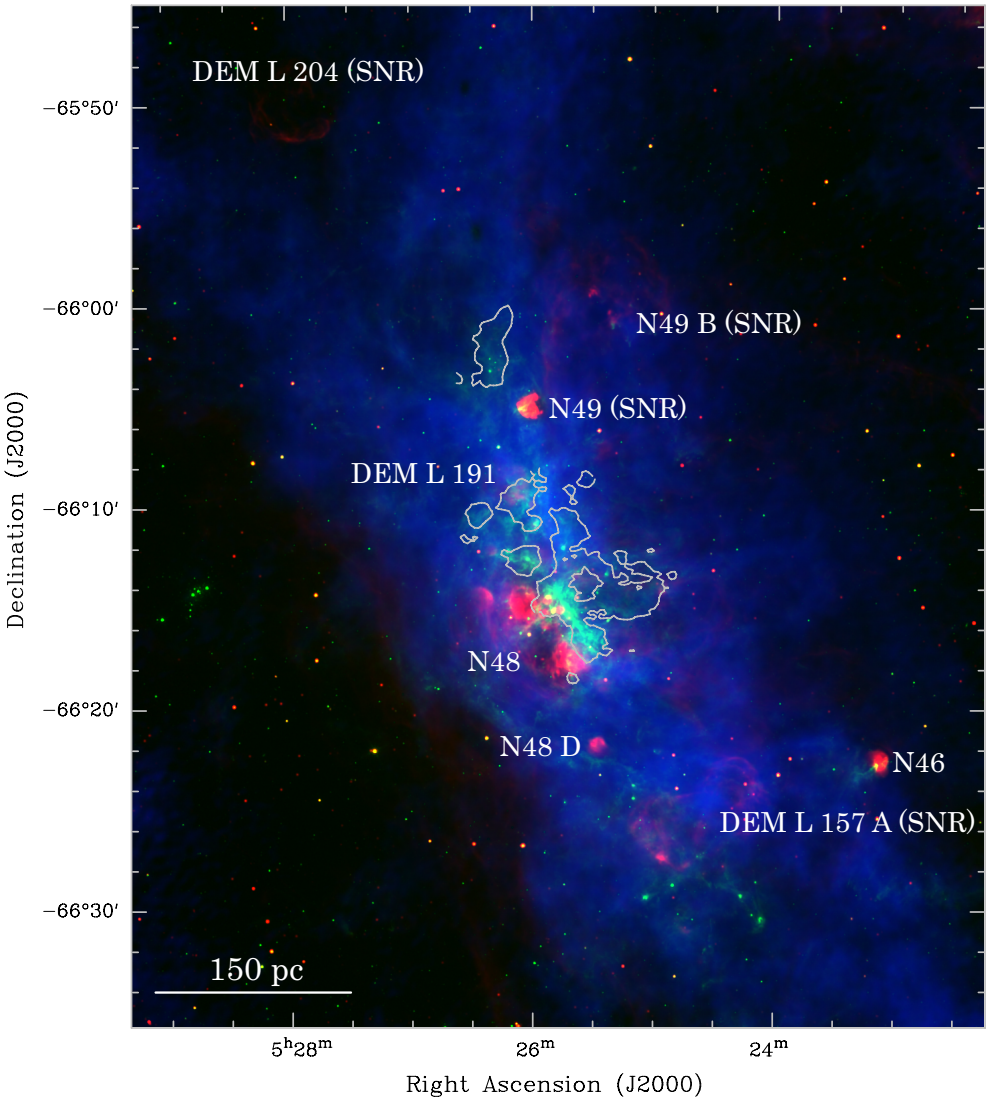

Figure 3.7: 3 color image of the H I ridge. Red is Hα flux (Smith & MCELS Team 1999) , green is Spitzer 8.0 μm (Meixner et al. 2006) , and blue is the H I of the new data.

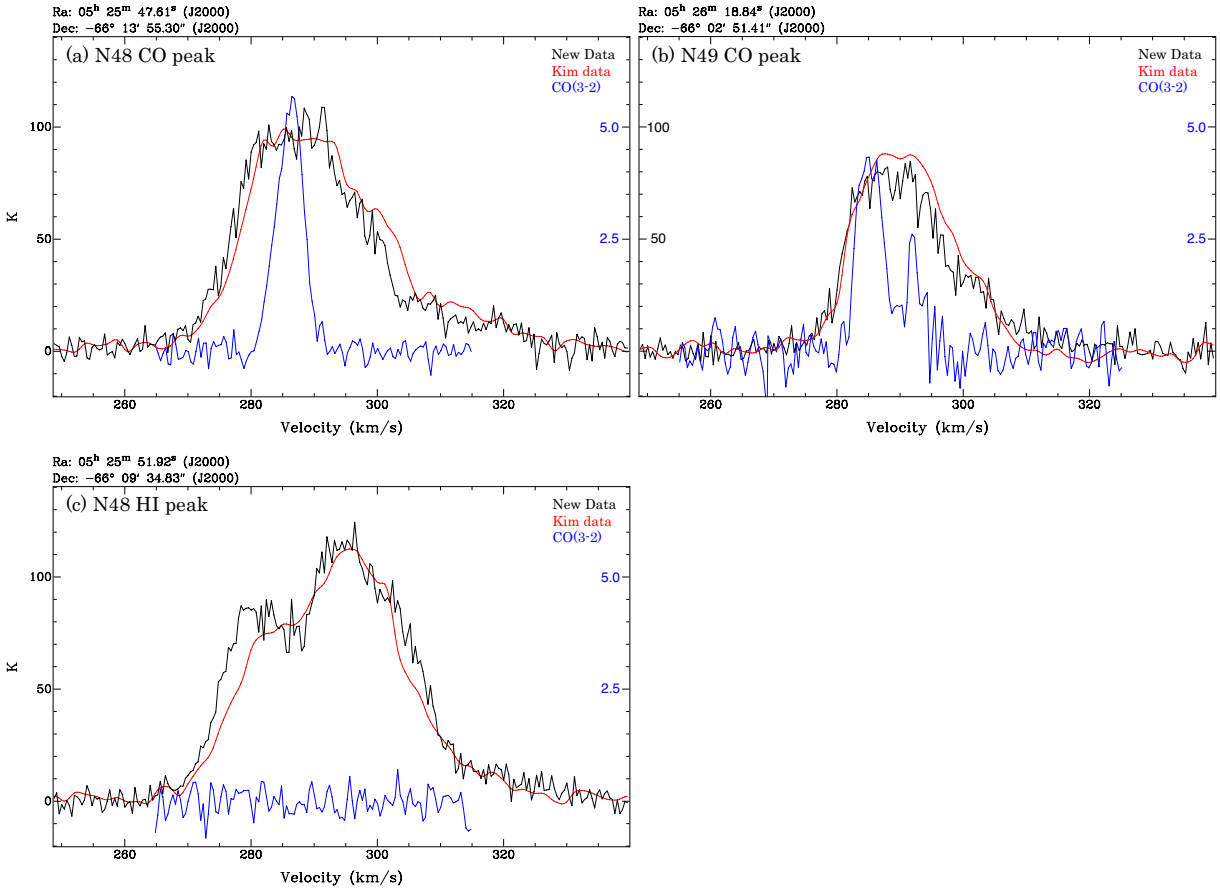

Figure 3.8: Examples of the spectrum of the H I of the new data (black), together with the Kim data (red), and the ASTE ^{12}CO(J=3–2) (blue). (a) Spectra at the strongest ^{12}CO(J=3–2) peak position in the N48 region (5h 25m 47.6s, -66° 13′ 55.3″). (b) Spectra at the ^{12}CO(J=3–2) peak position in the N49 region (5h 26m 18.8s, -66° 02′ 51.5″). (c) Spectra at the most luminous position in the ridge (in the N48 region, 5h 25m 51.9s, -66° 09′ 34.8″).

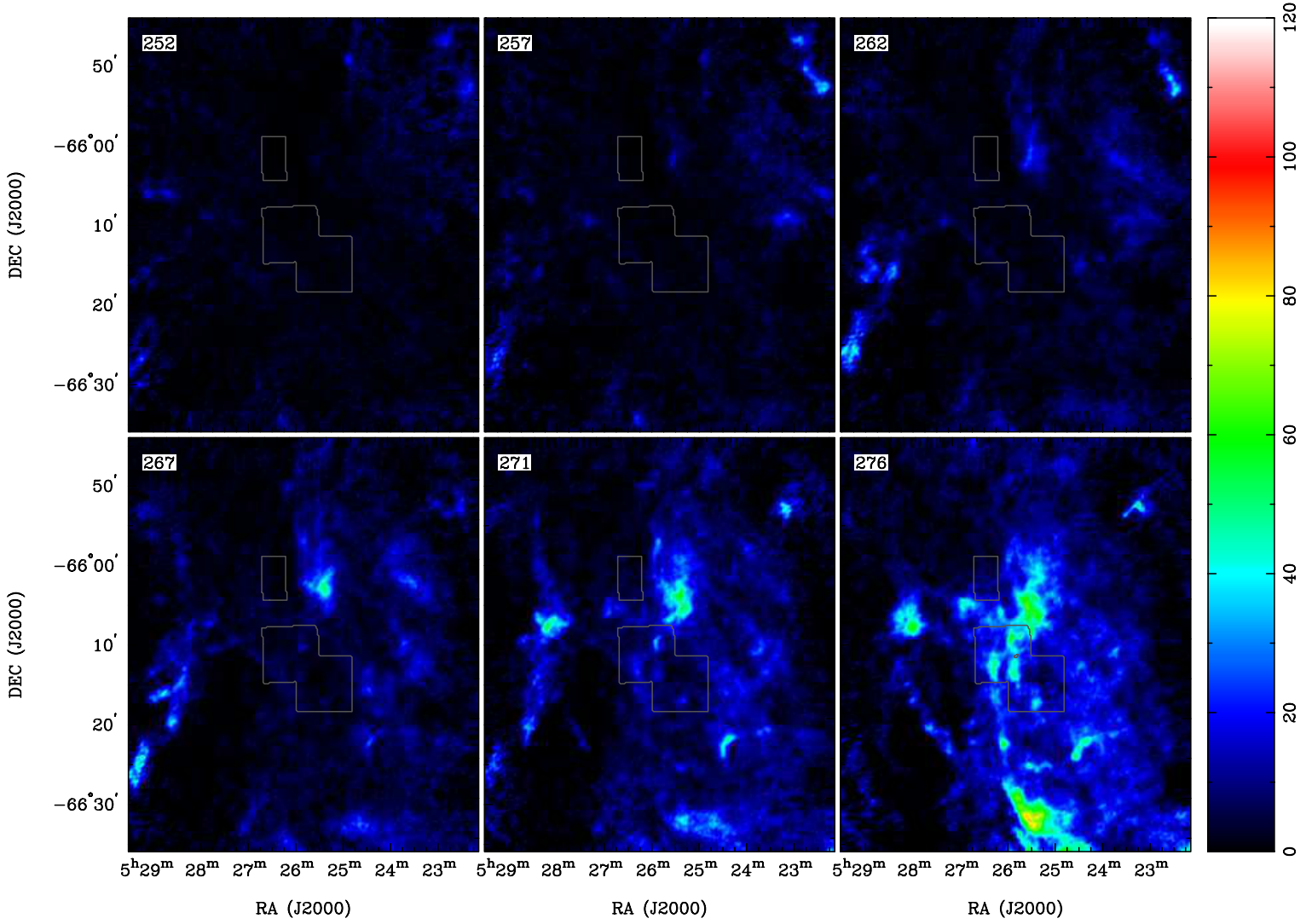

Figure 3.9: Velocity channel maps of the H I brightness temperature of the new data (color) and ^{12}CO(J=3-2) brightness temperature (black contour) of the H I ridge (covered area is the same as Figure 3.6), averaged in the velocity intervals of 5.0 km s^{-1}. The central velocity is shown in the upper left of each panel. Black boxes indicated in the all channels are the observed area of the ASTE.

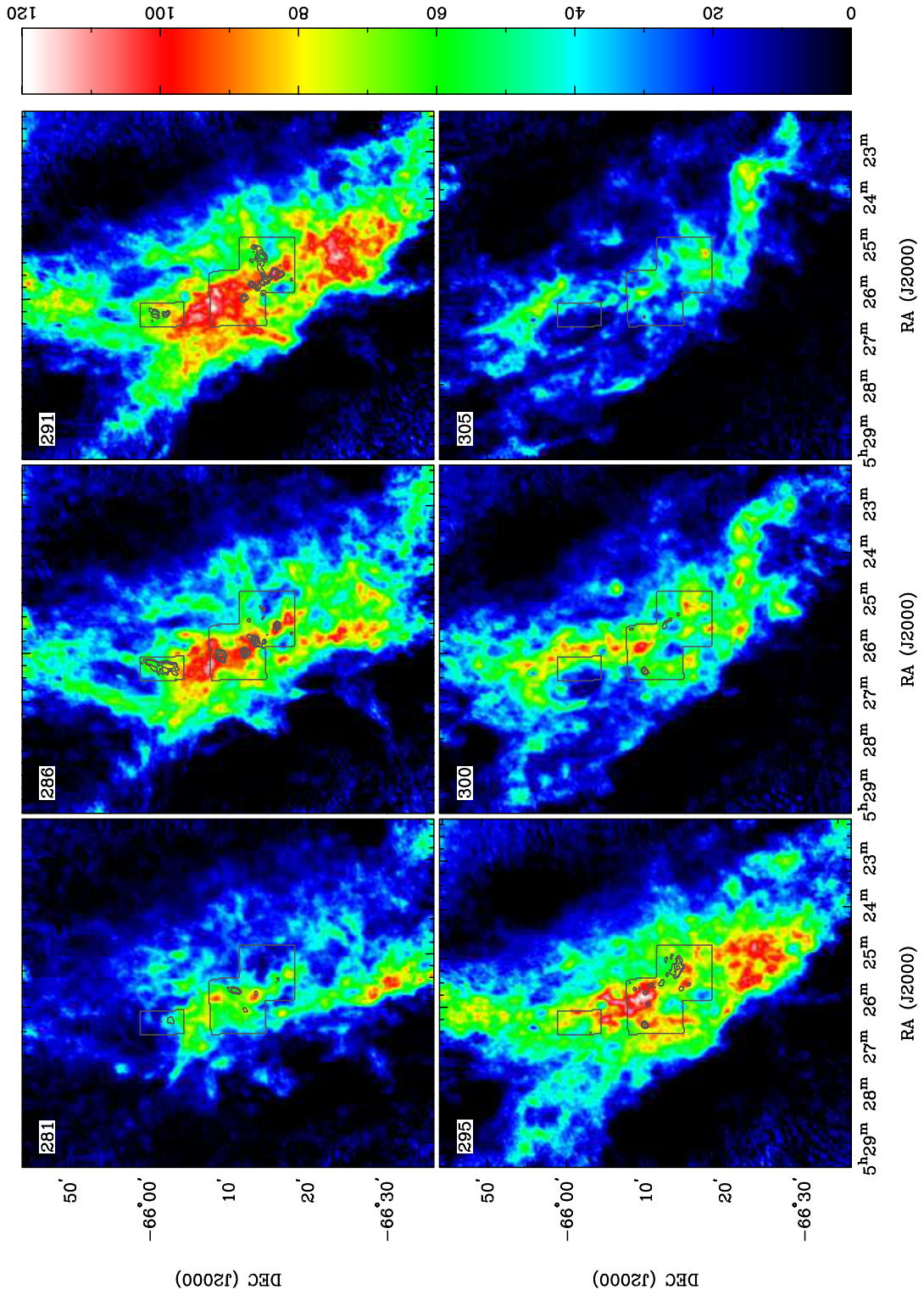

Figure 3.10: (Continued channel maps)

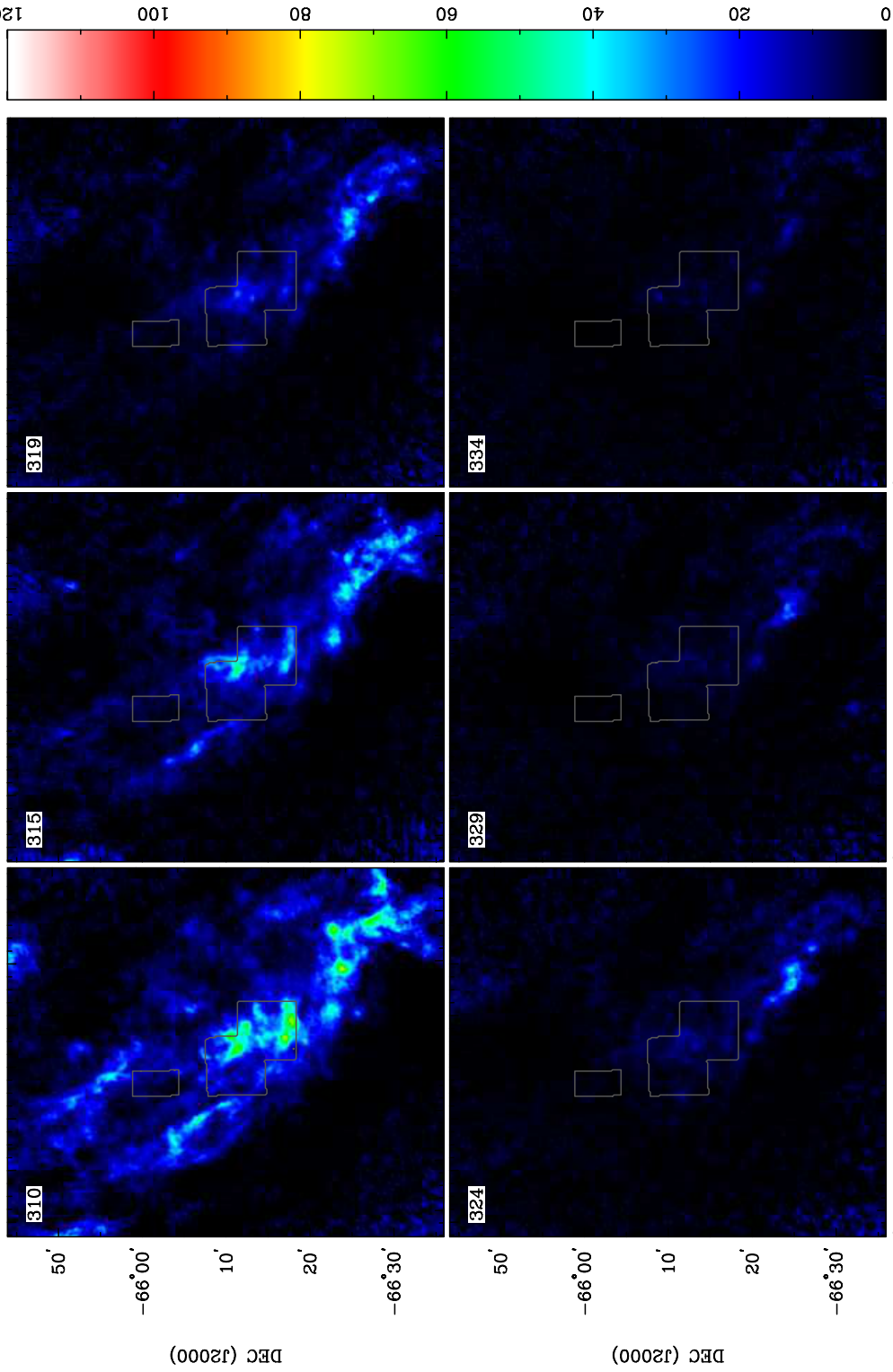

Figure 3.11: (Continued channel maps)

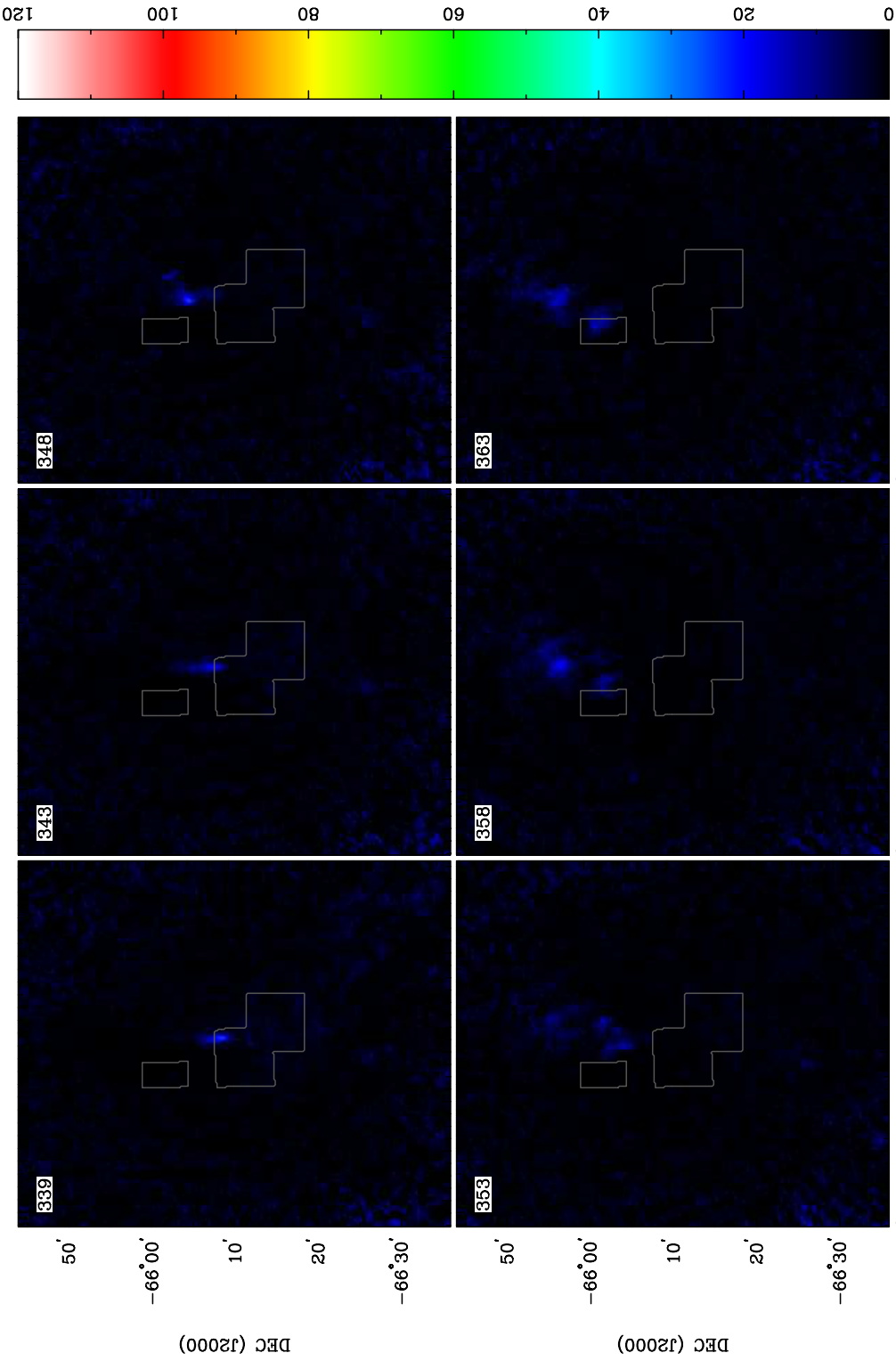

Figure 3.12: (Continued channel maps)

Chapter 4

Analysis

4.1 Optically Thick H I

Before discussing the detailed structure and the kinematics of the ridge, there are several questions. What is the mass of hidden H I which cannot be traced by the 21 cm line emission? How extent the optically thick H I component is? The true column density of the H I should be estimated.

Here the method that is constructed by Fukui et al. (2014) and Fukui et al. (2015c) is adopted. Assuming that the gas and the dust are well mixed with uniform properties, opacity corrected H I column density can be derived from the opacity of the dust. The detail of the method is summarized before (§1.1.2, and see also the referenced papers). This method might be the most convenient and reasonable way to estimate the actual column density of the H I ridge, because no complicated fitting process is required.

Archival data sets of optical depth at 353 GHz (τ_{353}), dust temperature ($T_{\rm d}$), smoothed-beam H I, and Hα flux are used for the analysis. The τ_{353} and $T_{\rm d}$ were obtained by fitting 353, 545, and 857 GHz data of the first 15 months observed by the Planck satellite and 100 micron data of the IRAS satellite. Angular resolutions of the both data sets are 5 arcminutes with pixel size of 2 arcmin. For the details, see the Planck Legacy Archive (PLA) explanatory supplement (Planck Collaboration 2013). The H I data is obtained from the ATCA+Parkes data (Kim et al. 1998, 2003). The FWHM beam size is smoothed to 5 arcmin by Gaussian smoothing. Hα data is from the Magellanic Cloud Emission-Line Survey (MCELS; Smith & MCELS Team 1999). The resolution is also smoothed to 5 arcmin. And finally the pixel size of the all data sets are unified to the Planck data (2 arcmin). The LMC is almost face-on, so the pixel-to-pixel comparison of the observed quantity on the 2-d image can be done without significant line-of-sight contamination. Note that the planck data is just extracted from the all-sky survey data, foreground galactic component is not subtracted, especially it affects the absolute value of the τ_{353}. This will be discussed in the following analysis.

The correction should be done in the range that the gas and the dust are well

mixed with uniform properties, so using the entire LMC is not good to estimate the local column density of the ridge. In this thesis, the opacity correction is performed to the area around LMC 4 and LMC 5. Figure 4.1 shows the area of the three data sets that are used in the analysis here. The region indicated by white line is the adopted area that roughly includes the entire LMC 4 and LMC 5. Figure 4.1(a) is the smoothed H I map. The H I show good spatial correlation with the CO molecular clouds. The positions of the SGSs LMC 4 and LMC 5 are indicated in this panel. Figure 4.1(b) is the τ_{353} map. The τ_{353} also shows good spatial agreement with the CO, but the correlation is clearer than the H I. The molecular clouds are distributed just around the τ_{353} is high. Figure 4.1(c) is the dust temperature map. $T_{\rm d}$ is high (>25 K) in the center and the south part of LMC 4. Even in the other area, the dust is not so cold ($\sim$ 22 K) on average.

In the area where heating of the UV radiation of massive stars and SNRs are significant, the relation of the gas and the dust may be largely different from the other area. So the data should be masked around such strong feedbacks can be seen. The masks are made where the Hα flux is significant (indicated by red lines in Figure 4.1). The threshold is $6 \times 10^7/4\pi$ [photons/cm^2/s/Sr], which can mask major H II regions and SNRs in this area.

A τ_{353}–$W_{\rm HI}$ scatter plot of the LMC 4 and LMC 5 are shown in Figure 4.2. Plotted points are colored by 1 K intervals every 1 K from 20 K. Compared with the Galactic case (Fig. 1.1), the dependence of the scatter on the dust temperature is not so clear. But it still can be seen that the the gas associated with the warmest dust (black dots) show the clearest linear τ_{353}-$W_{\rm HI}$ relation. Least-squares linear fits between $W_{\rm HI}$ and τ_{353} is made to the warmest dust plots. The best fit line is indicated as dashed line in the Figure 4.2. The slope k is 9.74×10^7 [K km s^{-1}] and the intercepts is -321.9 [K km s^{-1}] with a correlation coefficient of 0.73. The intercepts is rather large because the foreground Galactic component is not subtracted in τ_{353} data (for the H I data, the Galactic component is effectively cut off because the integrated velocity range is different). The intersection of the best fit line with X-axis is 3.3×10^{-6}. The average and the standard deviation of the τ_{353} around the north cavity of the LMC ($\sim$ 5h 50m; -65° $0'$) is $4.0 \pm 0.6 \times 10^{-6}$. This value may correspond to the ambient foreground emission. Since the values of the X-axis intersection and the roughly estimated foreground τ_{353} are similar, the best fit line should be across the origin if the foreground emission is completely subtracted from the τ_{353}. It is difficult to estimate actual foreground τ_{353}, so no detailed discussion will be done here. Instead, the slope of the intercept including fit, $k = 9.74 \times 10^7$ [K km s^{-1}], is adopted as the actual linear relation of $W_{\rm HI}$ and τ_{353} in this analysis.

If the H I is optically thin, the column density is estimated by Equation (1.1.24). Here the integrated intensity of H I is $W_{\rm HI}$, then the column density is expressed as

$$N_{\rm HI,thin} = 1.823 \times 10^{18} \cdot W_{\rm HI}. \tag{4.1.1}$$

The relationship between the τ_{353} and the column density of $N_{\rm HI,cor}$ is estimated for

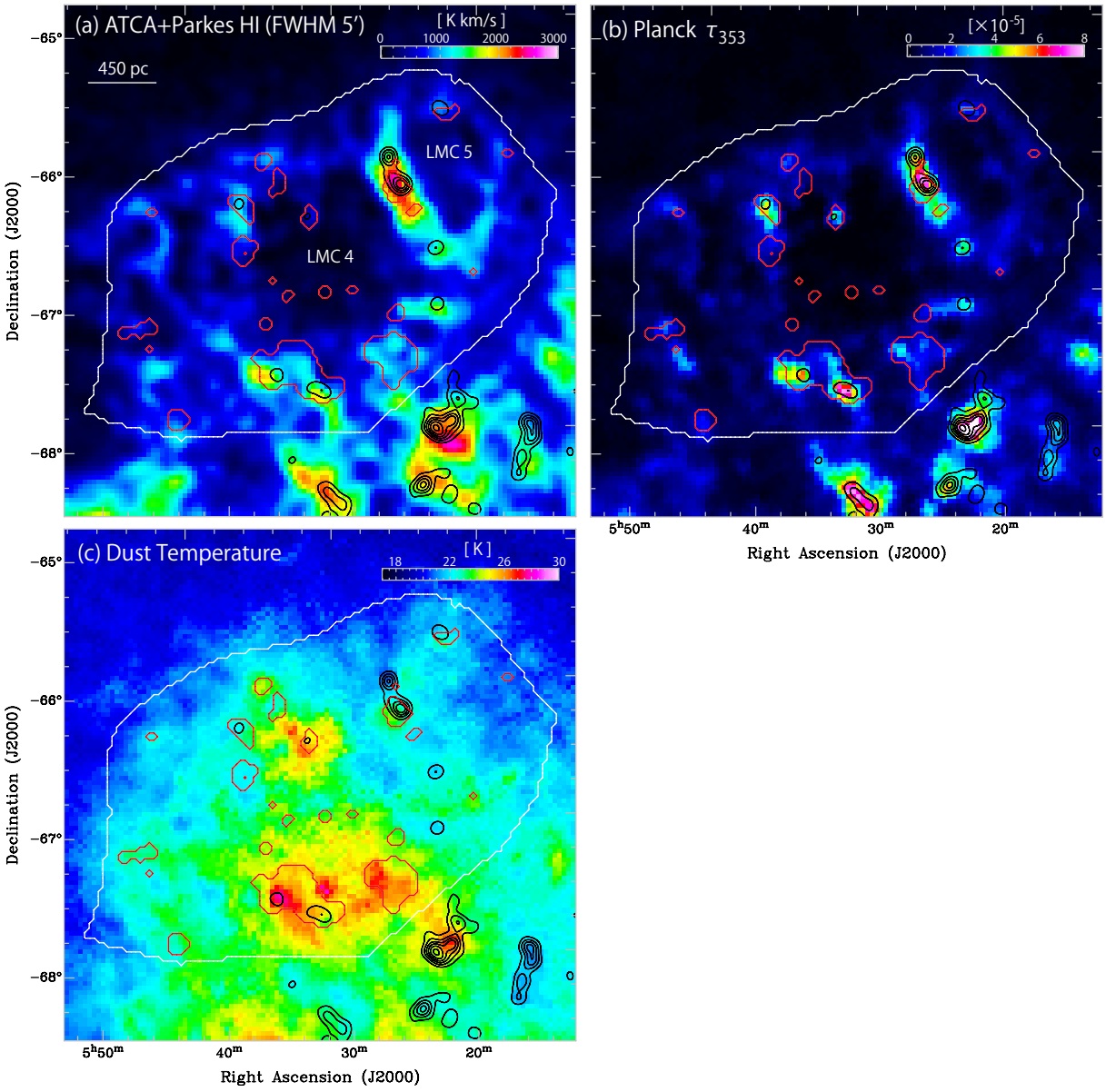

Figure 4.1: Three data sets that are used in the opacity correction analysis. The hole positions of LMC 4 and LMC 5 are indicated in the (a) panel. (a) Color map of H I integrated intensity of the Kim data (Kim et al. 2003), which is smoothed to the planck resolution of 5′. Black contours are the NANTEN ^{12}CO (Fukui et al. 2008), white large enclosure is the extracted area of the LMC 4 and LMC 5 for the analysis, and the red small enclosures are the masked area where Hα flux is significant ($> 6 \times 10^7/4\pi$ [photons/cm^2/s/Sr]). (b) Color map of τ_{353} of the Planck archive (Planck Collaboration 2013). (c) Color map of dust temperature of the Planck archive (Planck Collaboration 2013).

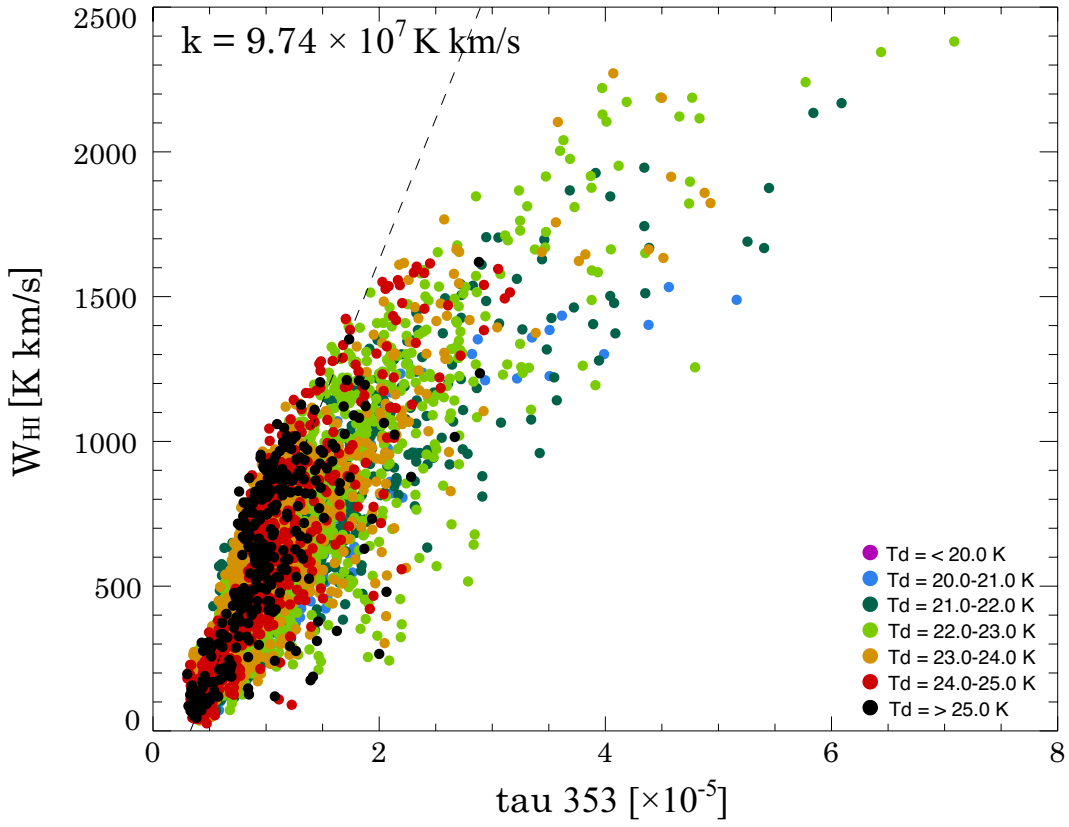

Figure 4.2: A scatter plot of τ_{353} and $W_{\rm HI}$ for the LMC 4 and LMC 5. Plotted points are colored by their dust temperature $T_{\rm d}$ in windows of 1 K intervals with steps of 1 K from 20 K. Dashed line is the best fit line to the $T_{\rm d} > 25$ K plot.

the optically thin regime at $T_{\rm d} > 25$K;

$$N_{\rm HI,cor} = (1.776 \times 10^{26}) \cdot \tau_{353}, \tag{4.1.2}$$

where 1.776×10^{26} is calculated by a product of 1.823×10^{18} (coefficient of Equation (4.1.1)) and the slope $k = 9.74 \times 10^{7}$ [K km s^{-1}] for $T_{\rm d} > 25$K.

The relation (4.1.2) holds as long as the dust properties are uniform. This allows us to calculate $N_{\rm HI,cor}$ from τ_{353} in the whole temperature range. If this gives the true column density of H I, spin temperature T_S and optical depth $\tau_{\rm HI}$ can be calculated from following coupled Equations,

$$W_{\rm HI}\ [\rm K\ km\ s^{-1}] = (T_{\rm S}\ [\rm K] - T_{\rm bg}\ [\rm K]) \cdot \Delta V_{\rm HI}\ [\rm km\ s^{-1}] \cdot (1 - \exp(\tau_{\rm HI})) \tag{4.1.3}$$

$$\tau_{\rm HI} = \frac{N_{\rm HI}\ [\rm cm^{-2}]}{1.823 \times 10^{18}} \cdot \frac{1}{T_{\rm S}} \cdot \frac{1}{\Delta V_{\rm HI}\ [\rm km\ s^{-1}]} \tag{4.1.4}$$

where $\Delta V_{\rm HI}$, the H I linewidth, is given by $W_{\rm HI}$/(peak H I brightness temperature) and $T_{\rm bg}$ is the background continuum radiation temperature including the 2.7 K cosmic background radiation (Fixsen 2009). $\tau_{\rm HI}$ is the optical depth of H I averaged over the H I velocity width $\Delta V_{\rm HI}$. Equation (4.1.4) is valid for any positive value of $\tau_{\rm HI}$. Equations (4.1.3) and (4.1.4) are corresponding to two independent lines in the T_S-$\tau_{\rm HI}$ plane. So it is able to estimate T_S and $\tau_{\rm HI}$ from the crossing point of two lines (see Figure 6 of Fukui et al. 2014). Note that in the optically thin limit, the two equations become essentially the same, and an infinite number of solutions is obtained. Only the lower limit for T_S and the upper limit of $\tau_{\rm HI}$ are constrained.

Figure 4.3 shows the distribution of modified τ_{353} (corresponds to the opacity corrected column density of the H I), and the estimated T_S and $\tau_{\rm HI}$. Several specific areas are masked as described in previously. The corrected H I column density shows clear spatial correlation with the distribution of the CO clouds. The high column density areas are found around the southern cloud (the N48 cloud) with $N_{\rm HI} \sim 1.3 \times 10^{22}$ [cm^{-2}]. The $\tau_{\rm HI}$ also shows good spatial agreement with the CO clouds. Unfortunately the southern part of the clouds are almost masked due to the presence of the H II region, the $\tau_{\rm HI}$ peak coincides with the northern CO cloud peak. The $\tau_{\rm HI}$ around the CO clouds is typically > 1.5, and ~ 2.9 at the peak. At the central part of the ridge $\tau_{\rm HI}$ is higher than unity. The H I tend to be optically thick in this area. The T_S shows no clear correlation with the CO clouds and the structure of the ridge. The T_S is typically > 100 K, roughly toward the side of LMC 4.

Figure 4.3(a) shows the spatial distribution of ratio of $N_{\rm HI,cor}$ (opacity-corrected column density) to $N_{\rm HI,thin} = 1.823 \times 10^{18} \cdot W_{\rm HI}$ (no-opacity-corrected column density). The ratio is apparently high (> 2) around the CO clouds. Figure 4.3(b) is the histgram of the ratio values. The ratio is greater than 1 for almost all pixels, and has a strong peak around 1.4. The histgram distribution seems to consist of two gaussian components; one has a peak around 1.4, and the other has a peak around 2.0. It can be interpreted as the two components roughly trace the diffuse gas and the dense gas

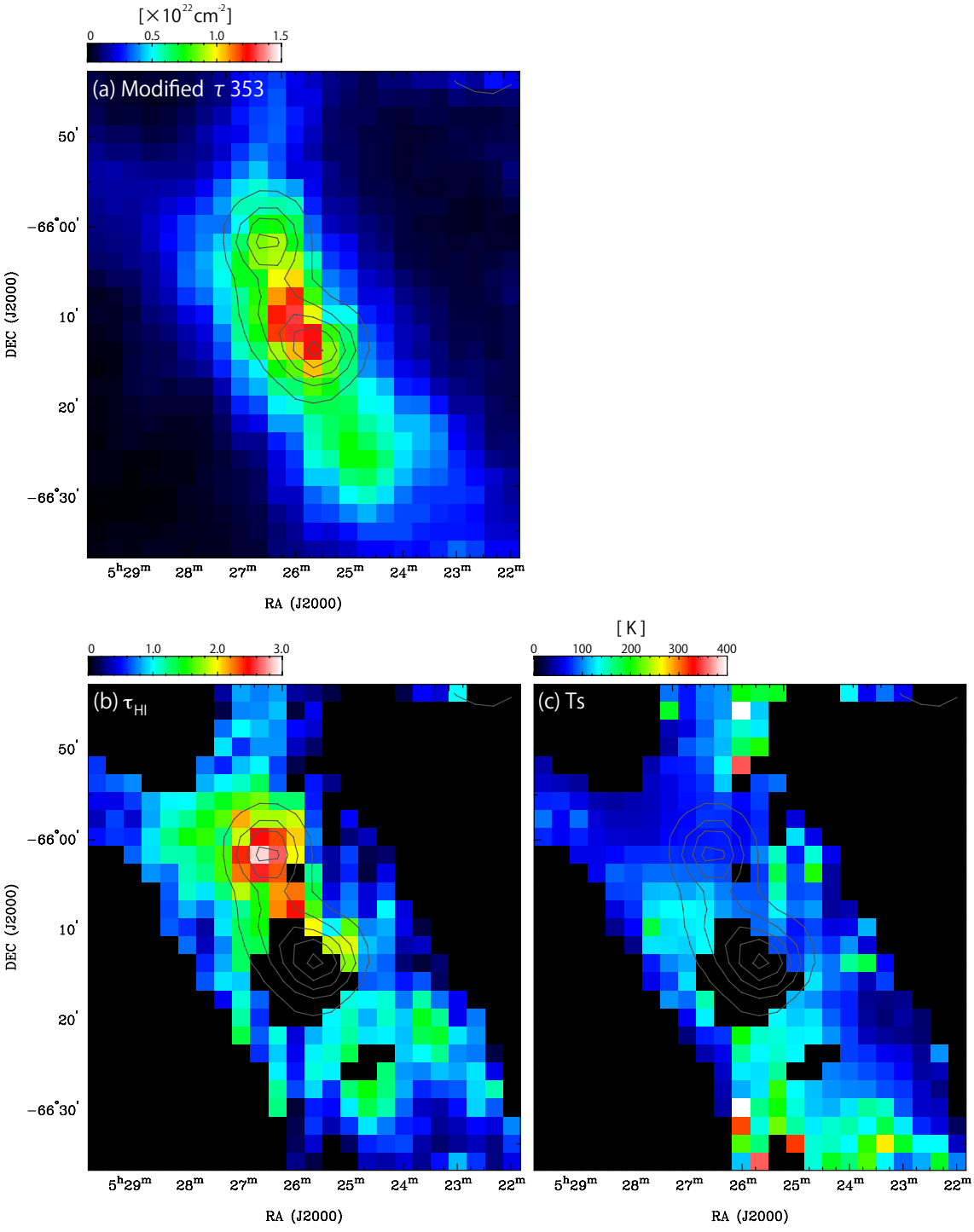

Figure 4.3: Three resulting maps of the opacity correction analysis. (a) Color map of the modified column density from Equation (1.1.25) with $k = 9.74 \times 10^7$ [K km s^{-1}]. Contours are the NANTEN ^{12}CO smoothed to the resolution of the Planck data (5′). The area where the H I is too faint is masked. (b) Color map of the optical depth of the H I $\tau_{\rm HI}$ derived from Equations (4.1.3) and (4.1.4). (c) Color map of the H I spin temperature $T_{\rm S}$ derived from Equations (4.1.3) and (4.1.4).

around the CO clouds, respectively. Spacial distribution of the high ratio components is concentrated around the molecular clouds. This two-phase distribution suggests that the τ_{353} not only traces the true column density of H I, but also traces the column density of H_2. This is not unusual when the gas to dust mass ratio is roughly uniform throughout the region. The total mass derived from $N_{\rm HI,cor}$ is $\sim 1 \times 10^7$ $M_\odot$, which might be a sum of the mass of the H I and the molecular clouds. Since the GMC mass is given as 1.5×10^6 (Yamaguchi et al. 2001a), the opacity corrected total H I mass of the ridge is $\sim 8.5 \times 10^6$ $M_\odot$. This is roughly 1.7 times greater than the no-opacity-corrected total H I mass.

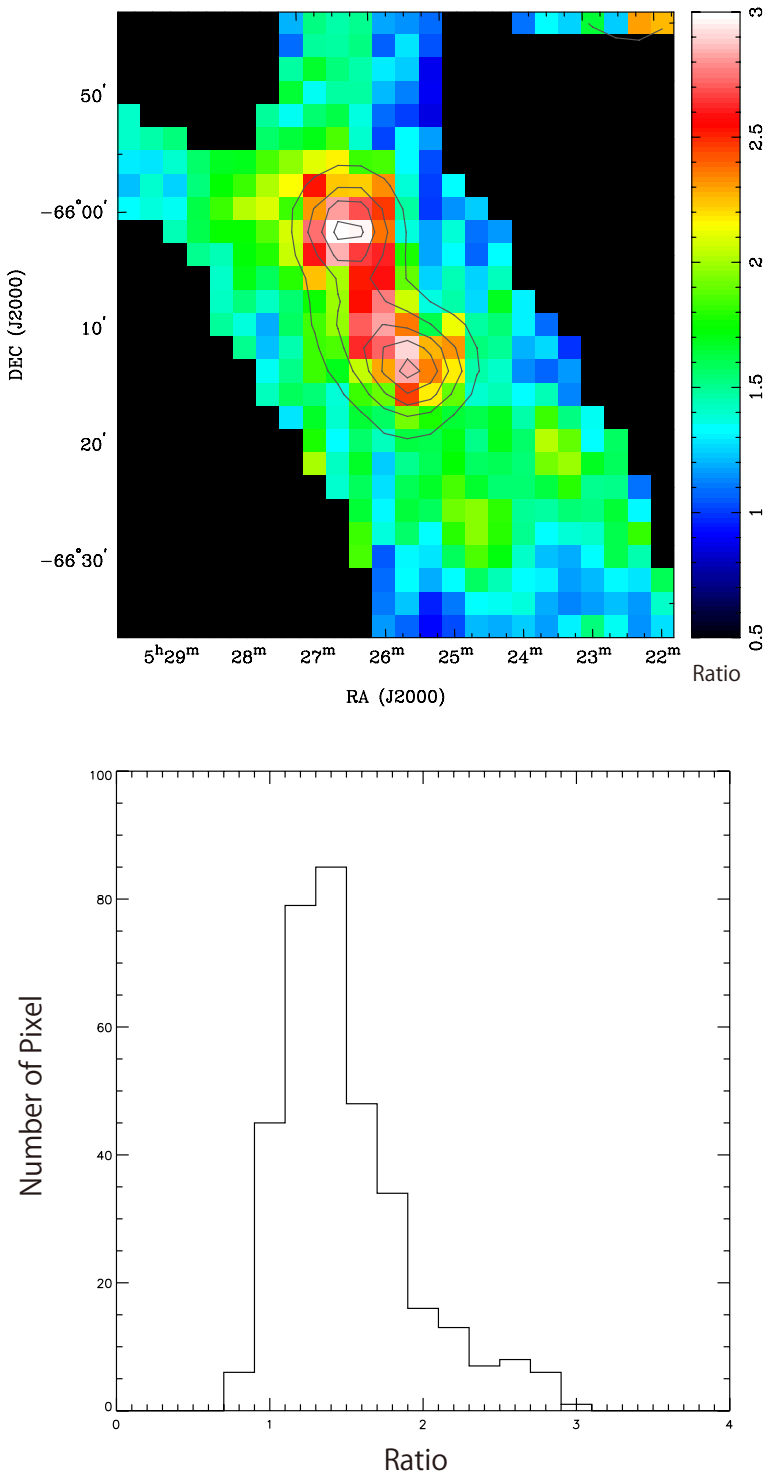

Figure 4.4: (a) Color map of the ratio of opacity-corrected $N_{\rm HI}$ to no-opacity-corrected column density. Contours are the NANTEN ^{12}CO smoothed to the resolution of the Planck data (5′). The data that is too faint in H I is masked. (b) Distribution of the ratio.

4.2 Filamentary Nature of the H I Ridge

4.2.1 Identification of Filamentary Features

As seen in the previous Chapter, the high-resolution morphology of the H I ridge is revealed to be highly filamentary. Such a filamentary nature of the ISM is typically found in the observation of dense clouds in our Galaxy (e.g., André et al. 2010). For the H I gas, filamentary H I is also found in the Galactic study (e.g., Martin et al. 2015), but the identification is done toward the diffuse H I at high-latitude. The filamentary structure of the H I ridge is the first result that reveals the highly filamentary nature of the H I gas around the GMCs and the star forming regions in the external galaxies. Identifying the filaments of the H I gas is important to understand the hierarchical nature of the ISM. Distribution, width, and mass of the filamentary structure are quite interesting to clarify the relation between the structure of H I gas and the formation of GMCs and dense molecular clumps.

On the other hand, computational identification of H I filaments is quite difficult. Almost no study has achieved to clearly identify the H I filaments. This is because the H I gas consists of two phase, the dense cold gas, and the diffuse warm gas. The diffuse component has a high temperature (> 100 K), so even an optically thin gas ($\tau < 0.1$) has a brightness temperature on the order of 10 K, that is comparable to that of the dense cold component. The dense and cold gas, which should be the main component of the H I filament, is often optically thick and the observed intensity is often underestimated. Due to these reasons, the contrast of the spatial distribution of the H I gas is typically smooth and unclear although the actual H I medium consists of the complex composition of the two phase components. And also, each component of H I gas has broad line width (more than 10 km s^{-1}), and consist a quite smooth spectrum. So the valley between the different spectral components is often difficult to separate. This can be seen in the typical spectrum of the H I ridge (Fig. 3.8), although the spatial distribution of the H I shows somewhat filamentary structure.

Taking these difficulties into account, here accurate identification of the H I filaments is given up. Instead, rough estimation of the distribution and the physical properties of the filamentary H I will be done with applying the core identification algorithm to the channel maps. Basic concepts are as follows. At first, the core identification algorithm is applied to each channel map in order to identify H I cores that show the position of local peaks and their rough extent. And then filaments are defined by eyes, drawing a line which can chain the cores along the ridge of the contours. The physical parameters of the filaments such as width, length, and line mass can be derived from those of the chained cores. This way of filament identification will give us rough estimate of the distribution and the parameters of the H I filaments. Of course the identification by eyes may suffer a large amount of uncertainties, and there is a danger of identifying the feature without any physical meaning. Here, the identified features will be called as "*filamentary features*", instead of filaments. The primary aim of the identification of the filamentary features in this work is that visualizing and quantifying the filamentary

nature of the ridge, so this rough identification method is the most reasonable way.

For the core identification process, Dendrogram is adopted (Rosolowsky et al. 2008). Structural analysis using Dendrogram has been performed to investigate hierarchical, cloud-to-core gas structures of position-position-velocity (PPV) space in several recent works (e.g., Goodman et al. 2009, Kauffmann et al. 2013). This method itself is also useful to identify filamentary structure in the dense clouds by selecting the cores with high aspect ratio (e.g., Lee et al. 2014, Storm et al. 2014).

The basic concepts of this hierarchical structure analysis is as follows. Dendrogram provides a tree diagram that characterizes how and where structures surrounding local maxima in the PPV space merge. Structures grow from the local maxima in the PPV volume with decreasing intensity level until they encounter adjacent structures. Local maxima in intensity become the "leaves" of the tree, which are the finest structure identified by Dendrogram, if they pass criteria used to suppress noise features. Two thresholds are set for the core identification criteria, one is "minimum value" that is simply to get rid of any structure peaking below this minimum, and the other is "minimum delta" that is to avoid including the local maxima that above the minimum value are only identified because of noise. The merge level, defined as the iso-contour which encircles two or more leaves, creates "branch" which grows in the PPV volume until it encounters another leaf or branch. Joining with a leaf or branch creates a lower level branch which can repeat the cycle of growth and merger until the minimum value of the flux density is reached.

Although the most profitable aspects of Dendrogram is to clarify the hierarchical structure of the clouds, it has also a unique pawer to identify the finest structure of the clouds. For the H I gas, all leaves are easily included in a single branch due to the contamination of the ambient component. So, identifying filaments just by picking up leaves or branches with high aspect ratio is not useful for the H I. But even in such case, chaining cores can be done without any difficulties. Dendrogram is a suitable tool for the identification of the filamentary features.

The identification of the filamentary feature is done according to the following steps.

1. Making channel maps of the H I of the new data. In this case, each channel is made by integrating 10 km s^{-1} velocity intervals. 10 km s^{-1} corresponds to the typical line width of the each H I component. The central velocity is started from 270.4 km s^{-1} with step of 5 km s^{-1}.

2. Identifying H I cores in each channel by Dendrogram. The minimum value is set to 0.065 [Jy/Beam·km s^{-1}] (corresponds to 5 sigma noise level of integrated intensity), and the minimum delta is set to 0.078 [Jy/Beam·km s^{-1}] for 285.4 to 300.4 km s^{-1} channels, and 0.065 [Jy/Beam·km s^{-1}] for the other channels.

3. Chaining the cores by eyes as filamentary features. Sequence of the cores that can be merged within elongated contours are chained by drawing a line along the contours. If the enclosing contours are too diffuse (typically wider than twice the size of the cores), these are excluded from the identification.

4. Elongated filamentary shape contours without cores are also identified as filamentary features. If any cores is found along the filamentary feature, they are included as the feature.

5. The end of the filamentary feature can elongate longer than the cores at both end if the contours show filamentary distribution. The end of the lines are roughly determined by seeing the distribution of the contours, including the adjacent channels.

6. If similar filamentary features are seen in more than 2 channels, the one channel is selected in which it looks the most prominent. This avoids the duplication in the identification, since the adjacent channel overlaps 5 km s^{-1} in their integration range. This does not mean dropping the filament detected in the less good channel.

7. If the velocity gradient of the filamentary feature is larger than the integration range of a channel (10 km s^{-1}), they should be identified in more than 3 channels. If filamentary features continue to elongate in more than 3 channels, these are merged in one.

Note that it is not sure whether the contiguous structures in the velocity channels are really contiguous in the 3D space or not. Since the line width of the H I gas is quite large, the contamination from the different spatial component may be significant for the H I case. However it is not able to distinguish the contamination, all contiguous structures in the velocity channels are regarded as the filamentary features here. Note also that the distribution of the H I is largely affected by the evacuation and the ionization by stellar feedbacks from massive stars, and the absorption of continuum sources. These effects will significantly affect the determination of the filamentary features. Actually, several deformation of the H I can be seen in the H I ridge (§3.2.1). In this study, the filamentary features are identified withut any correction or extrapolation on such deformations due to H II regions and SNRs. But for the absorption of the two background continuum sources, which are found in the north part of the H I ridge, the filamentary features are identified as if no H II depression were found around them. This is because essentially the background sources do not affect the distribution of the H I gas.

Figures 4.5 to 4.7 show the results of the identification. The features that are identified by the chain of the cores are shown in orange lines. Dashed lines are the features that is identified by the distribution of the contours. Cyan lines indicates the filamentary features that are identified in the adjacent channels (see point 6 of identification rules). They are shown in order to avoid duplication of the filamentary feature identification. Filamentary features were identified in almost all of the channels. In the 280.4 km s^{-1} and 285.4 km s^{-1} panels, clear spatial correlations with the CO and the filamentary features can be seen. This implies that the filamentary nature of the H I is key to their formation process. Although there are also prominent CO distribution

in the 290.4 km s^{-1} and 295.4 km s^{-1} panels, the filamentary features could not be identified around the central bright H I component (> 0.7 Jy/Beam·km s^{-1}). These velocity range corresponds to the central peak of the typical H I spectrum of the ridge. In such area, the H I gas is possibly getting optically thick, and the actual structures are buried in the smooth intensity distribution. Actually, the optical depth of the H I gas estimated in the previous section (Fig. 4.3) is greater than unity around such H I luminous area. On the other hand in the relatively diffuse part of the 285.4–295.4 km s^{-1} channels, several filamentary features can be seen. This suggests that the central bright H I area consists of the composition of several filamentary components, but the detailed distribution is hidden due to the high optical depth.

In the channels of both velocity ends (270.4 km s^{-1} to 280.4 km s^{-1}, and 300.4 km s^{-1} to 315.4 km s^{-1}), a lot of filamentary features are found regardless of the total H I opacity of the ridge. This indicates that the optical depth of the H I is relatively low at the edge of the spectrum. The number of the filamentary feature is greater in the red end of the channel maps (300.4 km s^{-1} to 315.4 km s^{-1}), than in the blue end (270.4 km s^{-1} to 280.4 km s^{-1}). In the blue end, the gas distribution is diffuse at the side of LMC 5, in such area no filamentary features is identified. In the red end, there are relatively less ambient components, and many filamentary features are found.

In total, 39 filamentary features are identified. Figure 4.8 shows the composition of the all identified filamentary features colored by their velocity range. The distribution of the filamentary features are rather complicated. It can be seen that the several filamentary features are roughly follow the detailed distribution of the dust. Most of the filamentary features distribute along the ridge direction, but several features are perpendicular to the ridge. The center of curvature of the filamentary features tend to be toward LMC 5. Several features are overlapping each other. But it is difficult to figure out the effects of such overlap on the molecular clump formation. This is because it is not able to see the detailed gas distribution around the molecular clumps in channel maps due to the complex composition and the high optical depth.

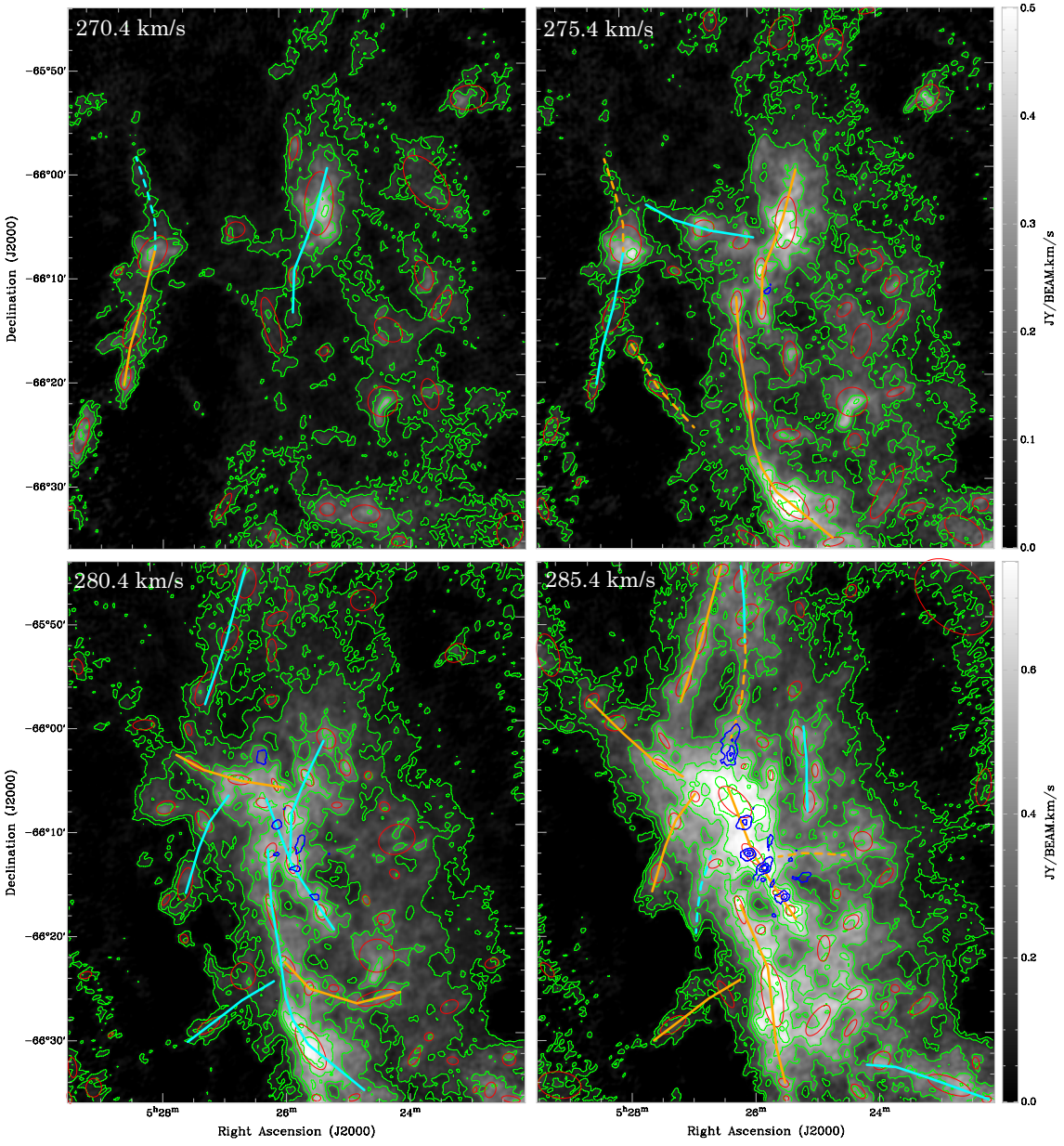

Figure 4.5: Channel maps for the identification of filamentary features. Channels of 270.4 km/s to 285.4 km/s are shown. Color and green contours are the H I integrated intensity of the new data. Contours are started from 5σ with step in 10σ (0.065 and 0.13 Jy/Beam km s^{-1}). Blue contours are the ASTE ^{12}CO(J=3–2) which started from 4 K km s^{-1} with step in 8 K km s^{-1}. Orange lines are the features identified by the chain of the cores, orange dashed lines are the features that is identified by the distribution of the contours, and cyan lines are those identified in different channels (see point 6 of identification rules).

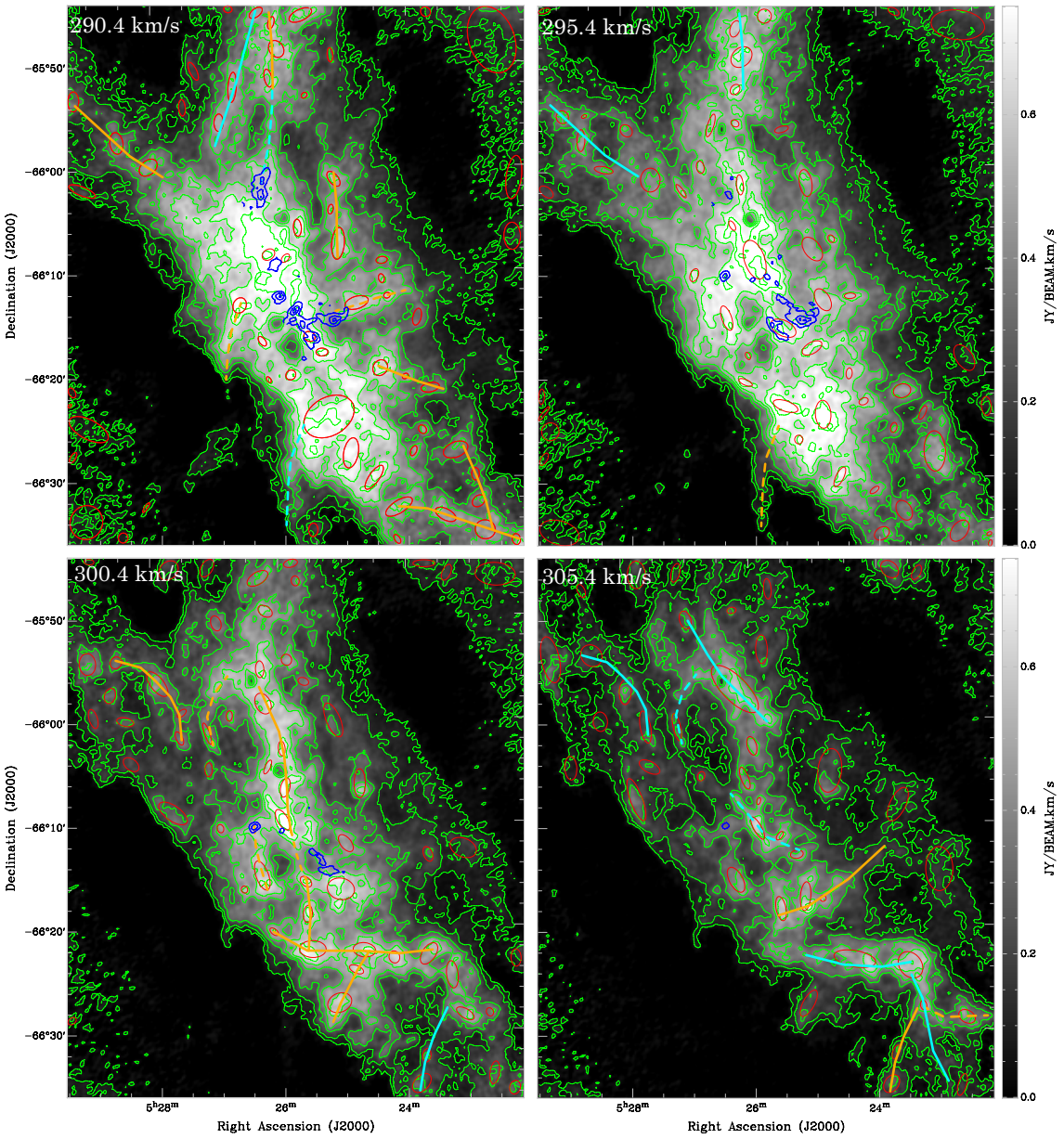

Figure 4.6: Continued channel maps for the identification of filamentary features. Channels of 290.4 km/s to 305.4 km/s are shown.

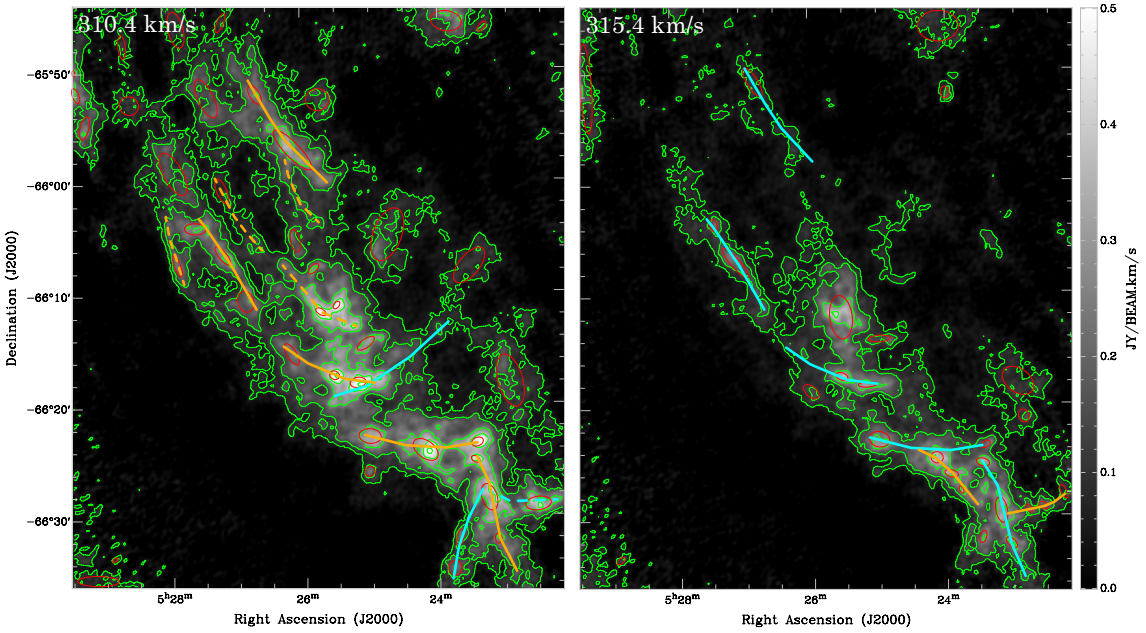

Figure 4.7: Continued channel maps for the identification of filamentary features. Channels of 310.4 km/s and 315.4 km/s are shown.

4.2.2 Physical Properties of the Filamentary Features

Physical properties of the filamentary features such as typical width, length, mass, and mass per line ratio (line mass) can be derived by the properties of the H I cores that are used for the identification of the filamentary features. Figure 4.9 shows a schematic view of the physical properties of the filamentary feature and the H I cores. With parameters given in Figure 4.9, the physical parameters of the filamentary features can be estimated as follows.

The width of the filamentary feature h is roughly given by the mean value of the FWHM diameter of the H I cores.

$$h \sim \frac{1}{N} \sum_{i=1}^{N} D_i, \tag{4.2.5}$$

where N is the number of the H I cores that are used for the identification. Each FWHM diameter D_i is derived by the geometric mean of the dispersion of the semi-major axis and the semi-minor axis that are the outputs of Dendrogram),

$$D_i = \sqrt{8 \ln 2 \cdot \sigma_{\mathrm{maj,i}} \sigma_{\mathrm{min,i}}}. \tag{4.2.6}$$

The precise determination of the length of the filamentary feature L is difficult, because the definition of the edge of the filamentary feature is quite loose. One reasonable estimation can be given by using the separation between the H I cores.

$$L \sim \sum_{i<j}^{N} l_{ij} + h. \tag{4.2.7}$$

Width of the filamentary feature h is added to include the extent of the edge of the cores. This equation is aplicable for the filamentary features that are identified just by the chain of the cores.

Total mass of the filamentary feature M is also difficult to be estimated, because the proper extent of the filamentary feature in the PPV area is not determined. One easy way to estimate the mass of the filamentary feature is just summing up the mass of the H I cores,

$$M > \sum_{i=1}^{N} m_i. \tag{4.2.8}$$

This gives the lower limit of the mass. Note that the mass of the H I core is just derived from the channel maps with integration range of 10 km s^{-1}, so some of the velocity components are out of integration range, and there may be contaminations from the other velocity components. But the actual extent of the components in the velocity space is difficult to be measured for almost all the filamentary features, since the spectrum of these features are significantly overlapped each other. Here Equation (4.2.8) is adopted for the rough estimation of the mass of the filamentary features. And

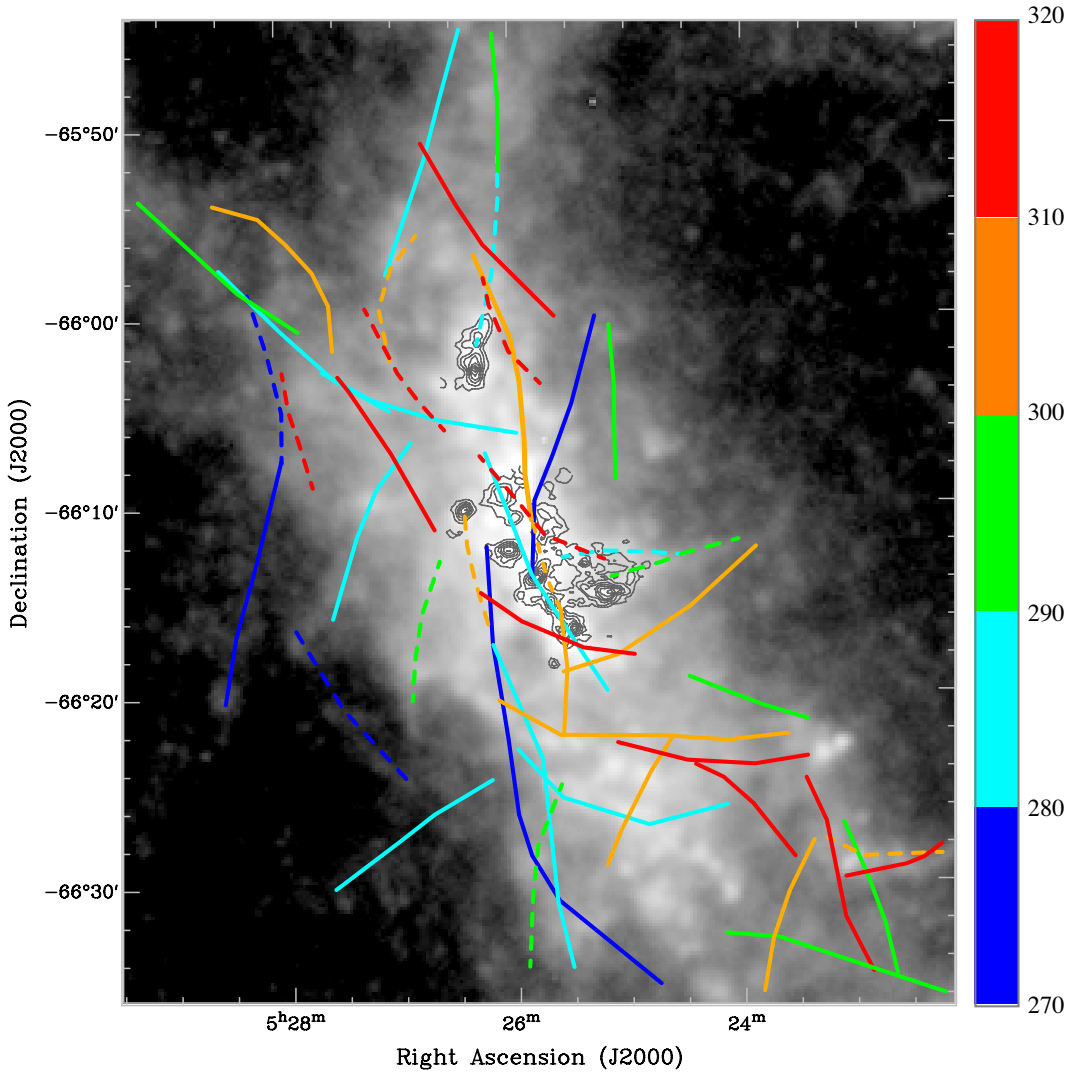

Figure 4.8: The composition map of the all identified filamentary features overlaid on the Herschel 500 μm image (Meixner et al. 2013). The filamentary features are colored by their velocity range.

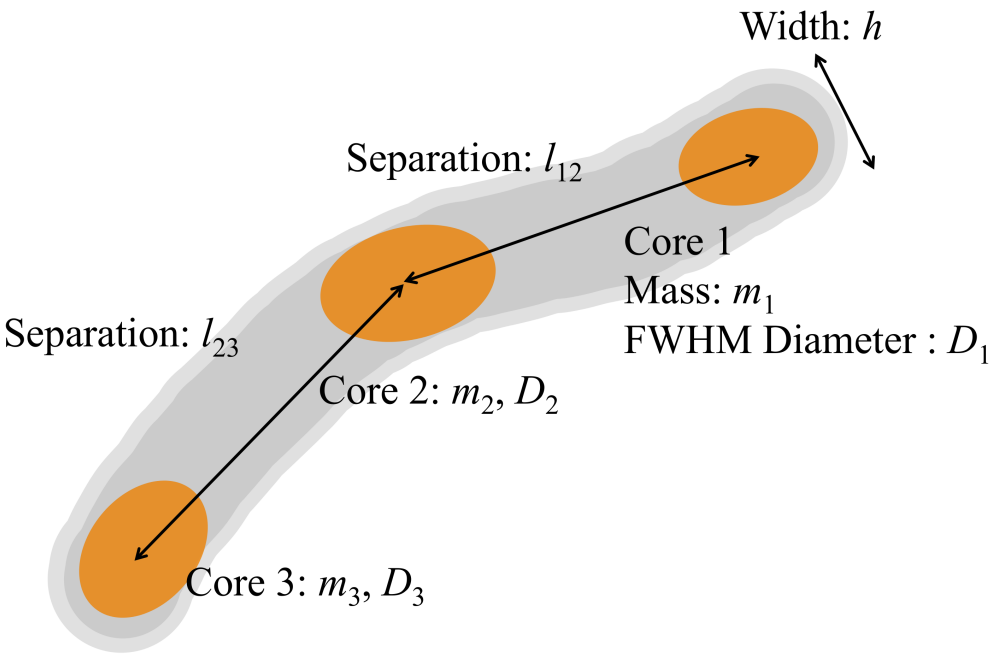

Figure 4.9: A schematic view of the physical properties of the filamentary feature.

it is also notable that the actual mass of the H I may be a few times higher than the mass just estimated from the intensity of the H I due to the optical depth of the H I is not thin (see previous section §4.1). The effect of this will be discussed later.

Line mass of the filamentary feature M_L can be estimated in two ways. One way is to just dividing the total mass of the filamentary feature M by their length L,

$$M_L \sim M/L. \tag{4.2.9}$$

This roughly gives the lower limit of the line mass. Another way is to derive the typical line mass around the H I cores. This can be derived from the average of the division of the mass of the H I cores by its FWHM diameter.

$$M_L \sim \frac{1}{N}\sum_{i}^{N}\frac{m_i}{D_i}. \tag{4.2.10}$$

This gives the upper limit of the line mass because it is calculated around the dense part of the filamentary feature. Here, the latter one is adopted for the estimation of the line mass.

The derived parameters are summarized in Table 4.10. Number distributions of each parameter is shown in Figure 4.10. The median (minimum–maximum) of each parameter is $h = 21$ [pc] (8–49 pc), $L = 118$ [pc] (11–400 pc), $M = 6200$ [$M_\odot$] (1600–21000 $M_\odot$) and $M_L = 90$ [$M_\odot$/pc] (20–190 $M_\odot$/pc). The most massive and prominent filamentary feature is that shows the molecular clump association (No. 11; $M = 21000$ $M_\odot$, $M_L = 190$ $M_\odot$/pc). The number distribution of the width h has strong peak around 20 pc within standard deviation of 7 pc, indicating that 20 pc is the typical width of the H I filamentary feature of the ridge. Filamentary features with this width are newly revealed structure by the high resolution observation, because they were almost spatially unresolved with spatial resolution of previous survey data (60″, $\sim$ 15 pc at the LMC). The diameter of the molecular clumps in the N48 and N49 regions is $\sim$ 10 pc, which is a little bit smaller than the 20 pc width of the filamentary features. The length and the mass of the filamentary features show rather wide distribution over the entire range. This is mainly due to the roughness of the definition of these parameters. The line mass of $M_L \sim 90$ [$M_\odot$/pc] corresponds to the averaged density of 10 [cm^{-3}] for 20 pc width cylinder. This is one order denser than the density of the WNM (< 1 cm^{-3}), which suggests that the filamentary nature of the H I is the results of the shock compressions of the SGSs. The upper limit density is ~ 20 [cm^{-3}] that is given from the line mass of $M_L \sim 190$ [$M_\odot$/pc]. Note that the column density of the H I increases by 1.4 to 2.0 if the actual opacity is taken into account (S 4.1). Thus the averaged density of the filamentary feature may be distributed in a range of 10 to 40 [cm^{-3}]. The theoretical critical line mass of the filaments are estimated by assuming isothermal, self gravitating cylinders with no magnetic support (Ostriker 1964):

$$M_{\rm L,crit} = 2c_{\rm s}^2/G \tag{4.2.11}$$

$$\sim 1.67 \times (T\ [{\rm K}])\ [M_\odot\ {\rm pc}^{-1}]. \tag{4.2.12}$$

Considering the spin temperature is 100–200 K in the H I ridge, the typical critical line mass is roughly 200–300 [$M_\odot$/pc]. The typical line mass of the filamentary features of the ridge (20–190 [$M_\odot$/pc]) is somewhat lower than this critical line mass. The most massive filamentary feature (No. 11, which is only one which shows the molecular clump association) is the closest to the critical values. And if the opacity correction factor of 1.4 to 2.0 is applied, entire values are getting to comparable to the critical values. So the mass of the filamentary features are slightly under the critical line mass. This is quite consistent with the fact that the almost all filamentary features show no molecular clump association. And this strongly suggests that the some evolution is required to the molecular clump formation in the filamentary H I gas. One notification here is that in actual case, prevention of the turbulence and the magnetic fields cannot be ignored for additional extra support of the filaments, so the discussion here is quite quite simple consideration.

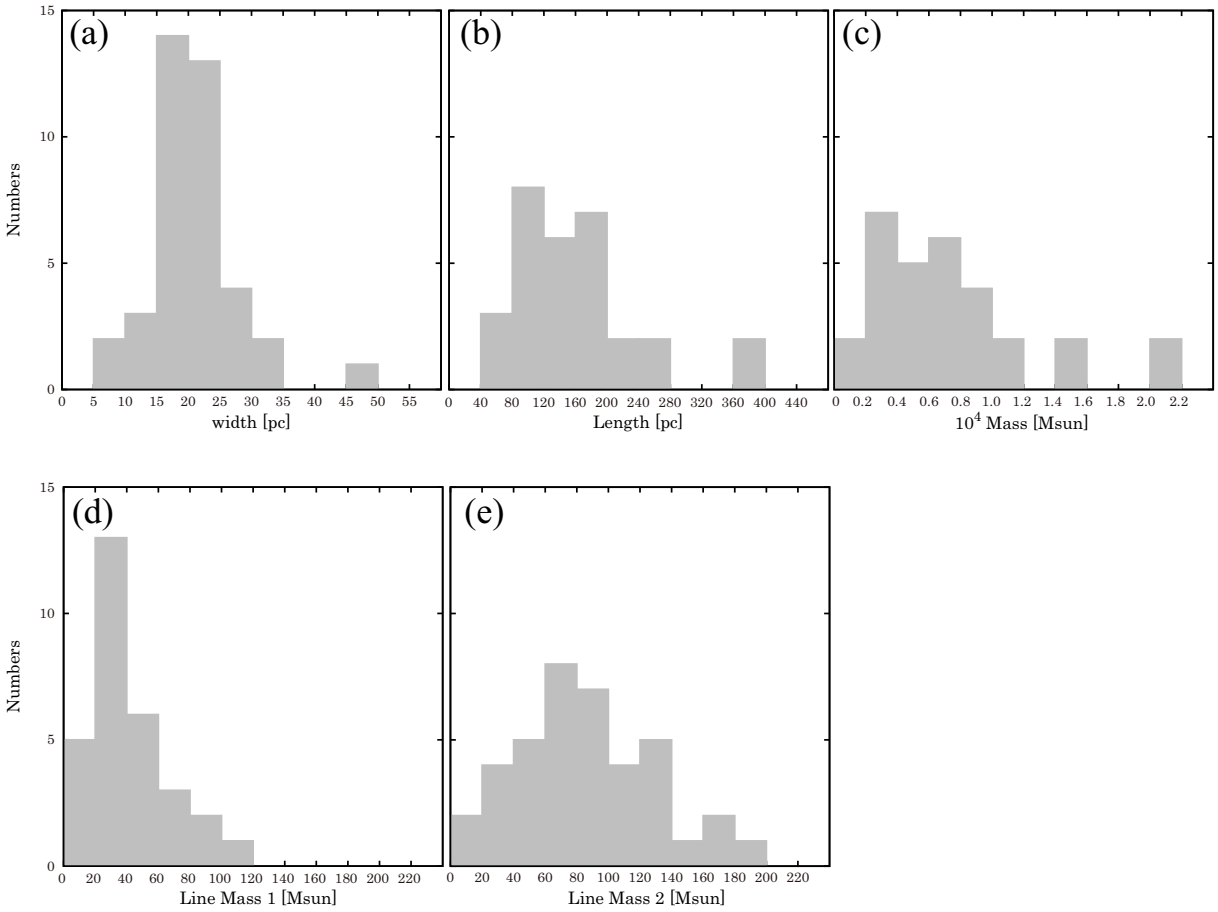

Figure 4.10: Histgrams of the physical parameters of the filamentary features. See Equation (4.2.5) to (4.2.10) for the detailed explanation of each paramenter.

Table 4.1: Parameters of filamentary features

Channel Velocity [km s^{-1}]	ID Number	Position of the Cores		Core parameters			Filament Parameters				
		R.A.($J2000$)	Dec($J2000$)	major axis	Diameter	Mass	Width	Length	Mass	Line Mass 1	Line Mass 2
		h:m:s	d:′:″	[pc×pc]	[pc]	[$M_\odot$]	[pc]	[pc]	[10^4 $M_\odot$]	[$M_\odot$/pc]	[$M_\odot$/pc]
270.4	1	5:28:32.2	-66:19:41.6	34×14	22	1100	34	180	0.74	40	58
		5:28:23.2	-66:15:2	56×26	38	1700					
		5:28:3.6	-66:7:48.7	56×33	43	3500					
275.4	2	5:24:44.1	-66:35:57.8	30×11	18	1100	26	370	1.5	57	90
		5:25:26.5	-66:32:0.4	69×30	45	9700					
		5:26:4	-66:22:45.5	40×13	23	1300					
		5:26:12.1	-66:17:18.5	40×14	24	1200					
		5:26:14.7	-66:12:53.2	33×14	22	1500					
	3	5:25:50.7	-66:13:34.9	27×12	18	1200	28	130	1.1	72	110
		5:25:50.8	-66:9:38.9	30×15	21	1500					
		5:25:26.5	-66:5:14.9	73×29	46	8700					
	4	5:27:31.6	-66:20:56.7	32×15	22	520	20				23
		5:27:54.7	-66:16:58.4	21×15	18	390					
	5	5:27:59.1	-66:7:0	54×44	49	6400	49				130
280.4	6	5:25:24.2	-66:18:16.9	23×14	18	1700	21	150	0.83	92	130
		5:25:50.9	-66:13:14.9	37×16	24	3900					
		5:25:53	-66:8:52.9	27×15	20	2700					
	7	5:24:31.8	-66:26:33.6	56×18	32	2900	23	140	0.6	60	88
		5:25:36.7	-66:25:35.2	19×13	16	1200					
		5:25:57.5	-66:23:14.6	31×14	21	1900					
285.4	8	5:25:32.9	-66:34:39.2	16×9.9	12	860	28	250	2.1	100	180
		5:25:42.8	-66:26:14.9	89×28	50	17000					
		5:26:12.3	-66:17:59.6	41×10	21	2600					
	9	5:27:2.4	-65:56:9.9	36×16	24	2300	22	170	0.66	67	99
		5:26:44.8	-65:51:46.8	43×13	23	2600					
		5:26:25.2	-65:45:16.8	23×16	19	1700					
	10	5:27:30	-66:14:18.4	27×20	23	2000	19	120	0.57	89	100
		5:27:13.3	-66:9:19.7	23×17	20	2300					
		5:26:53.5	-66:7:0	15×12	13	1400					

Col.(1): The central velocity of the channel in which the filamentary features are identified. Col.(2): Serial numbers of the filamentary features. Col.(3)(4): Central positions of H I cores that are used for the identification of the filamentary features. Col.(5)(6)(7): Major and minor axis, geometric mean diameter of the equivalent ellipse, and corresponding mass of the H I cores. Col.(8)(9)(10)(11)(12): Parameters of the filamentary features. Corresponding equations are (4.2.5), (4.2.7), (4.2.8), (4.2.9), and (4.2.10). Length, mass, and line mass 1 for filamentary features that are identified by the contour distribution cannot be derived, and empty value is listed here.

Table 4.2: Filament Parameters

Channel Velocity [km s^{-1}]	ID Number	Position of the Cores R.A.($J2000$) h:m:s	Dec($J2000$) d:′:″	Core parameters major axis [pc×pc]	Diameter [pc]	Mass [M$_\odot$]	Filament Parameters Width [pc]	Length [pc]	Mass [10^4 M$_\odot$]	Line Mass 1 [M$_\odot$/pc]	Line Mass 2 [M$_\odot$/pc]
	11	5:25:24.4	-66:18:6	14×14	14	1800	23	170	2.1	140	190
		5:25:35.8	-66:16:27.5	16×9.1	12	1300					
		5:25:59.5	-66:12:41.1	39×17	26	5500					
		5:26:15.4	-66:7:37.1	57×28	40	13000					
	12	5:27:18.8	-66:28:53.5	40×19	27	1200	25	85	0.2	24	38
		5:26:27.5	-66:26:3.7	42×13	23	710					
	13	5:26:6.3	-66:5:55.8	19×6.5	11	700	19	340	0.75	46	67
		5:26:40.2	-66:5:23.9	31×13	20	2000					
		5:27:21.4	-66:3:55.6	27×7.5	14	710					
		5:28:7.5	-65:59:44.1	30×21	25	1700					
		5:28:29.4	-65:57:31.4	25×16	20	1100					
		5:29:14.2	-65:53:14	28×15	21	1400					
290.4	14	5:22:46.1	-66:35:10.4	28×26	27	3100	21	120	0.76	70	81
		5:22:52.5	-66:32:26.4	20×15	17	1200					
		5:22:55.5	-66:29:50.3	17×11	14	570					
		5:23:14.6	-66:27:29.3	36×21	28	2800					
	15	5:22:16	-66:36:7.1	15×11	13	980	23	170	1	83	110
		5:22:46.1	-66:35:10.4	28×26	27	3100					
		5:23:24.5	-66:33:43.5	32×16	22	2500					
		5:24:9.6	-66:32:57.3	43×18	27	3400					
	16	5:25:5.9	-66:7:30.5	45×18	28	4700	19	92	0.71	74	110
		5:25:12.6	-66:4:11.9	14×7.4	10	590					
		5:25:9.4	-66:1:16.2	25×13	18	1800					
	17	5:26:10	-65:51:25.7	26×11	16	920	17	80	0.42	60	78
		5:26:1.8	-65:48:37.5	25×20	22	2400					
		5:26:6.6	-65:46:5.3	18×8.4	12	890					
	18	5:24:48.8	-66:13:14.3	34×17	24	3400	16	44	0.39	79	100
		5:24:19.6	-66:12:34.2	9.3×7.8	8.5	530					
	19	5:26:40.6	-66:13:19	22×18	20	2900	20				140
295.4		no data									
300.4	20	5:23:40	-66:22:48.2	34×19	25	3000	21	220	1.5	100	130
		5:24:13.4	-66:23:6.3	17×15	16	1900					
		5:24:42.2	-66:22:23.5	32×20	25	3600					
		5:25:31.9	-66:22:14.3	37×24	30	6100					
		5:26:8.6	-66:20:31.6	14×7.7	11	680					

(Continued Table)

Table 4.3: Filament Parameters

Channel Velocity [km s^{-1}]	ID Number	Position of the Cores R.A.($J2000$) h:m:s	Dec($J2000$) d:′:″	Core parameters major axis [pc×pc]	Diameter [pc]	Mass [M$_\odot$]	Filament Parameters Width [pc]	Length [pc]	Mass [10^4 M$_\odot$]	Line Mass 1 [M$_\odot$/pc]	Line Mass 2 [M$_\odot$/pc]
	21	5:25:31.9	-66:22:14.3	37×24	30	6100	21	95	0.99	110	150
		5:25:36.2	-66:18:50.7	24×13	17	2200					
		5:25:37.6	-66:15:44.4	19×12	15	1600					
	22	5:25:58.9	-66:9:43.8	32×14	22	4100	19	220	1.2	83	120
		5:25:55.9	-66:6:38.8	27×13	19	1700					
		5:25:58.8	-66:2:51	21×9.5	14	1400					
		5:26:15.7	-65:58:28.5	31×21	25	2400					
		5:26:18.4	-65:55:8.9	24×12	17	1800					
	23	5:27:35.6	-66:1:40.2	20×9	14	740	17	150	0.51	47	65
		5:27:33.1	-65:59:14.6	16×7.9	11	490					
		5:27:55.7	-65:56:22.3	42×18	28	3100					
		5:28:34.2	-65:54:11.4	17×15	16	850					
	24	5:25:6.5	-66:27:27.3	35×26	30	4600	24	82	0.98	110	130
		5:24:49.9	-66:24:16	21×11	15	1600					
		5:24:42.2	-66:22:23.5	32×20	25	3600					
	25	5:26:19.3	-66:15:5.3	43×17	27	4600	27				170
	26	5:27:9.3	-66:1:15.6	32×7.1	15	1100	15				71
305.4	27	5:23:48.3	-66:35:17.9	28×20	23	1400	16	120	0.26	42	52
		5:23:43.7	-66:32:15.1	20×9.2	14	480					
		5:23:17	-66:27:45.3	14×9	11	650					
	28	5:22:35	-66:28:52.8	25×17	21	1800	17	63	0.25	60	73
		5:23:17	-66:27:45.3	14×9	11	650					
	29	5:25:33.3	-66:18:19.2	34×14	22	2600	18				100
		5:25:9.7	-66:17:9.2	40×15	24	3300					
		5:24:52.9	-66:17:23.4	8.6×8.3	8.5	430					
310.4	30	5:23:7.7	-66:32:12.9	13×8.5	10	350	16	110	0.32	43	56
		5:23:15.7	-66:28:31.1	35×20	26	2400					
		5:23:27.8	-66:25:7.4	12×7.5	9.6	450					
	31	5:25:2.1	-66:22:58.7	29×19	23	2000	22	140	0.61	71	89
		5:24:12.7	-66:24:14.5	37×22	29	3100					
		5:23:26.3	-66:23:33.8	16×11	13	970					
	32	5:25:12.5	-66:18:9.5	21×13	16	1600	16	94	0.33	56	70
		5:25:33.2	-66:17:30.1	13×11	12	840					
		5:26:11.1	-66:15:33.6	31×12	20	900					

(Continued Table)

Table 4.4: Filament Parameters

Channel Velocity [km s^{-1}]	ID Number	Position of the Cores		Core parameters			Filament Parameters				
		R.A.(J2000) h:m:s	Dec(J2000) d:′:″	major axis [pc×pc]	Diameter [pc]	Mass [M$_\odot$]	Width [pc]	Length [pc]	Mass [10^4 M$_\odot$]	Line Mass 1 [M$_\odot$/pc]	Line Mass 2 [M$_\odot$/pc]
	33	5:26:51.1	-66:10:45.4	28×21	24	1200	21	120	0.32	38	53
		5:27:10.6	-66:6:36.6	30×10	18	970					
		5:27:34.6	-66:4:9.8	28×15	20	1100					
	34	5:26:7.5	-65:57:14.7	70×19	36	3500	31	87	0.43	39	68
		5:26:40	-65:52:13.4	27×13	19	740					
	35	5:25:44.6	-66:11:46.8	15×7.6	11	620	11				58
	36	5:27:10.6	-66:0:49.7	34×13	21	480	21				23
	37	5:27:51	-66:7:25.7	29×8.1	15	590	15				38
315.4	38	5:23:11.8	-66:29:36.4	33×15	22	1700	7.8	88	0.23	22	32
		5:22:47.2	-66:29:29.3	12×5.9	8.6	140					
		5:22:34	-66:29:13.1	13×8.1	10	240					
		5:22:15.7	-66:27:59.4	19×7.7	12	170					
	39	5:23:47.6	-66:27:47.2	10×4.9	7	170	9.9	53	0.16	34	41
		5:23:56.2	-66:26:19.3	18×9.2	13	410					
		5:24:9.3	-66:24:52.4	16×15	15	1000					

(Continued Table)

4.3 Global Kinematics of the H I Ridge

The global kinematics of the H I ridge will give us a special clue to understand the dynamical mechanism of the molecular cloud formation. The distribution of the H I medium in the 3 dimensional space (position-position-velocity) largely reflects the dynamical effects of the ISM such as gravitational infall, collapse induced by instabilities, and shock compression of expanding shells. For the H I ridge, there are several questions to be clarified. Can dynamical effects of the shells be seen around the GMCs? Is the H I ridge radially collapsing, or fragmenting along the ridge? Can the H I accreting to the molecular clouds be seen? Since the line-of-sight velocity is a good indicator of the kinematics of the medium, the dominant dynamics of the H I medium can be visualized by the position velocity diagrams of the H I gas.

Position Velocity Diagrams: Perpendicular Cut

Figure 4.11 shows the position velocity (P–V) diagrams of the H I and the CO of the direction perpendicular to the ridge. From these perpendicular cut, the radial motion of the ridge and the effects of the two SGSs can be visualized. Two extreme resolution images are prepared ($\sim 156''$ and $\sim 25''$, corresponds to ~ 38 pc and ~ 6 pc at the LMC distance) in order to see both the global and the local kinematics. For the low resolution data, archival Kim et al. H I data and the NANTEN ^{12}CO(J=1–0) data are used. The beam size is smoothed by the gaussian deconvolution to the NANTEN ^{12}CO(J=1–0) beam size ($\sim 156''$, ~ 40 pc at the LMC). For the high resolution data, the new ATCA H I data and the ASTE ^{12}CO(J=3–2) are used. Since the difference of the beam size of these two data set is slight ($\sim 25'' \times 20''$ and $\sim 27''$, $\sim$ 5–7 pc at the LMC), no beam smoothing is applied. Data cut is performed at 5 positions (A to E in the Figure 4.11). The positions A and E are the typical points of the northern and the southern end of the ridge. The position B is around the peak position of the GMC in the N49. The positions C and D are the two peak positions of the GMC in the N48.

In the low resolution P–V diagrams, the H I is quite smoothly distributed both in the postion and the velocity directions. Especially at the positions C and D, the H I shows no complex sub-structures and almost axi-symmetric, ellipse-like (2nd order gaussian like) distribution at the bright part ($>$ 1 K Degree), that is, the line width is the broadest around the center and is getting narrower towards the edge. This tendency is roughly shown as red dashed ellipses in the figure. On the other hand, at the positions A, B, and E, the H I shows several sub-components. At the positions A and E, there are more than two peaks along the position direction, and at the positions B and E, the H I distribution and the central velocity of the H I components are somewhat distorted towards the both side of the shells. These features indicates that the two shells are not well mixed (A, E), and the shape of the H I distribution is affected by the shells (B, E). ^{12}CO(J=1–0) contours are roughly distributed around the peak of the H I in the positions B, C, and D. In this size scale, the CO and the H I show good spatial agreement and there is no H I depression by the conversion of H I into H_2 molecules.

In the high resolution P–V diagrams, basic structure of the H I is roughly similar to the low resolution images, but complicated sub-structures are rather revealed. Even in the positions C and D, the main H I component seems to consist of the composition of several sub-components. Such sub-components may correspond to the filamentary features that are identified in the previous section. In the positions C and D, although some sub-structures make the H I distribution rather complex, the rough shapes of bright part are still axi-symmetric and elliptical (within red dashed ellipses in the figure). Note that in the position D, H I depression due to the H II region N48 can be seen just next to the molecular clumps. In the diffuse part (< 0.6 K Degree), the distribution is getting irregular and the line width getting broader especially towards the side of LMC 5. So, even the main component of the H I seems to be well mixed together, while the diffuse component still reflects the disturbance by the shells. Toward the side of LMC 4, the strong cut off of the H I can be seen, so the H I might be blown out by the shell. The CO contours are quite compact compared to the low resolution image, since the resolution is quite higher with higher density tracer (^{12}CO(J=3–2)) observation. The peak positions of the CO are a bit away from the peak of the H I in both spatial and velocity directions, except for the C position. Even the rough structure is mixed together in one large component, the dense molecular clumps may be formed in the sub-components, not always in the center of the main component.

Position Velocity Diagrams: Parallel Cut

Figure 4.12 shows the P–V diagrams of the H I and the CO of the direction parallel to the ridge. The same two resolution images are prepared as the perpendicular cut (Figure 4.11). Data cut is performed at 5 positions (A to E in the Figure 4.11). The positions C and D pass on the strongest clump peak positions of the N48 and N49 regions, A and E pass typical area of the diffuse part of the ridge, and the position B passes on the H I depressed area of the H II region N48.

In the velocity cuts near the center axis (B, C, and D) of the low resolution P–V diagrams, the H I shows straight elongation of roughly constant one peak $V_{\rm lsr}$ with $\sim$ 600 pc length. To see this clearly, dashed line of $V_{\rm lsr} = 295$ km s^{-1} is indicated in the figure. The velocity width of the H I is roughly constant (~ 20 km s^{-1}) along the ridge. Although the peak $V_{\rm lsr}$ of the CO clouds is similar to the H I, the CO clouds take a little bit spatially offset from the strongest H I envelope (offset position $\sim$ 400–500 pc). The shape of the H I is rather complex in the velocity cuts at the diffuse part of the ridge (A and E), in which the peak $V_{\rm lsr}$ is winding, and several sub-components can be seen.

In the parallel cut, the high resolution P–V diagrams show rather resolved distribution of the ridge. In the position C, winding of the peak $V_{\rm lsr}$ is seen especially around the molecular clumps of the N48 region (offset position $\sim$ 300 pc). In the position D, the distribution of the molecular clumps avoids the H I bright area. H I depression due to the H II region N48 is clearly seen in the position B (offset position $\sim$ 250–300 pc). The depressed velocity range is quite wide, indicating that the H II region punches

holes. A hole of the H I depression due to the SNR N49 is also seen in D position (offset position $\sim$ 250–300 pc, $V_{\rm lsr} \sim 290$ km s^{-1}).

Interpretation of the P–V Diagrams

The most important finding from the P–V diagrams is achieved from the perpendicular cut; the main part of the H I seems to be well mixed in one large component at the two shell interacting area (around the GMCs in the N48), but rather complex in the other area. This axi-symmetric, elliptical distribution in the P–V diagram implies that the gravitational evolution plays an important role around the shell interacting area. Since such an elliptical shape P–V is offen seen in the P–V of a spherical molecular cloud, the origin of this axi-symmetric distribution can be interpreted in the similar logic; the gas is free falling or sustained by turbulence (turbulent accretion). In either case, the H I envelope feeds a mass to the GMCs, as suggested in Fukui et al. (2009). However it is quite difficult to distinguish the two cases. Even for the Galactic GMCs, although they are commonly considered to be sustained by turbulence, their supersonic velocity dispersion is also interpreted as a hierarchical gravitational collapse of the clouds (e.g., Ballesteros-Paredes et al. 2011).

The radial (infall) velocity of the ridge can be simply expressed as,

$$v_{\rm infall}(r) = v_{\rm infall,0} \left(\frac{r}{r_0} \right)^{\alpha}, \tag{4.3.13}$$

where r is a radial position, α is a power of the dependence on r, and subscript 0 indicates the values at the outer edge of the ridge. Figure 4.13 shows the schematic images of the P–V diagrams for a uniform density cylinder.

When $\alpha > 0$ (Fig. 4.13(a)), the cylinder is radially collapsing. In such cylinder, the P–V diagrams should be elliptical (2d-gaussian-like). Since observed velocity dispersion of the molecular clouds are always smaller than the surrounding H I envelopes, and smaller clouds show smaller velocity dispersion (size-linewidth relation), $\alpha > 0$ also indicates the the cylinder is in a state close to a usual turbulent cloud. If the cylinder is free falling (Fig. 4.13(b)), the infall velocity is getting faster according to the gas is falling inside, then $\alpha < 0$. So the P–V diagram should be in a shape of inverse proportion, if the gas is optically thin. This also gives an axi-symmetric P–V diagram with the broadest line width at the center, if the central fast-infalling components are converted into molecular clouds with narrower line width. If the cylinder is affected by expanding shells from the both side of the P–V cut (Fig. 4.13(c)), the edge-shape of the P–V diagram is largely affected by the shells. If the cylinder is formed by the collision of the two shells, the central velocity is not uniform and may have a gradient within the cut.

Taking these simple models into account, axi-symmetric, elliptical distribution in the P–V diagram at the shell interacting area suggests that no clear shell effects remains and now the gravitational evolution plays an important role to confine the ridge.

Detailed discussion about this observational suggestion will be done in the following section.

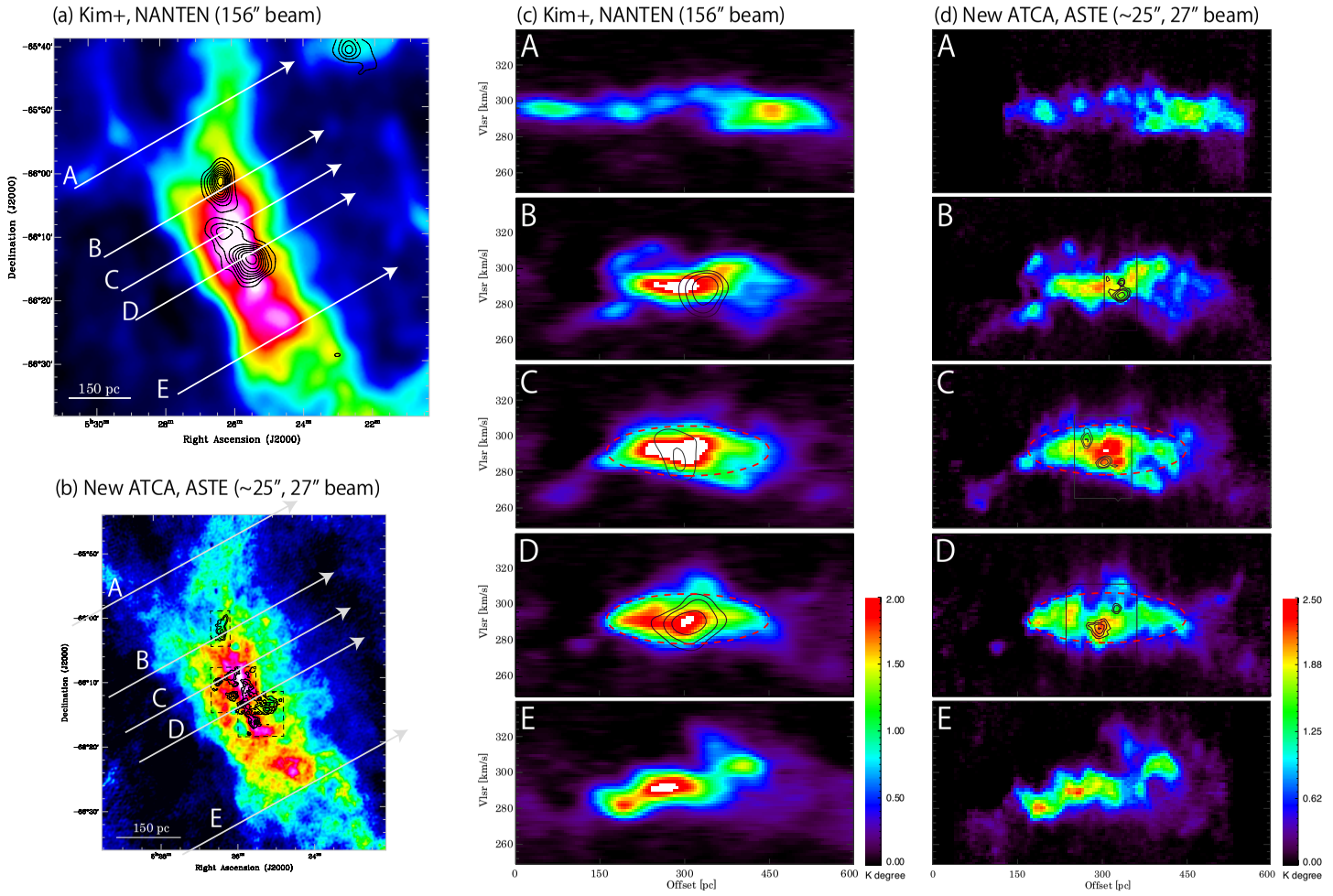

Figure 4.11: Five position-velocity diagrams perpendicular to the ridge for the NANTEN resolution (156″) and the new H I resolution (∼ 25″). (a) Map of the entire ridge to specify the position cut of the diagrams. Color map is smoothed-beam H I (Kim et al. 2003) with contours of the NANTEN ^{12}CO(J=1–0) (Fukui et al. 2008). White arrows are the position lines for each diagram. Red dashed line ellipses in C and D position represent the axi-symmetric, elliptical structure of the P–V diagram. (b) The same map for the high resolution data sets. Color map is the new H I data of $\sim 25'' \times 20''$ beam with contours of the ASTE ^{12}CO(J=3–2) $\sim 27''$ beam data. White arrows are the same position lines as (a). (c) P–V diagrams for the low resolution data sets. (d) P–V diagrams for the high resolution data sets.

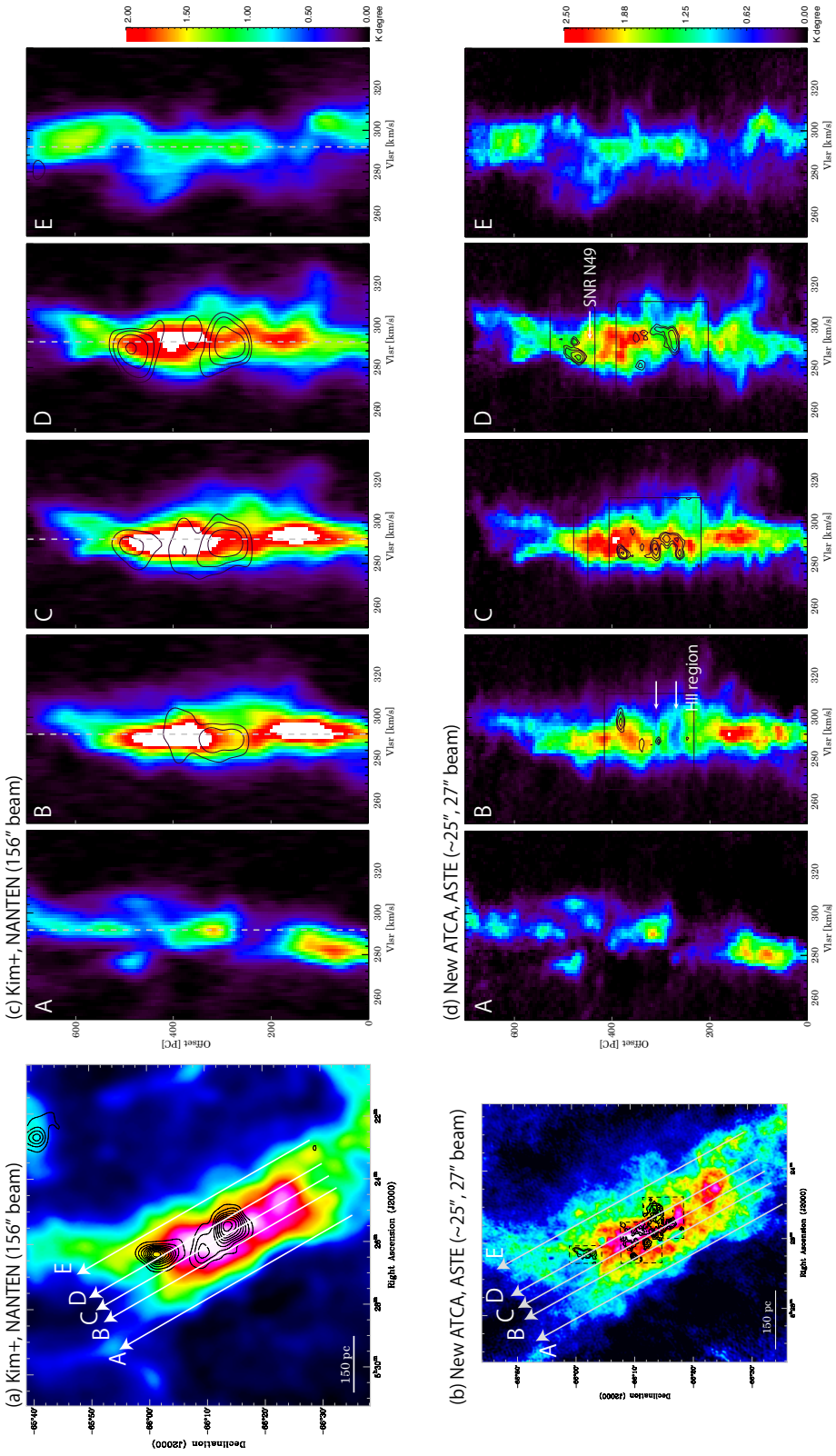

Figure 4.12: Five Position-Velocity Diagrams along the ridge with 156″ resolution. The information is the same as the Figure 4.11. Gray dashed lines in the low resolution images indicate $V_{\rm lsr} = 295$ km s^{-1}.

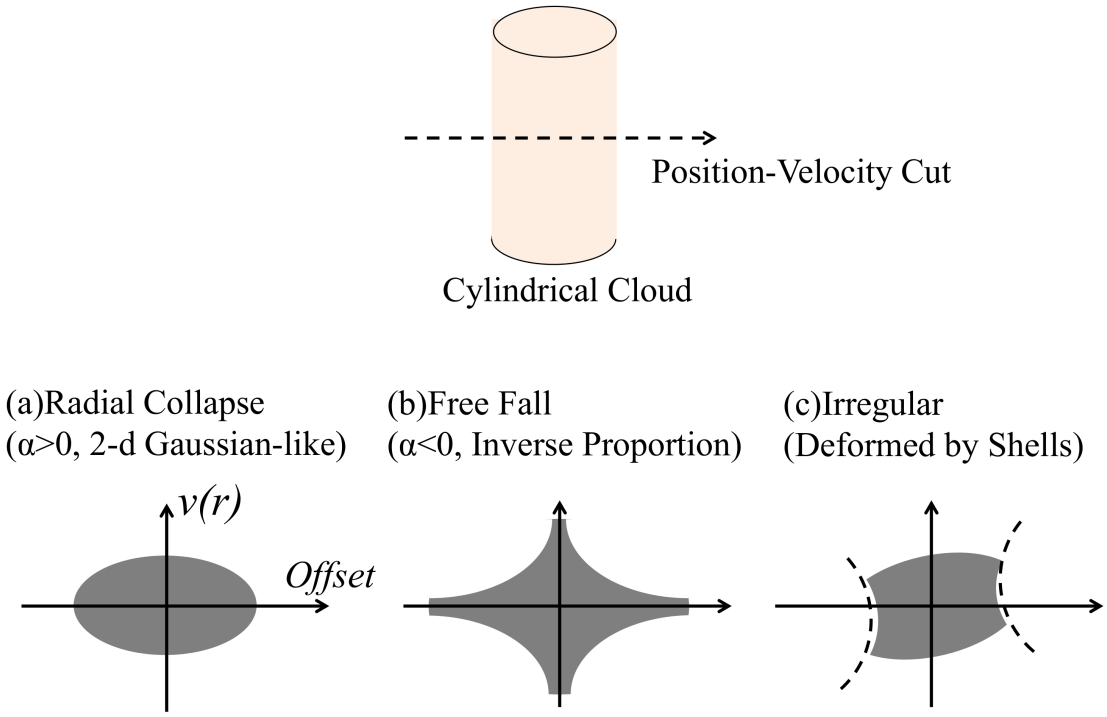

Figure 4.13: Schematic views of the P–V diagrams for a uniform density cylinder. α is a power of the radial infall velocity (Eq. (4.3.13)).

Chapter 5

Discussion

In this section, possible scenarios of the GMC formation in the N48 and N49 regions are constructed from the observational results. At first, several questions for the possible formation scenario are proposed, and then the justification of the scenario is done by estimating physical quantities from the observation and comparing them with theories.

5.1 Implication from the Observational Results

In order to construct the possible scenarios of the GMC formation, important implications from the previous observation should be reviewed at first. The high column density H I ridge is confirmed at the interface of the two SGSs LMC 4 and LMC 5 (Kim et al. 1999), and massive the GMCs whose total mass is up to 10^6 $M_\odot$ are found in the ridge (Mizuno et al. 2001, Yamaguchi et al. 2001a). Although the current expanding motions of LMC 4 and LMC 5 are still controversial (Kim et al. 1999, Book et al. 2008), their formation time scales and expanding velocities are estimated on the order of, or greater than, 10 Myr and 10 km s^{-1}. These values are matched well with the typical life time and the velocity width of the GMCs in the LMC (>10 Myr and <10 km s^{-1}; Kawamura et al. 2009, Fukui et al. 2008). The enhancement of the formation of the GMCs and the stellar clusters around the two shells are pointed out in many works (Yamaguchi et al. 2001a, Book et al. 2009, Dawson et al. 2013). Spatial coincidence of the shells and the GMCs at the ridge suggests that the GMCs are formed by the collision of the two shells.

With the high resolution ASTE ^{12}CO(J=3–2) observation (Fujii et al. 2014), it is revealed that the GMCs consist of a lot of molecular clumps with $\sim$ 10 pc diameter, $\sim$ 10^4 $M_\odot$ mass, and $\sim$ 10^3 cm^{-3} mean density. They show good spatial agreement with the H I in channel maps. Especially in the N48 region, the clumps are distributed in similar separation of $\sim$ 40 pc without prominent diffuse envelopes. One interesting trend is that the star formation and the physical properties of the clumps are more evolved in the N48 region, where the two SGSs are just interacting, than in the N49 region, which is located at the rim of only one SGS LMC 5. The interaction of the

two shell surely enhances the star formation activities. But the massive clusters are not formed yet, and the densities of the clumps are not as high as the massive cluster forming clumps, implying that the clumps in these regions are now just in the evolving, pre-cluster phase. The suggested star formation scenario for the N48 and N49 region is summarized inFujii et al. (2014): Dense, young, clumpy, star-forming molecular clumps are formed in the large-scale H I ridge accumulated by the two SGSs, LMC 4 and LMC 5. The densest molecular clumps ($\sim 2 \times 10^3$ cm^{-3}), in which the star formation is more advanced, are formed at the interaction zone of the two SGSs. The large-scale structure of the SGSs affects the formation of the young, star-forming molecular clumps; in particular the interaction of the two SGSs plays an important role and triggers the active formation of dense molecular clumps and massive stars.

In addition to these, several new facts are clarified from the new analysis of the H I gas. The averaged column density of the H I ridge is about 10^{22} cm^{-2}, and the opacity is actually high ($\tau > 1$) in the entire area. The high resolution ATCA+Parkes observation has revealed that the ridge consist of a composition of the filamentary features of the H I with 20 pc width. The molecular clumps are distributed along the prominent filamentary features. And the position velocity diagrams perpendicular to the ridge show axi-symmetrical, elliptical H I distribution at the interface of the two shells (the N48 region), indicating that the gravity plays an important role on the evolution of the current H I ridge.

Thus, the observational facts that are important for the GMC formation process are summarized as follows.

1. Massive GMCs with total mass of 10^6 M$_\odot$ are observed in the large, high column density H I ridge at the interface of the two SGSs.

2. The GMCs consist of the dense molecular clumps with 10 pc size, 10^4 M$_\odot$ mass, and 10^3 cm^{-3} density. They are distributed in the typical separation of $\sim$ 40pc.

3. The clumps are not as dense as cluster forming clumps, and the cluster formation is not started yet. Only several small H II regions and isolated core-collapse SNRs are observed.

4. The H I structure of the entire ridge is highly filamentary with 20 pc width. Their density is typically higher than ~ 10 cm^{-3} at the H I cores. The molecular clumps are typically associated with the prominent filamentary features.

5. The H I kinematics of the ridge implies that now the gravitational evolution seems to be important at the colliding area of the two shells.

The fact 1 to 3 are the results of the CO observations compared with the star formation activities. The fact 3 says that the drastic massive star cluster formation does not occur via the shell collision, unlike to the case of cloud-cloud collision. So the density of the cloud is not getting so high even after the collisional event. The fact 4 and 5 are the newly revealed results by the high resolution H I observation. The fact 4 implies

that the relatively dense (than ambient atomic medium) filamentary features are also formed outside the shell interacting zone, which may be formed by the single shock of the SGSs. And the fact 5 indicates that there is a sign of gravitational evolution of the ridge at the shell colliding area.

In order to suggesting a GMC formation scenario of this region from the observational facts, there are still several questions to be clarified.

- Can accumulation of the WNM by the expansion of the SGSs form the ridge, or several pre-existing molecular clouds are required?
- Are the GMCs, and the clumps gravitationally stable or not?
- Does the typical separation of the clumps corresponds to the Jeans length?
- How the local structure of the filamentary features affects the GMC formation process?
- Is there an additional evidence of the GMC evolution via the accretion of the H I?
- Are the typical time scales related to the GMC formation scenario consistent each other?

In the following sentions, justifications for these questions are performed, and the GMC formation scenario of the H I ridge will be constructed.

5.2 Discussion

5.2.1 The Formation of the Ridge by the SGSs

Dawson et al. (2015) have analyzed a GMC that is located at the stagnation point of two Galactic Supershells, GSH287+04−17 and Carina OB2 Supershell. By comparing the observational results with simulations and theoretical parameters, they have concluded that the GMC was partially seeded by pre-existing material denser than the WNM and assembled into its current form by the action of the two shells. This scenario is matched well with the theoretical predicts; several times shocks are required to form GMCs from the WNM (Inoue & Inutsuka 2008, Inutsuka et al. 2015). The total mass of the GMC is 1.7×10^5 $M_\odot$, and the sizes of the shells are 150×230 pc and 80×130 pc. These are roughly smaller by one order than the LMC N48 and N49 regions (mass $\sim 10^6$ $M_\odot$, shell size ~ 1 kpc). However, this is only one site in our Galaxy that the formation of the GMC via collision of Supershells has been discussed in the literature. And thus the same analysis should be done for the case of the LMC H I ridge, and the results should be compared.

Dawson et al. (2015) have estimated a mean initial number density for the pre-shell medium $\langle n_{\rm H} \rangle$, assuming simple sweep-up geometry. $\langle n_{\rm H} \rangle$ can be estimated by dividing the mass of the ridge $M_{\rm H_2}$ by the total volume of the sweep-up corns that consist of a base circle of the cloud and tops at the center of the shells. In their case, the mass and the diameter of the cloud are $M_{\rm H_2} = 1.2 \times 10^5$ $M_\odot$ and 90 pc, and the hight of the cones ($\sim$ the radius of the shells) are 80 and 100 pc. They have derived $\langle n_{\rm H} \rangle \sim 10$ cm^{-3}, which is denser than a canonical ambient atomic medium ($n \sim 1$ cm^{-3}), and they have concluded that the some pre-existing dense material was present prior to the formation of the GMC.

Here the estimation of the mean initial number density is applied to the LMC H I ridge. Note that in the case of the H I ridge, the mass of the H I gas cannot be ignored for the total mass. Taking the total H I mass of the ridge of 5×10^6 $M_\odot$ (the mass of $\sim$ 300pc length with optically thin approximation) into account, the total mass of the ridge M(H I + H_2) is $\sim 6.5 \times 10^6$ $M_\odot$. The area of the ridge as a base of the cones can be estimated by an elipse with semimajor and semiminer axis of 300 × 150 pc. With the radius of the SGSs of 700 pc (LMC 4) and 400 pc (LMC 5), $\langle n_{\rm H} \rangle \sim 4$ cm^{-3} is obtained. This initial density is denser than the ambient atomic medium of 1 cm^{-3} but rather diffuser than that of the study of out Galaxy (10 cm^{-3}). The average H I number density of the LMC is ~ 2 cm^{-3} (Kim et al. 2003), which is derived from the average H I column density of the entire LMC $\sim 3 \times 10^{21}$ cm^{-2}, and the typical H I scale hight of the LMC $\sim$ 180 pc (Kim et al. 1999). The estimated initial density is somewhat denser than the density of ambient atomic medium of the LMC. This is not so strange because not a few amount of the initial materials come from dispersed gas of GMCs that previously formed the stellar clusters inside the LMC 4. So the total mass of the ridge is sufficiently explained by the accumulated materials by both the SGSs. This result is different from what Dawson et al. (2015) have suggested; the GMC in the

H I ridge do not require the pre-existing denser material. This may be due to the large size scale. Since the total mass of the accumulated materials is quite large (>10^6 $M_\odot$), they are able to collapse into GMCs. Another suggestion here is that the kilo-parsec scale shells are required to form a massive GMC whose mass is up to $\sim 10^6$ $M_\odot$ from an ambient medium. The formation of the massive GMCs requires accumulation of the large amount of matters by the large-scale flows.

Note that total mass of the ridge is somewhat greater if the opacity corrected column density is used (Fig. 4.3). But in this case, the ambient density of entire the LMC is also underestimated almost by the same factor. So the effects of opacity is not so significant in the discussion here.

5.2.2 Gravitational Stability of the Clouds

Dawson et al. (2015) have also discussed the dominant confining pressure of the GMC between GSH287+04−17 and Carina OB2 Supershell. They argued the gravitational stability of the GMC by estimating the viral state of the cloud. Virial mass of the GMC is $M_{\rm vir}(^{12}{\rm CO}) = 1040\, R\sigma_v^2 \sim 5.6 \times 10^5$ $M_\odot$ with radius $R = 35$ pc, and velocity dispersion $\sigma_{\rm cld} = 3.7$ km s^{-1}. And the luminosity-based mass is $M_{\rm lum}(^{12}{\rm CO}) \sim 2.3 \times 10^5$ $M_\odot$, so the virial parameter of the GMC is $\alpha = 5\sigma^2 R/GM_{\rm lum} = 1.12 \times M_{\rm vir}/M_{\rm lum} \sim 2.7$, which is apparently higher than unity. In the case of the ^{13}CO line, $M_{\rm vir}(^{13}{\rm CO}) \sim 3.1 \times 10^5$ $M_\odot$ and $M_{\rm lum}(^{13}{\rm CO}) \sim 3.7 \times 10^4$ $M_\odot$ so the virial parameter is greater than the ^{12}CO case, $\alpha \sim 8.4$. So the GMC is therefore not globally self-gravitating under the standard virial treatment, and some external pressure is required to confine the GMC.

The surface pressure just required to confine a spherical cloud, with the inclusion of a surface pressure term in the virial theorem, can be obtained as

$$P_S = \frac{1}{4\pi R^3}\left(3M\sigma_v^2 - \frac{3}{5}\frac{GM^2}{R}\right). \tag{5.2.1}$$

For the assumed properties of the GMC, $P_S \gtrsim 7 \times 10^{-12}$ g cm^{-1} s^{-2} is obtained to confine the current state of the GMC. They have argued that ram pressure ρv^2 from the colliding flows provides a candidate for an external confining pressure. Warm gas in the collision zone typically has densities of 1–10 cm^{-3} and velocities of 20–40 km s^{-1} from each side, in the model shells. So ram pressure is between $\sim 7 \times 10^{-12}$ and 3×10^{-10} g cm^{-1} s^{-2}, which is more than sufficient to confine the GMC.

In the case of the GMCs in the LMC H I ridge, the situation is somewhat different. Given the total radius of the GMC $R = 50$ pc and the velocity width $dV = 11.5$ km s^{-1}, the virial mass of the GMC is $M_{\rm vir}(^{12}{\rm CO}) \sim 1.3 \times 10^6$ $M_\odot$. The luminosity-based mass is $M_{\rm lum}(^{12}{\rm CO}) \sim 1.5 \times 10^6$ $M_\odot$, then the virial parameter of the GMC in the ridge is $\alpha \sim 0.97$, indicating that the gravity is sufficient to confine the GMCs. Note that the luminosity-based mass $M_{\rm lum}(^{12}{\rm CO})$ is derived from $X_{\rm CO}$ factor that is estimated from the luminosity to virial mass relation of the LMC GMCs with assumption of they are

in the virial equilibrium (Fukui et al. 2008), so this argument is rather meaning less. But here it is confirmed that the virial parameter of the GMCs in the N48 and N49 regions are not quite different from unity, indicating that the GMC is quite common state of the GMCs in the LMC, i.e., it can be said that the GMC is roughly in the virial equilibrium. The surface pressure P_S is negative for these GMC parameters. Therefore, no external pressure other than gravity is necessary to the GMC confinement.

The GMC consists of the dense molecular clumps. The fact that the GMC as a whole is close to virial equilibrium indicates that the velocity dispersion between the clumps are confined by the gravity of the GMC. This indicates that the clumps are not formed separately in turbulent medium. As seen in section 3.1.1, the virial parameters of the ^{12}CO(J=3–2) clumps are also close to virial equilibrium, in average $\alpha \sim 1.3$ (or greater if lower $X_{\rm CO}$ value is adopted). This implies the clumps roughly in gravitational equilibrium, indicating that the clumps are in the pre-cluster phase. Note that each clumps also consists of sub-structures of dense cores and/or filaments as seen in high resolution observation of the LMC clumps (Seale et al. 2012, Fukui et al. 2015a). Even the clump itself is close to virial equilibrium, some of the substructures can collapse to form stars. Actually several Spitzer YSO candidates are found in the clumps (Figure 3.1). Since the cluster formation requires further compressive event such as cloud-cloud collision, this might be the typical state of the pre-cluster phase.

5.2.3 Jeans Analysis

One famous theoretical parameter associated with the wavelength of the instability is Jeans length. If the GMCs in the ridge is formed via the shell-induced instability, the characteristic $\sim$ 40 pc separation of the molecular clumps (§3.1.1) should be explained by the Jeans length. With an assumption of an infinite and homogenous medium, the Jeans length is

$$\lambda_{\rm J,therm} = \sqrt{\frac{\pi c_{\rm S}^2}{G\rho}}. \tag{5.2.2}$$

This is a common expression of the thermal Jeans length. The Jeans length corresponds to the critical size scale of the unstable gas cloud. That is, the clumps that is formed from the shell-induced instability, the length scale of their separation should be $\sim \lambda_{\rm J,therm}$ with certain initial parameters. Another expression of the Jeans length can be obtained by substituting the thermal sound speed by a velocity dispersion of turbulence,

$$\lambda_{\rm J,turb} = \sqrt{\frac{\pi \sigma_{\rm turb}^2}{G\rho}}. \tag{5.2.3}$$

$\lambda_{\rm J,turb}$ is called as turbulent Jeans length since its expresses the unstable size scale of a medium with supersonic turbulence. These two Jeans lengths give different estimations for the fragmentation length of the medium, and it is still controversial which value should be adopted: Although the turbulence is considered to be important for the

formation of molecular clouds and the molecular clouds are typically in state of a super sonic turbulence, the classical thermal Jeans length is still applicable to explain the fragmentation size scale even in recent high-resolution observational works (e.g., Takahashi et al. 2013, Beuther et al. 2015). It is also argued that the turbulence is dominant in very local scale (< 1 pc) where the cores are so dense that their mass cannot be explained by the thermal Jeans mass (e.g., Wang et al. 2014). In this work, both expressions are used to test that the clump separation can be explained by the Jeans length or not. To derive the typical Jeans length of the ridge, pre-collapse density of the medium and the thermal sound speed (or the turbulent velocity dispersion) should be estimated.

One notification here is that the entire H I ridge is almost virialized, so there is no problem with considering the instability of the entire system here. Assuming the main part of the ridge can be regarded as a sphere with ~ 100 pc radius, the virial mass of the ridge is $\sim 8{\times}10^6$ $M_\odot$ (given the FWHM velocity width of 20 km s^{-1}). Although the total mass of the H I gas in the corresponding area is only $\sim 3{\times}10^6$ $M_\odot$, the total mass of the ridge including molecular mass (H I+H_2) is $\sim 5{\times}10^6$ $M_\odot$ with upper limit of $\sim 8{\times}10^6$ $M_\odot$ (opacity corrected value). This is slightly lower but quite comparable to the virial mass of the ridge. Considering the typical H I cloud is highly non-virialized (e.g., Kim et al. 2007), it can be said that the entire H I ridge is almost virialized.

The initial density of the pre-collapse ridge can be estimated from theoretical models. Here the ridge is considered to be formed by the accumulation of the ambient diffuse medium by the two SGSs and the collision of the two shells. In this consideration, there are two shock compression processes; the one is induced by a shock of an expanding shell, and the other one is driven by a collision of two shells. For the expanding shell case, density enhancement is not only induced by the shock compression, but also by the isobaric contraction of shocked cold medium with strengthening interstellar magnetized fields (Inoue & Inutsuka 2009). Resulting density is given by

$$\langle n_{\rm sh} \rangle \sim n_1 \frac{\rho_0 v_{\rm sh}^2}{B_{\perp 1}^2/8\pi}, \tag{5.2.4}$$

where n_1 is post-shock number density (immediately behind the shock front), ρ_0 is pre-shock density, $v_{\rm sh}$ is shell expansion velocity, and $B_{\perp,1}$ is magnetic field in the post-shock medium (see Eq.(16) of Inoue & Inutsuka 2009). This Equation means that the mean density enhancement due to the isobaric contraction of the shocked gas is stopped when the ram pressure of the shell flows and the magnetic pressure in the shell are balanced. For the collision of shells, density enhancement can be estimated from the model of the collision of two clouds Inoue & Fukui 2013. According to the shock jump condition for the isothermal MHD shock, the density is

$$n_{\rm sh,col} \sim \sqrt{2}\mathcal{M}_A n_{\rm sh}, \tag{5.2.5}$$

where $\mathcal{M}_A$ is Alfvénic Mach number of the pre-collision medium. $\mathcal{M}_A$ is given by $v_{\rm sh}/v_A$, where $v_A = B_{\perp,1}/\sqrt{4\pi\rho_{\rm sh}}$ is Alfvénic velocity of the pre-collision medium. The

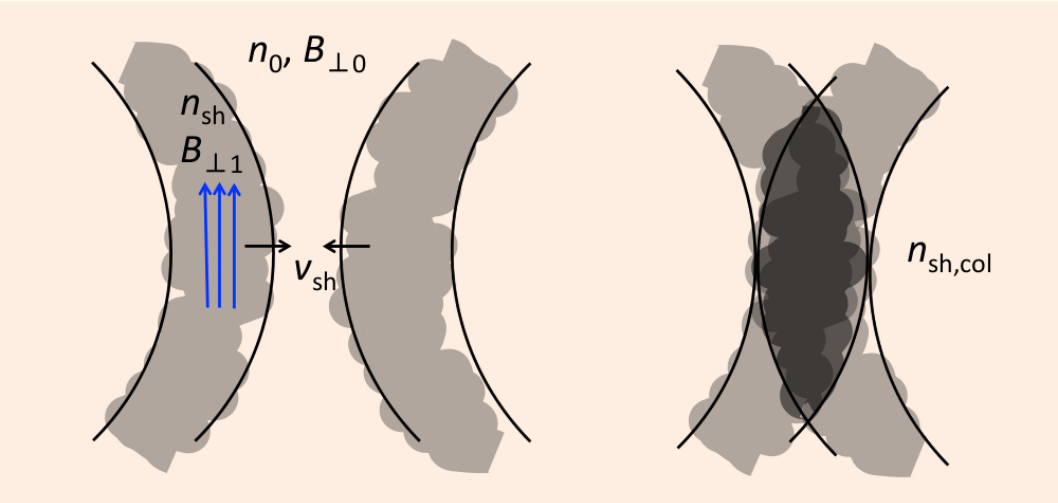

Figure 5.1: Schematic view of the shock compression by the shells and by the collision of the shells.

density increase in Equation (5.2.5) is much smaller than the case without the effect of the magnetic field, where the compression ratio is $\mathcal{M}_S^2$, which is two order of magnitude greater than $\sqrt{2}\mathcal{M}_A$ for a typical molecular cloud. This means that the magnetic field prevents the rapid collapse of the couds and keeps the Jeans mass effectively high during the compression.

The density of the atomic medium just after the collision can be estimated from the density of the ambient atomic medium using these two equations. At first, the initial ambient atomic medium of this area is estimated as 4 cm^{-3} in previous subsection. It is a little bit denser than the typical density of 1 cm^{-3}, so the ambient atomic medium density of $n_0 \sim$ 1–4 cm^{-3} is adopted here. From Equation (5.2.4), the ambient medium compressed by a sigle shell increases its density by 10, since the density increase by the shock compression is factor of a few (up to 4 for the large Mach number limit of Rankine-Hugoniot relation), and that by the isobaric contraction is factor of a few for typical interstellar magnetic field ($\sim$ a few μG). And from Equation (5.2.5), the collision of the shells compresses the shell-shocked medium by a factor of 3, with shell expanding velocity of $\sim$ 10 km s^{-1} and Alfvénic velocity of $\sim$ 5 km s^{-1} (assuming the $B_{\perp,1} \sim 10$ μG). Thus the final density $n_{\rm sh,col} \sim$ 30–120 cm^{-3} is achieved. The free fall time of H I (Eq. (1.1.26)) medium with density range of $\sim$ 30–120 cm^{-3} is $\sim$ 4–8 Myr, which are quite consistent with the typical formation time scale of the GMC formation of $\sim$ 10 Myr. Note that this corresponds to the density of the most effectively compressed medium by the shocks of the shells and the collision.

Consistency between these theoretically estimated density and the observed density should be confirmed. Average number density of the ridge that is derived by dividing the average column density $\sim 10^{22}$ cm^{-2} (opacity corrected value, see Fig. 4.3) by the typical width of the ridge (that may be similar to the depth of the ridge) 100 pc is $\sim$ 30 cm^{-3}. Total H I mass of the ridge with the final density of $n_{\rm sh,col} \sim$ 30–120 cm^{-3} is 8–32 $\times$ 10^6 M$_\odot$ when the size of the ridge can be expressed as a cylinder with a base diameter of 150 pc and a hight of 600 pc. Observed total mass of opacity corrected column density map (Fig. 4.3), which gives the most optimistic mass of the ridge including the GMCs, is $\sim 1 \times 10^7$ M$_\odot$, so the estimated final density $n_{\rm sh,col}$ gives rather high total mass than observed value. So, the lower end of the $n_{\rm sh,col}$ seems to be reliable as the averaged density of pre-collapse ridge, and the higher end is only applicable when more localized area of the ridge is considered.

Using the resulting density range, the Jeans length of the atomic medium is derived by Equation (5.2.2) and (5.2.3), and the Jeans mass $M_{\rm J}$ is derived from the Jeans length

$$M_{\rm J} = \frac{4}{3}\pi \left(\frac{\lambda_{\rm J}}{2}\right)^3 \mu\, m_{\rm H\,I}\, n_{\rm H\,I}, \tag{5.2.6}$$

where μ is a mean molecular weight (for atomic medium $\mu \sim$1.3 including the weight of Helium), and $m_{\rm HI}$ is a weigh of the atomic Hydrogen ($\sim 1.67 \times 10^{-27}$ kg). Since the estimation of an actual value of a sound speed and a turbulent velocity dispersion involves large errors of a several factor, several conditions should be considered. Table

5.2 shows the parameters and calculated results of the thermal and turbulent Jeans lengths for 9 cases, which is a combination of 3 possible values of the density and the velocity. Considered densities are 30, 60, and 120 $\mathrm{cm^{-3}}$, that are within the range derived above. Considered spin temperatrues of the H I to derive sound speed are 50, 100, and 200 K. The H I spin temperatrue of the ridge is roughly estimated as 100 K (Fig. 4.3), and colder and warmer case are considered. Sound speed c_S is derived by

$$c_\mathrm{S} = \sqrt{\frac{\kappa R T_\mathrm{spin}}{\mu}}, \tag{5.2.7}$$

where κ is the ratio of the specific heat (= 5/3 for atomic medium), R is the gas constant (=8314.4598 [$\mathrm{m^2\ g\ s^{-2}\ K^{-1}\ mol^{-1}}$]), and μ is a mean molecular weight of the atomic medium ($\sim$ 1.3). Considered turbulent velocity dispersions are 2.0, 3.0, 5.0 km $\mathrm{s^{-1}}$. σ_v should be given by a turbulent velocity dispersion of the cold medium. There are several ways to estimate it. First, it is given from a typical velocity dispersion of the molecular clumps. The typical velocity width of the molecular clumps in the N48 and N49 regions is 4.3 km $\mathrm{s^{-1}}$ (Table 3.1), which corresponds to the velocity dispersion of $\sim$ 2.0 km $\mathrm{s^{-1}}$. The second way is using velocity dispersion of the GMC, which is equivalent to the velocity dispersion of typical CNM. From the NANTEN observation (Fukui et al. 2008), the velocity width of the GMC is 11.5 km $\mathrm{s^{-1}}$, which corresponds to the velocity dispersion of $\sim$ 5.0 km $\mathrm{s^{-1}}$. And finally, it can be estimated from theoretical works. From a MHD simulation of a converging flows, the typical velocity dispersion at the compressed layer is expected to be 3.0 km $\mathrm{s^{-1}}$ (Inoue & Inutsuka 2012).

$\lambda_\mathrm{J,therm}$ and $\lambda_\mathrm{J,thurb}$ distribute in a wide range from 10 pc to 140 pc, but this is within a range of a factor of 2 to 3 from the clump separation (30–50 pc, §3.1.1). For thermal case, the derived Jeans lengths are typically shorter than the clump separation, indicating that all case is acceptable to explain the separation in a rough sense. Case 2 and 3 is only one that gives close value to the separation, $\lambda_\mathrm{J,therm}$ = 27–41 pc with n_HI = 30 $\mathrm{cm^{-3}}$ and T_spin = 100–200 K. n_HI = 30 $\mathrm{cm^{-3}}$ is the most reasonable estimate for the pre-collapse density of the ridge. T_spin = 100-200 K corresponds to warmer end of the estimated in the ridge (Fig. 4.3), and lower end of that is roughly estimated for entire the LMC (150–600 K; Fukui et al. 2009). So the temperature range is also reasonable for the pre-collapse medium. $\lambda_\mathrm{J,therm}$ in the case 2 and 3 also give a reasonable Jeans mass of 1.0 and 3.5 $\times 10^4$ $\mathrm{M_\odot}$, that is comparable to the observed mass of the clumps $\sim$ 2 $\times 10^4$ $\mathrm{M_\odot}$.

For turbulent Jeans length, $\lambda_\mathrm{J,turb}$ is typically longer than the clump separation, indicating that the turbulent velocity seems to be large to explain the separation. However, $\lambda_\mathrm{J,turb}$ is close to the separation of $\sim$ 40 pc in the case 4, 7, and 8. Case 4 is $\lambda_\mathrm{J,turb}$ = 39 pc with n_HI = 60 $\mathrm{cm^{-3}}$ and σ_v = 2.0 km $\mathrm{s^{-1}}$. Case 7 and 8 is $\lambda_\mathrm{J,turb}$ = 27–41 pc with n_HI = 120 $\mathrm{cm^{-3}}$ and σ_v = 2.0–3.0 km $\mathrm{s^{-1}}$. As mentioned before, the densities of 60 and 120 $\mathrm{cm^{-3}}$ are either rather high for the average density for the entire ridge. If the turbulent fragmentation plays important role for the formation of the molecular

clumps, it should be occur in more localized scale (< 100 pc). This agrees with the required turbulent velocity is close to the velocity dispersion of molecular clumps, not of the GMCs or the H I medium. It is also consistent with the fact that the clumps seem to be distributed in a typical separation $\sim$ 40 pc but the actual separation values take some distribution from 30 to 50 pc, that is, it is also possible that the entire clouds are formed by the composition of several local scale instabilities. The Jeans masses for the turbulent case, however, are higher than the observed quantity by a factor of few. Considering the equation of the Jeans mass just means the total mass of the gas within a sphere with a diameter of the Jeans length, and the observed molecular gas is just the central portions of the unstable gas, so it is not strange that the current molecular mass is smaller than the Jeans mass. Typical free fall time of H medium of 60–120 cm^{-3} is $\sim$ 5 Myr, so this is sufficiently possible.

In both the thermal and the turbulent case, the clump separation can be explained by the Jeans length within the reasonable parameter range. The classical thermal Jeans analysis gives the separation and mass that show the better agreement with observed quantities with the most reasonable density and temperature. The turbulent Jeans analysis also gives the good separation and the mass with several constraints on the physical conditions (but these constraints are also in a reasonable range). Therefore, it can be said that the scenario of the GMCs formation via shell-induced, large-scale instability agrees well with the Jeans analysis. One notification on these results is that this analysis do not give a limitation on the parameters, but just means that the characteristic clump separation "can be" the result of the fragmentation.

5.2.4 Fragmentation of the Filamentary Features

In a local scale, the H I structure of the H I ridge is dominated by the filamentary features with 20 pc width (§4.2.2). The molecular clumps are found along the prominent filamentary feature, so the this filamentary nature of the H I should be important for the formation process of the molecular clumps. Thus, the fragmentation of such filamentary features should also be considered for the GMCs formation via gravitational collapse. A characteristic isothermal scale-height H of a gas cylinder within a hydrostatic equilibrium is given by

$$H = \frac{c_{\mathrm{S}}}{\sqrt{4\pi G\rho}}, \tag{5.2.8}$$

where c_{S} is the sound speed, G is the gravitational constant, and ρ is the gas mass density at the center of the filament (e.g., Nagasawa 1987). In this expression, the scale-height H is equal to $\lambda_{\mathrm{J,therm}}/2\pi$. The width of the cylinder is $2H = \lambda_{\mathrm{J,therm}}/\pi$. The characteristic fragmentation scale of a self gravitating cylinder is expected with separation of 4 times of the cylinder diameter (Inutsuka & Miyama 1992), i,e, the fragmentation wavelength is

$$\lambda_{\mathrm{frag}} = 8H. \tag{5.2.9}$$

Table 5.2 shows the results of the isothermal width and the fragment wavelength for 9 cases, that is similar to the discussion in the previous subsection. Only the range of density is different, diffuser case (10 cm^{-3}) is adopted instead of middle density case (60 cm^{-3}). It is intersting that the cases with density of 10 cm^{-3} and 100 to 200 temperature (case 2 and 3) give the width of $\sim$ 15–22 pc, which is a good agreement with the observed width of the filamentary features with similar density and temperature. This indicates that the filamentary features are in a state close to a hydrostatic equilibrium. The fragmentation wavelength is just $4/\pi$ times the value of the thermal Jeans length. So it is notable that the physical condition that gives the closest length to the clump separation is similar to the Jeans length case, $n_{\rm HI} = 30$ cm^{-3} and $T_{\rm spin} =$ 100–200 K. In this condition, the width of the filament is $\sim$ 10 pc. This width is tighter than the observed filamentary features, but is good agreement with the typical size of the molecular clumps. This indicates that the filamentary features need to be tightened from the current width to form molecular clumps. But if the case is true, the molecular clumps are formed through fragmentation along the filament with almost no radial contraction. This may be possible if magnetic field along the filament is more prominent than that of the radial direction (e.g., Nakamura et al. 1993). Since the ridge experiences at least two times of shock compressions, magnetic field along the ridge is effectively enhanced with the gas compression (Inoue & Inutsuka 2008, 2009), the collapse speed of the fragment of a filament can be faster in the direction along the filament. However, the actual case seems to be more complicated because the filamentary feature around the clumps looks broader than 10 pc with significantly compositing and/or blending each other with other components. Anyway, the separation of the clumps also can be explained by the axial fragmentation of filamentary features with reasonable density and temperature conditions.

5.2.5 Accretion of the H I

The position velocity diagrams of the H I ridge also suggests the possibility of H I accretion on the GMCs at the shell colliding area. Since whether the H I envelopes are gravitationally bound to the GMCs or not is quite contraversive, checking the effects of accretion of H I on the GMCs evolution is still necessary to clarify this question.

In some theoretical works, self-gravity of the whole molecular cloud is regarded to not significantly affect the cloud growth. This is partly because the mass function should be steeper if the molecular clouds evolve with mass accretion (Inutsuka et al. (2015)). In a simulation of GMC formation via colliding flow, the mass of the cloud is accumulated by the flows and the cloud is formed via thermal instability, without any effects of gravity (e.g., Inoue & Inutsuka 2008). On the other hand, Fukui et al. (2009) have argued from the LMC observation that the GMCs are evolving within the gravitationally bound H I envelopes of the GMCs according to their star formation activity. The H I flows to the GMCs are considered to be a supplier of the supersonic turbulence of the clouds (e.g, Inoue & Inutsuka 2012).

Fukui et al. (2009) have estimated the mass accretion rate of the H I to the GMCs.

Table 5.1: Jeans Length

Case No.	1	2	3	4	5	6	7	8	9
Thermal Jeans Length									
$n_{\rm HI}$ [cm^{-3}]	30	30	30	60	60	60	120	120	120
$T_{\rm spin}$ [K]	50	100	200	50	100	200	50	100	200
$c_{\rm S}$ [km/s]	0.73	1	1.5	0.73	1	1.5	0.73	1	1.5
$\lambda_{\rm J,therm}$ [pc]	20	27	41	14	19	29	10	14	21
$M_{\rm J,therm}$ [$10^4\times$ M $_\odot$]	0.41	1	3.5	0.28	0.7	2.5	0.2	0.56	1.9
Turbulent Jeans Length									
$n_{\rm HI}$ [cm^{-3}]	30	30	30	60	60	60	120	120	120
$\sigma_{\rm v}$ [km/s]	2.0	3.0	5.0	2.0	3.0	5.0	2.0	3.0	5.0
$\lambda_{\rm J,turb}$ [pc]	55	82	140	39	58	97	27	41	69
$M_{\rm J,turb}$ [$10^4\times$ M $_\odot$]	8.5	28	140	6	20	93	4	14	67

Estimated Jeans lengths and Jeans masses for 9 possible cases.

Table 5.2: Isothermal Filament Fragmentation Length

Case No.	1	2	3	4	5	6	7	8	9
Parameters of the Isothermal Cylinder									
$n_{\rm HI}$ [cm^{-3}]	10	10	10	30	30	30	120	120	120
$T_{\rm spin}$ [K]	50	100	200	50	100	200	50	100	200
$c_{\rm S}$ [km/s]	0.73	1	1.5	0.73	1	1.5	0.73	1	1.5
$\lambda_{\rm J,therm}$ [pc]	35	48	71	20	27	41	10	14	21
H [pc] (=half width)	5.6	7.6	11	3.2	4.3	6.5	1.6	2.2	3.3
$\lambda_{\rm frag}$ [pc] ($= 8H$)	45	61	88	26	34	52	13	18	26

Theoretical parameters of an isothermal cylinder given by Equations (5.2.8) and (5.2.9) for 9 possible cases.

The infall velocity of the H I is roughly estimated to be half of the H I line width, $\sim$ 7 km s^{-1}. Since this is nearly equal to $\sqrt{GM/R} \sim 6$ km s^{-1} for $M = 2 \times 10^5$ M$_\odot$ and $R = 40$ pc GMCs, the H I envelope can be considered to be gravitationally bound to the GMCs. In the case of the H I envelope with a radius of $\sim$ 40 pc and volume density of $\sim$ 10 cm^{-3} spherical accretes to the GMC with this infall velocity, the mass accretion rate is $\sim$ 0.05 M$_\odot$ yr^{-1}. This corresponds to the increase in molecular mass amounts of 5×10^5 M$_\odot$ in 10 Myr, which is consistent with the observed typical mass of a cluster forming GMC ($\sim 4 \times 10^5$ M$_\odot$).

For the GMCs in the H I ridge, the H I accretion is indicated in the position velocity diagrams. The total mass of the H I ridge as the envelope of the GMCs is $\sim 5 \times 10^6$ M$_\odot$ ($\sim 2 \times 10^6$ M$_\odot$ even focus on the area just around the GMCs), which is sufficient reserver for the mass accretion to the GMCs with $\sim 10^6$ M$_\odot$ mass (note that the total mass is up to $\sim 10 \times 10^6$ M$_\odot$ with opacity corrected data). The H I mass accretion rate, that is estimated in the same way as Fukui et al. (2009), of the ridge is $\sim$ 0.2 M$_\odot$ yr^{-1} with the infall velocity of H I $\sim$ 10 km s^{-1} (half of the typical line width), the radius of the H I envelope $\sim$ 50 pc (radius of the GMCs), and volume density of $\sim$ 30 cm^{-3}. This corresponds to 2×10^6 M$_\odot$ for 10 Myr, which is clearly consistent with the current mass of the GMCs. The same calculation is also applicable to the molecular clumps. The H I envelope of the molecular clumps should be the filamentary features. The infall velocity of this H I envelope is roughly given as $\sim$ 5 km s^{-1}, which is the half of the typical linewidth of the filamentary features. Given the radius of the H I envelope $\sim$ 5 pc (radius of the molecular clumps), and the volume density of $\sim$ 30 cm^{-3}, the H I mass accretion rate to the clumps is $\sim 1 \times 10^{-3}$ M$_\odot$ yr^{-1}, corresponding to the mass of $\sim 10^4$ M$_\odot$ in 10 Myr. This is also consistent with the current mass of the molecular clumps.

One important fact of this analysis is that in the optimistic estimate for the infall velocity (almost free fall), the total accreted mass in 10 Myr only corresponds to the current mass of the GMC and the clumps. This suggests that the H I accretion seems to be non-negligible even in the clump-scale once the GMCs are formed. This is not a decisive evidence of the scenario that the GMC is evolving by the H I accretion from the first step, however it can be said from the analysis that the H I envelopes of the GMCs and the molecular clumps are gravitationally bound to them.

5.2.6 Time Scale Consistency

As mentioned in the introduction section (§1.3.1), the formation timescales of the SGSs are on the order of 10 Myr from the age estimates based on the stellar population (e.g., Glatt et al. 2010), which includes the assumption that the SGSs are formed by several generations of star formation. The ages of 10–20 Myr for the two SGSs LMC 4 and LMC 5 are adopted here, with a particularly strong constraint of >15 Myr implied for LMC 4 since there is an extended stellar arc ($\sim$ 600 pc) in Constellation 3 (Efremov & Elmegreen 1998).

Typical timescales for the formation of GMCs from diffuse H I gas have been roughly

estimated as $\sim$ 10 Myr in the LMC (Fukui et al. 2009), which corresponds to a crossing time of a typical GMC of $\sim$ 100 pc size assuming a typical H I velocity dispersion of $\sim$ 10 km s^{-1} (Fukui & Kawamura 2010). The crossing time is supported to be a reasonable measure of the actual lifetime of the cloud by a theoretical work (Dobbs & Pringle 2013). The free-fall time of H I gas whose density is $\sim$ 10 cm^{-3} is also $\sim$ 10 Myr.

Current expanding velocities of the two SGSs are roughly estimated to $\sim$ 30–40 km s^{-1} from the dynamics of the H I gas (Kim et al. 1999, Book et al. 2008), but the accurate velocity is still controversial. The width of the ridge is $\sim$ 200 pc, so the ridge crossing time of the SGSs is $\sim$ 5–7 Myr for these velocities, which is rather short comparing to the formation timescale and the lifetime of the GMCs. However, this velocity is estimated by seeing approaching and receding components near the central part of the shells, so this is the expansion velocity of the direction perpendicular to the ridge. Since the density of ambient gas is getting lower according to the height from the disk getting higher, the expansion of a shell is faster toward the direction perpendicular to the disk than that parallel to the disk. This indicates that the collision velocity might be slower, around $\sim$ 10 km s^{-1}. This gives the ridge crossing time of the SGS of $\sim$ 20 Myr, which is sufficiently comparable timescale with the formation timescale and the lifetime of the GMCs. This is also consistent with the observed line width of the GMCs, ΔV = 11.5 km s^{-1}, implying that the GMC formation is involved in the collisional events with $\sim$ 10 km s^{-1}.

There are several signatures of OB stars in the N48 and N49 regions. Actually, the H II region N48 is an extensive young OB association NGC1948, which consists of two OB associations, LH 52 and LH 53 (Lucke & Hodge 1970). Age spread of the association is estimated to 5-10 Myr (Vallenari et al. 1993, Will et al. 1996). The parental molecular clouds of the association seems to be dispersed away (Fig. 3.1(d)). The most luminous source of the association is IRAS 05257-6617 whose bolometric luminosity is $\sim$ 3.4 $\times 10^5$ L$_\odot$, implies an O6V star with $\sim$ 30 M$_\odot$ (Cohen et al. 2003). This corresponds to a main sequence life of 6 Myr (Meynet & Maeder 2000). How the OB stars in the association including such a quite massive star are formed besides the pre-cluster phase molecular clumps? One possibility is a cloud-cloud collision. In the previous work, the offset of the H II regions from the molecular clumps is understood as the age gradient induced by the shell expansion (Yamaguchi et al. 2001a). Since the timescale of massive star formation via cloud-cloud collision is quite short ($\sim 10^5$ yr, Fukui et al. 2015b), the age gradient also can be explained by this process. In the LMC, sub-parsec resolution observation of ALMA has revealed that the high mass young star of $\sim$ 37 M$_\odot$ is formed within a 10^5 yr at the intersection of two filaments, indicating massive star formation via filament collision (Fukui et al. 2015a). If the ridge is actually formed by the collision of the two SGSs, it is highly probable that the small dense clouds or filaments formed in the expanding shells are colliding each other at the stagnation point of the collision. This is just a speculation and further analysis is necessary, but there seems to be almost no chance to prove this hypothesis since the H II regions are highly evolved and the parental clouds are dispersed away.

5.3 Summary of the GMC Formation Scenario

5.3.1 The GMC Formation Scenario at the Ridge

The answers for the questions that are suggested above to probe the GMC formation scenario at the H I ridge are as follows.

- *Can accumulation of the WNM by the expansion of the SGSs form the ridge, or several pre-existing molecular clouds are required?*
  – Yes, the total mass of the ridge can be supplied by the accumulation of the ambient medium. The initial density should be a few cm^{-3}, but it does not mean the requirements of pre-existing dense materials like molecular clouds. This also indicates that the kilo-parsec scale accumulation flows are required to form the GMC with mass up to 10^6 $M_\odot$ from the ambient medium.

- *Are the GMC and the clumps gravitationally stable or not?*
  – The GMC is roughly in the gravitational equilibrium, so the entire system of the GMC with sub-structures of the clumps is gravitationally bound. This indicates that the clumps are not formed separately in the turbulent medium. The clumps are also roughly in the gravitational equilibrium, implying that the further collapse to the cluster formation is restrained by the turbulence.

- *Does the typical separation of the clumps corresponds to the Jeans length?*
  – The separation and the mass of the N48 clumps can be explained by the Jeans length and the Jeans mass with reasonable densities and temperatures (or turbulent velocities). This indicates the clumps are formed in a large-scale instability induced by the shells.

- *How the local structure of the filamentary features affects the GMC formation process?* – The molecular clumps are found along the prominent filamentary feature, which indicates that the filamentary H I might plays an important role on the formation of the molecular clumps. The separation of the N48 clumps also can be explained by the fragmentation of the filamentary features of $\sim$ 30 cm^{-3} density and $\sim$ 10 pc width. The H I filamentary features are required to be evolved in order to form the molecular clumps.

- *Is there an additional evidence of the GMC evolution via the accretion of the H I?*
  – In the optimistic estimation of the H I mass accretion rate to the GMC, the H I mass accretion rate is $\sim$ 0.2 $M_\odot$ yr^{-1}, corresponds to the total mass of the GMCs in 10 Myr. The same result is achieved for the H I mass accretion rate of the molecular clumps. It implies that the H I accretion is now non-negligible and the H I envelopes are gravitationally bound to the GMCs and the clumps.

- *Are the typical time scales related to the GMC formation scenario consistent each other?*

– Yes, all time scales related to the GMC formation and the SGS kinematics can be explained in $\sim$ 10 Myr, which is consistent with commonly accepted timescale of the GMC formation.

Considering these facts, the scenario of the GMC formation process at the ridge can be constructed in a large-scale and a high-resolution scale. At first in the large scale ($>$ 100 pc scale), the expansion and the collision just aggregates the diffuse atomic medium with density of a few cm^{-3} into large-scale, high column density ridge that mainly consists of the shocked CNM with density of several tens of cm^{-3}. Secondly, the ridge collapses into the GMCs consists of a lot of molecular clumps. The clumps are typically 10^4 M$_\odot$ and 10^3 cm^{-3}, and are roughly in a virial equilibrium (further collapse is restrained by a turbulence). And in the current phase, the H I gas around the GMCs is gravitationally bound to the GMCs, and the GMCs are evolving by its accretion until the cluster formation starts via further gravitational collapse, or collision with other clouds. On the other hand in the high-resolution scale ($<$ 10 pc resolution), the structure of the H I gas is getting highly filamentary during its evolution. The formation of the molecular clumps is taken place along the evolved filamentary H I gas. The H I gas around the molecular clumps are also getting to be bound to the clumps, and the H I accretion onto the clumps are now non-negligible. The formation scenarios in the both size scale proceed simultaneously and just see the different spatial resolution. These agrees well with the theoretical predicts insisting that several times shocks are required to form GMCs, and newly suggests that the GMC formation involves filamentary nature of the atomic medium.

5.3.2 Speculation to the General GMC Formation Process

One of the important results of this work is that the H I gas is highly filamentary and the molecular clumps are formed in the evolved filamentary H I gas. Since the filamentary H I features are quite crowded in the H I ridge, merger of the filamentary features induced by the shell collision may play an important role on their evolution. In the LMC N159W region, sub-parsec resolution observation of ALMA has revealed that the high mass young star is formed at the intersection of two filamentary molecular clouds (Fukui et al. 2015c). If the molecular clumps are formed at the merging filaments, this gives the hierarchical view of the evolution of the ISM; a collision of filamentary H I clouds forms molecular clouds, and a collision of filamentary molecular clouds form massive stars. To probe such scenario, further large sample of detailed H I observation is required. And also, it is important to investigate the molecular clumps of the N48 and N49 regions in more detail, in order to understand whether the filamentary H I gas can be the origin of filamentary molecular clouds like those were seen in the N159W region.

The applicability of the suggested scenarios above to the general GMC formation process also should be checked here. One intersting fact of the N48 and N49 regions is that the entire system of the H I ridge is almost virialized (see §5.2.3). Since H I

clouds are generally not gravitationally bound (e.g., Kim et al. 2007), the H I ridge is somewhat rare case of the H I cloud, that is, the H I gas is efficiently accumulated at certain place with high column density. So the GMC formation via the instability of several times 10 cm^{-3} (not so dense) H I gas is possibly a special case for this region. On the other hand, it is clearly suggested here that the H I envelope of the GMC and the molecular clumps are gravitational bound to them, once the mass and the density of the H I gas are getting high enough to form molecular clouds. This is what Fukui et al. (2009) have proposed from the statistical analysis of the LMC GMCs, and what this work clarified for the specific GMCs. Especially, the features of gravitationally bound H I gas in the molecular clump scale are the one of the important results of this work. For the future works, it is important to see the relationship between the GMC formation process and the effects of the gravitation.

In order to extend the discussion, the next steps are considered as follows. First, the ALMA observation of the molecular clumps in the N48 and N49 regions are quite important to understand the future cluster formation of these clumps. With the GMC formation process in the N48 and N49 region introduced above, sub-pc resolution observation of the N48 and N49 regions will connect the distinct understanding of the GMC formation and the stellar cluster formation, like the N159 study (Fukui et al. 2015a). The ALMA observations of Band 6 (^{12}CO(J=2–1) and ^{13}CO(J=2–1) lines) toward three clumps in the N48 is now coming up to the scheduling block of the ALMA and will be done in this year. Second, detailed analysis of the H I kinematic is required for the other targets. One interesting target is around the 30 Doradus, that is located between two SGSs LMC 2 and LMC 3 (see Figure 1.5). In the area, there are SSC R136, which is the most prominent SSC in the Local Group, and the N159, in which the collision of the filamentary molecular clouds were revealed (Fukui et al. 2015a). There is also the large CO Arc below them. Analyzing this area is crucial to understand the GMC formation and stellar cluster formation. The long baseline ATCA observation (1.5 km) will be done toward these area in 2016 January and February. The similar analysis that is performed in this work will be done for this area.

Chapter 6

Summary of the Thesis

The high column density H I ridge between the two kpc-scale SGSs, LMC4 and LMC 5, is analyzed by high-resolution observation of co and atomic Hydrogen (H I) gas with ASTE, Mopra, and ATCA. The GMC formation process at the colliding area of two SGSs are studied by investigating from the fine-structure to the large-scale kinematics of the H I gas. Main results and suggestions are as follows.

1. ^{12}CO(J=3–2) observations of the ASTE telescope, at a spatial resolution of 7 pc, have revealed that the GMCs in the N48 and N49 regions show highly clumpy structure. In total, 18 and 3 distinct molecular clumps are identified in the N48 and N49 regions respectively.

2. Mean values of the clump physical parameters are $R_{\rm deconv} \sim 4.7$ pc, $\Delta V_{\rm clump} \sim 4.3$ km s^{-1}, $M_{\rm vir} \sim 1.8 \times 10^4$ M$_\odot$, $L_{\rm CO(J=3-2)} \sim 1.2 \times 10^3$ K km s^{-1} pc^2, and $M_{\rm lum,3-2} \sim 1.8 \times 10^4$ M$_\odot$, respectively. These values are smaller than those of clumps observed in the LMC CO Arc with the same instrument (Minamidani et al. 2008).

3. The LVG radiative transfer calculations are performed in order to estimate the density and temperature of 7 clumps in the N48/N49 region, using the CO line intensity rations $R^{13}_{3-2/1-0}$ and $R^{12/13}_{3-2}$. The N4849 clumps are typically warm ($\gtrsim$ 50 K), with moderate density (1–3 $\times 10^3$ cm^{-3}). The N48 clumps are denser and warmer than the N49 clump, but are not as dense as the cluster forming clumps in the LMC (30 Dor and N159), indicates that the clumps are in the early stage of cluster formation.

4. The N48 region is located at the interaction zone of the two SGSs, whereas N49 is associated with LMC 5 alone. The clumps in the N48 region are typically denser and warmer than those in the N49 region, and the star formation activity, as traced by Hα and YSO candidates, seems to be more evolved. This suggests that the formation of massive clumps and stars proceeds more efficiently where the two SGSs are interacting.

5. Data combination of the new long baseline H I 21 cm line observation of ATCA with the archival short baseline data (Mao et al.) and the Parkes single dish data is performed. Achieved beam size is 24.75″ by 20.48″, which is unusually high spatial resolution ($\sim 6 \times 5$ pc) for the 21 cm line in the external galaxy.

6. The H I opacity correction method of Fukui et al. (2014, 2015c) is applied to the H I ridge using the dust opacity data of the Planck Legacy Archive (Planck Collaboration 2013). After the opacity correction, the total mass of the H I ridge is estimated as $\sim 8.5 \times 10^6$ $M_\odot$, which corresponds to roughly 1.7 times increase from the pre-correction data. By solving the radiative transfer equations using these values, the opacity and the spin temperatures are estimated to $\tau_{\rm HI} \gtrsim 1.5$ and $T_S \gtrsim 100$ K.

7. The new observation of the H I reveals that the H I ridge is consist of highly filamentary H I features. By applying Dendrogram to the channel maps, the filamentary features are identified by chaining H I cores by eyes. In total 39 features are identified, implying that the H I gas structure of the ridge mainly consists of the composition of filamentary features. Molecular clumps are associated with the most prominent filamentary feature, indicating that the molecular clumps are typically formed at the evolved filamentary H I gas. Typical width of the filamentary feature is ~ 21 (8–49) [pc], and the line mass is ~ 90 (20–190) [$M_\odot$/pc].

8. The H I position velocity diagrams perpendicular to the ridge show that the axi-symmetric, ellipse-like distribution at the colliding area of the shells (N48 region), and the molecular clouds are found at their central part. This is followed by the three facts. 1) Theoretical model predicts that the pre-collapse density of the ridge is 30–120 cm^{-3}, which is corresponds to the observed mean density. The characteristic separation of the N48 clumps (~ 40 pc) can be explained by the Jeans instability with this initial condition. 2) Since the GMC is roughly in the gravitational equilibrium, the GMC is effectively confined by its gravity, not by the shells. 3) the GMC mass can be explained by the accretion of the H I envelope with the velocity of half the line width. These suggests that the axi-symmetric H I kinematics and the separation of the clumps in the N48 region can be interpreted as the GMC formation via large-scale instability of the shell-shocked medium and the afterward accretion of the H I envelope.

9. The scenario of the GMC formation process in the N48 and N49 regions can be constructed in the large-scale and the high-resolution scale. In the large-scale (> 100 pc scale), the expansion of the two SGSs aggregates the diffuse medium with density of a few cm^{-3} into high column density ridge that mainly consists of the shocked CNM with density of several tens of cm^{-3}. Secondly, the ridge collapses into the GMCs consists of a lot of molecular clumps. And in the current phase, the H I gas around the GMCs is gravitationally bound to the GMCs, and the GMCs are evolving by its accretion until the cluster formation starts. On

the other hand in the high-resolution scale, the structure of the H I gas is getting highly filamentary during its evolution. The molecular clumps are formed along the evolved filamentary H I gas. The H I gas around the molecular clumps are also getting to bound to the clumps, and the H I accretion onto the clumps are now non-negligible. These agree well with the theoretical predicts which are insisting that several times shocks are required to form GMCs, and suggest that the GMC formation involves filamentary nature of the atomic medium.

Acknowledgement

I would like to show my greatest appreciation to Dr. Norikazu Mizuno who gives sincere comments and supports on my work during the Ph-D student. Special thanks also go to Prof. Yasuo Fukui whose suggestions have helped me very much throughout the production of this thesis. I would like to express my gratitude to Dr. Tetsuhiro Minamidani for his long support on the observation and the data reduction of the ASTE, with his IDL codes for the data analysis. I deeply appreciate to Dr. Joanne Dawson on the grateful helps on the ATCA observation and data reduction, and has helpful comments on the paper and this thesis. I also deeply appreciate to Dr. Tsuyoshi Inoue on giving insightful comments on the theoretical aspects of this work. I want to show my appreciation to Dr. Kazufumi Torii on allowing me to use the IDL codes for the H I opacity correction. I would like to thank to Prof. Toshikazu Onishi, Dr. Akiko Kawamura, and Dr. Erik Muller on supporting me with helpful comments and discussions of various scientific aspects.

I would like to thank JSPS KAKENHI (grant Numbers 14J11419) for a grant that made it possible to complete this study. Many thanks to my colleagues and friends, giving me a delightful life during a hard work of the doctor thesis. Finally, I would also like to express my gratitude to my parents for their supports and warm encouragements on all my Ph-D student life.

Bibliography

Abbott, D. C. 1982, ApJ, 263, 723

André, P., Men'shchikov, A., Bontemps, S., Könyves, V., Motte, F., Schneider, N., Didelon, P., Minier, V., Saraceno, P., Ward-Thompson, D., di Francesco, J., White, G., Molinari, S., Testi, L., Abergel, A., Griffin, M., Henning, T., Royer, P., Merín, B., Vavrek, R., Attard, M., Arzoumanian, D., Wilson, C. D., Ade, P., Aussel, H., Baluteau, J.-P., Benedettini, M., Bernard, J.-P., Blommaert, J. A. D. L., Cambrésy, L., Cox, P., di Giorgio, A., Hargrave, P., Hennemann, M., Huang, M., Kirk, J., Krause, O., Launhardt, R., Leeks, S., Le Pennec, J., Li, J. Z., Martin, P. G., Maury, A., Olofsson, G., Omont, A., Peretto, N., Pezzuto, S., Prusti, T., Roussel, H., Russeil, D., Sauvage, M., Sibthorpe, B., Sicilia-Aguilar, A., Spinoglio, L., Waelkens, C., Woodcraft, A., & Zavagno, A. 2010, A&A, 518, L102

Ascenso, J., Alves, J., Beletsky, Y., & Lago, M. T. V. T. 2007, A&A, 466, 137

Audit, E. & Hennebelle, P. 2005, A&A, 433, 1

Ballesteros-Paredes, J., Hartmann, L. W., Vázquez-Semadeni, E., Heitsch, F., & Zamora-Avilés, M. A. 2011, MNRAS, 411, 65

Beuther, H., Henning, T., Linz, H., Feng, S., Ragan, S. E., Smith, R. J., Bihr, S., Sakai, T., & Kuiper, R. 2015, A&A, 581, A119

Bisbas, T. G., Wünsch, R., Whitworth, A. P., Hubber, D. A., & Walch, S. 2011, ApJ, 736, 142

Blitz, L. 1993, in Protostars and Planets III, ed. E. H. Levy & J. I. Lunine, 125–161

Blitz, L., Fukui, Y., Kawamura, A., Leroy, A., Mizuno, N., & Rosolowsky, E. 2007, Protostars and Planets V, 81

Bonnell, I. A., Bate, M. R., Clarke, C. J., & Pringle, J. E. 2001, MNRAS, 323, 785

Book, L. G., Chu, Y.-H., & Gruendl, R. A. 2008, ApJS, 175, 165

Book, L. G., Chu, Y.-H., Gruendl, R. A., & Fukui, Y. 2009, AJ, 137, 3599

Castor, J. I. 1970, MNRAS, 149, 111

Chen, C.-H. R., Chu, Y.-H., Gruendl, R. A., Gordon, K. D., & Heitsch, F. 2009, ApJ, 695, 511

Chernin, A. D., Efremov, Y. N., & Voinovich, P. A. 1995, MNRAS, 275, 313

Chini, R., Reipurth, B., Ward-Thompson, D., Bally, J., Nyman, L.-Å., Sievers, A., & Billawala, Y. 1997, ApJ, 474, L135

Cohen, M., Staveley-Smith, L., & Green, A. 2003, MNRAS, 340, 275

Cohen, R. S., Dame, T. M., Garay, G., Montani, J., Rubio, M., & Thaddeus, P. 1988, ApJ, 331, L95

Combes, F. 1991, ARA&A, 29, 195

Dale, J. E., Haworth, T. J., & Bressert, E. 2015, MNRAS, 450, 1199

Dame, T. M., Ungerechts, H., Cohen, R. S., de Geus, E. J., Grenier, I. A., May, J., Murphy, D. C., Nyman, L.-A., & Thaddeus, P. 1987, ApJ, 322, 706

Davies, R. D., Elliott, K. H., & Meaburn, J. 1976, MmRAS, 81, 89

Dawson, J. R. 2013, PASA, 30, 25

Dawson, J. R., McClure-Griffiths, N. M., Dickey, J. M., & Fukui, Y. 2011, ApJ, 741, 85

Dawson, J. R., McClure-Griffiths, N. M., Wong, T., Dickey, J. M., Hughes, A., Fukui, Y., & Kawamura, A. 2013, ApJ, 763, 56

Dawson, J. R., Ntormousi, E., Fukui, Y., Hayakawa, T., & Fierlinger, K. 2015, ApJ, 799, 64

Deharveng, L., Schuller, F., Anderson, L. D., Zavagno, A., Wyrowski, F., Menten, K. M., Bronfman, L., Testi, L., Walmsley, C. M., & Wienen, M. 2010, A&A, 523, A6

Deharveng, L., Zavagno, A., Anderson, L. D., Motte, F., Abergel, A., André, P., Bontemps, S., Leleu, G., Roussel, H., & Russeil, D. 2012, A&A, 546, A74

Deharveng, L., Zavagno, A., & Caplan, J. 2005, A&A, 433, 565

Desai, K. M., Chu, Y.-H., Gruendl, R. A., Dluger, W., Katz, M., Wong, T., Chen, C.-H. R., Looney, L. W., Hughes, A., Muller, E., Ott, J., & Pineda, J. L. 2010, AJ, 140, 584

Dickey, J. M. & Lockman, F. J. 1990, ARA&A, 28, 215

Dickey, J. M., McClure-Griffiths, N. M., Gaensler, B. M., & Green, A. J. 2003, ApJ, 585, 801

Dobashi, K., Bernard, J.-P., & Fukui, Y. 1996, ApJ, 466, 282

Dobbs, C. L., Krumholz, M. R., Ballesteros-Paredes, J., Bolatto, A. D., Fukui, Y., Heyer, M., Low, M.-M. M., Ostriker, E. C., & Vázquez-Semadeni, E. 2014, Protostars and Planets VI, 3

Dobbs, C. L. & Pringle, J. E. 2013, MNRAS, 432, 653

Domgoergen, H., Bomans, D. J., & de Boer, K. S. 1995, A&A, 296, 523

Dopita, M. A., Mathewson, D. S., & Ford, V. L. 1985, ApJ, 297, 599

Dufour, R. J. Structure and Evolution of the Magellanic Clouds, ed. S. van den Bergh and K. S. de Boer (Dordrecht: Reidel), 353

Efremov, Y. N. & Elmegreen, B. G. 1998, MNRAS, 299, 643

Efremov, Y. N., Elmegreen, B. G., & Hodge, P. W. 1998, ApJ, 501, L163

Elmegreen, B. G. 1979, ApJ, 231, 372

—. 1995, MNRAS, 275, 944

Elmegreen, B. G. 1998, in Astronomical Society of the Pacific Conference Series, Vol. 148, Origins, ed. C. E. Woodward, J. M. Shull, & H. A. Thronson, Jr., 150

Elmegreen, B. G. & Lada, C. J. 1977, ApJ, 214, 725

Emerson, D. T. & Graeve, R. 1988, A&A, 190, 353

Ezawa, H., Kawabe, R., Kohno, K., & Yamamoto, S. 2004, in Society of Photo-Optical Instrumentation Engineers (SPIE) Conference Series, Vol. 5489, Society of Photo-Optical Instrumentation Engineers (SPIE) Conference Series, ed. J. M. Oschmann, Jr., 763–772

Ezawa, H., Kohno, K., Kawabe, R., Yamamoto, S., Inoue, H., Iwashita, H., Matsuo, H., Okuda, T., Oshima, T., Sakai, T., Tanaka, K., Yamaguchi, N., Wilson, G. W., Yun, M. S., Aretxaga, I., Hughes, D., Austermann, J., Perera, T. A., Scott, K. S., Bronfman, L., & Cortes, J. R. 2008, in Society of Photo-Optical Instrumentation Engineers (SPIE) Conference Series, Vol. 7012, Society of Photo-Optical Instrumentation Engineers (SPIE) Conference Series

Field, G. B. & Saslaw, W. C. 1965, ApJ, 142, 568

Filipovic, M. D., Haynes, R. F., White, G. L., & Jones, P. A. 1998, A&AS, 130, 421

Fixsen, D. J. 2009, ApJ, 707, 916

Fujii, K., Minamidani, T., Mizuno, N., Onishi, T., Kawamura, A., Muller, E., Dawson, J., Tatematsu, K., Hasegawa, T., Tosaki, T., Miura, R. E., Muraoka, K., Sakai, T., Tsukagoshi, T., Tanaka, K., Ezawa, H., & Fukui, Y. 2014, ApJ, 796, 123

Fukui, Y., Harada, R., Tokuda, K., Morioka, Y., Onishi, T., Torii, K., Ohama, A., Hattori, Y., Nayak, O., Meixner, M., Sewiło, M., Indebetouw, R., Kawamura, A., Saigo, K., Yamamoto, H., Tachihara, K., Minamidani, T., Inoue, T., Madden, S., Galametz, M., Lebouteiller, V., Mizuno, N., & Chen, C.-H. R. 2015a, ApJ, 807, L4

Fukui, Y. & Kawamura, A. 2010, ARA&A, 48, 547

Fukui, Y., Kawamura, A., Minamidani, T., Mizuno, Y., Kanai, Y., Mizuno, N., Onishi, T., Yonekura, Y., Mizuno, A., Ogawa, H., & Rubio, M. 2008, ApJS, 178, 56

Fukui, Y., Kawamura, A., Wong, T., Murai, M., Iritani, H., Mizuno, N., Mizuno, Y., Onishi, T., Hughes, A., Ott, J., Muller, E., Staveley-Smith, L., & Kim, S. 2009, ApJ, 705, 144

Fukui, Y., Mizuno, N., Yamaguchi, R., Mizuno, A., Onishi, T., Ogawa, H., Yonekura, Y., Kawamura, A., Tachihara, K., Xiao, K., Yamaguchi, N., Hara, A., Hayakawa, T., Kato, S., Abe, R., Saito, H., Mano, S., Matsunaga, K., Mine, Y., Moriguchi, Y., Aoyama, H., Asayama, S.-i., Yoshikawa, N., & Rubio, M. 1999, PASJ, 51, 745

Fukui, Y., Okamoto, R., Kaji, R., Yamamoto, H., Torii, K., Hayakawa, T., Tachihara, K., Dickey, J. M., Okuda, T., Ohama, A., Kuroda, Y., & Kuwahara, T. 2014, ApJ, 796, 59

Fukui, Y., Torii, K., Ohama, A., Hasegawa, K., Hattori, Y., Sano, H., Ohashi, S., Fujii, K., Kuwahara, S., Mizuno, N., Dawson, J. R., Yamamoto, H., Tachihara, K., Okuda, T., Onishi, T., & Mizuno, A. 2015b, ArXiv e-prints

Fukui, Y., Torii, K., Onishi, T., Yamamoto, H., Okamoto, R., Hayakawa, T., Tachihara, K., & Sano, H. 2015c, ApJ, 798, 6

Furukawa, N., Dawson, J. R., Ohama, A., Kawamura, A., Mizuno, N., Onishi, T., & Fukui, Y. 2009, ApJ, 696, L115

Genzel, R. & Stutzki, J. 1989, ARA&A, 27, 41

Glatt, K., Grebel, E. K., & Koch, A. 2010, A&A, 517, A50

Goldreich, P. & Kwan, J. 1974, ApJ, 189, 441

Goldsmith, P. 1987, Interstellar Processes, D Reidel Publishing Co.

Goodman, A. A., Rosolowsky, E. W., Borkin, M. A., Foster, J. B., Halle, M., Kauffmann, J., & Pineda, J. E. 2009, Nature, 457, 63

Gruendl, R. A. & Chu, Y.-H. 2009, ApJS, 184, 172

Hartmann, L., Ballesteros-Paredes, J., & Bergin, E. A. 2001, ApJ, 562, 852

Haworth, T. J. & Harries, T. J. 2012, MNRAS, 420, 562

Heiles, C. & Troland, T. H. 2003a, ApJS, 145, 329

—. 2003b, ApJ, 586, 1067

Heitsch, F., Burkert, A., Hartmann, L. W., Slyz, A. D., & Devriendt, J. E. G. 2005, ApJ, 633, L113

Heitsch, F., Slyz, A. D., Devriendt, J. E. G., Hartmann, L. W., & Burkert, A. 2006, ApJ, 648, 1052

Heitsch, F., Stone, J. M., & Hartmann, L. W. 2009, ApJ, 695, 248

Helfer, T. T., Thornley, M. D., Regan, M. W., Wong, T., Sheth, K., Vogel, S. N., Blitz, L., & Bock, D. C.-J. 2003, ApJS, 145, 259

Henize, K. G. 1956, ApJS, 2, 315

Hennebelle, P. & Audit, E. 2007, A&A, 465, 431

Hennebelle, P. & Pérault, M. 1999, A&A, 351, 309

Heyer, M., Krawczyk, C., Duval, J., & Jackson, J. M. 2009, ApJ, 699, 1092

Hilditch, R. W., Howarth, I. D., & Harries, T. J. 2005, MNRAS, 357, 304

Hodge, P. W. 1961, ApJ, 133, 413

Hosokawa, T. & Inutsuka, S.-i. 2006, ApJ, 646, 240

Hughes, A., Meidt, S. E., Colombo, D., Schinnerer, E., Pety, J., Leroy, A. K., Dobbs, C. L., García-Burillo, S., Thompson, T. A., Dumas, G., Schuster, K. F., & Kramer, C. 2013, ApJ, 779, 46

Hughes, A., Wong, T., Ott, J., Muller, E., Pineda, J. L., Mizuno, Y., Bernard, J.-P., Paradis, D., Maddison, S., Reach, W. T., Staveley-Smith, L., Kawamura, A., Meixner, M., Kim, S., Onishi, T., Mizuno, N., & Fukui, Y. 2010, MNRAS, 406, 2065

Hunter, D. A., Shaya, E. J., Holtzman, J. A., Light, R. M., O'Neil, Jr., E. J., & Lynds, R. 1995, ApJ, 448, 179

Inoue, H., Muraoka, K., Sakai, T., Endo, A., Kohno, K., Asayama, S., Noguchi, T., & Ogawa, H. 2008, in Ninteenth International Symposium on Space Terahertz Technology, ed. W. Wild, 281

Inoue, T. & Fukui, Y. 2013, ApJ, 774, L31

Inoue, T. & Inutsuka, S.-i. 2008, ApJ, 687, 303

—. 2009, ApJ, 704, 161

—. 2012, ApJ, 759, 35

Inutsuka, S.-i., Inoue, T., Iwasaki, K., & Hosokawa, T. 2015, A&A, 580, A49

Inutsuka, S.-I., Koyama, H., & Inoue, T. 2005, in American Institute of Physics Conference Series, Vol. 784, Magnetic Fields in the Universe: From Laboratory and Stars to Primordial Structures., ed. E. M. de Gouveia dal Pino, G. Lugones, & A. Lazarian, 318–328

Inutsuka, S.-I. & Miyama, S. M. 1992, ApJ, 388, 392

Kalberla, P. M. W. & Kerp, J. 2009, ARA&A, 47, 27

Kalberla, P. M. W., McClure-Griffiths, N. M., Pisano, D. J., Calabretta, M. R., Ford, H. A., Lockman, F. J., Staveley-Smith, L., Kerp, J., Winkel, B., Murphy, T., & Newton-McGee, K. 2010, A&A, 521, A17

Kauffmann, J., Pillai, T., & Zhang, Q. 2013, ApJ, 765, L35

Kawamura, A., Mizuno, Y., Minamidani, T., Filipović, M. D., Staveley-Smith, L., Kim, S., Mizuno, N., Onishi, T., Mizuno, A., & Fukui, Y. 2009, ApJS, 184, 1

Kawamura, A., Onishi, T., Yonekura, Y., Dobashi, K., Mizuno, A., Ogawa, H., & Fukui, Y. 1998, ApJS, 117, 387

Kim, S., Dopita, M. A., Staveley-Smith, L., & Bessell, M. S. 1999, AJ, 118, 2797

Kim, S., Rosolowsky, E., Lee, Y., Kim, Y., Jung, Y. C., Dopita, M. A., Elmegreen, B. G., Freeman, K. C., Sault, R. J., Kesteven, M., McConnell, D., & Chu, Y.-H. 2007, ApJS, 171, 419

Kim, S., Staveley-Smith, L., Dopita, M. A., Freeman, K. C., Sault, R. J., Kesteven, M. J., & McConnell, D. 1998, ApJ, 503, 674

Kim, S., Staveley-Smith, L., Dopita, M. A., Sault, R. J., Freeman, K. C., Lee, Y., & Chu, Y.-H. 2003, ApJS, 148, 473

Kim, W.-T. & Ostriker, E. C. 2006, ApJ, 646, 213

Kim, W.-T., Ostriker, E. C., & Stone, J. M. 2002, ApJ, 581, 1080

Kohno, K. 2005, in Astronomical Society of the Pacific Conference Series, Vol. 344, The Cool Universe: Observing Cosmic Dawn, ed. C. Lidman & D. Alloin, 242

Koyama, H. & Inutsuka, S.-I. 2000, ApJ, 532, 980

Koyama, H. & Inutsuka, S.-i. 2002, ApJ, 564, L97

Kutner, M. L., Tucker, K. D., Chin, G., & Thaddeus, P. 1977, ApJ, 215, 521

Kwan, J. 1979, ApJ, 229, 567

Ladd, N., Purcell, C., Wong, T., & Robertson, S. 2005, PASA, 22, 62

Larson, R. B. 1981, MNRAS, 194, 809

Lee, K. I., Fernández-López, M., Storm, S., Looney, L. W., Mundy, L. G., Segura-Cox, D., Teuben, P., Rosolowsky, E., Arce, H. G., Ostriker, E. C., Shirley, Y. L., Kwon, W., Kauffmann, J., Tobin, J. J., Plunkett, A. L., Pound, M. W., Salter, D. M., Volgenau, N. H., Chen, C.-Y., Tassis, K., Isella, A., Crutcher, R. M., Gammie, C. F., & Testi, L. 2014, ApJ, 797, 76

Leroy, A. K., Bolatto, A., Gordon, K., Sandstrom, K., Gratier, P., Rosolowsky, E., Engelbracht, C. W., Mizuno, N., Corbelli, E., Fukui, Y., & Kawamura, A. 2011, ApJ, 737, 12

Lucke, P. B. & Hodge, P. W. 1970, AJ, 75, 171

Luks, T. & Rohlfs, K. 1992, A&A, 263, 41

Mac Low, M.-M. & Ferrara, A. 1999, ApJ, 513, 142

MacLaren, I., Richardson, K. M., & Wolfendale, A. W. 1988, ApJ, 333, 821

Maddalena, R. J., Morris, M., Moscowitz, J., & Thaddeus, P. 1986, ApJ, 303, 375

Martin, P. G., Blagrave, K. P. M., Lockman, F. J., Pinheiro Gonçalves, D., Boothroyd, A. I., Joncas, G., Miville-Deschênes, M.-A., & Stephan, G. 2015, ApJ, 809, 153

Marx-Zimmer, M., Herbstmeier, U., Dickey, J. M., Zimmer, F., Staveley-Smith, L., & Mebold, U. 2000, A&A, 354, 787

Massey, P. & Hunter, D. A. 1998, ApJ, 493, 180

McClure-Griffiths, N. M., Dickey, J. M., Gaensler, B. M., & Green, A. J. 2002, ApJ, 578, 176

—. 2003, ApJ, 594, 833

McClure-Griffiths, N. M., Dickey, J. M., Gaensler, B. M., Green, A. J., Haynes, R. F., & Wieringa, M. H. 2000, AJ, 119, 2828

McClure-Griffiths, N. M., Pisano, D. J., Calabretta, M. R., Ford, H. A., Lockman, F. J., Staveley-Smith, L., Kalberla, P. M. W., Bailin, J., Dedes, L., Janowiecki, S., Gibson, B. K., Murphy, T., Nakanishi, H., & Newton-McGee, K. 2009, ApJS, 181, 398

McCray, R. & Kafatos, M. 1987, ApJ, 317, 190

McKee, C. F. & Ostriker, E. C. 2007, ARA&A, 45, 565

McKee, C. F. & Tan, J. C. 2003, ApJ, 585, 850

McLaughlin, D. E. & Pudritz, R. E. 1996, ApJ, 469, 194

Meaburn, J. 1980, MNRAS, 192, 365

Megeath, S. T., Gutermuth, R., Muzerolle, J., Kryukova, E., Flaherty, K., Hora, J. L., Allen, L. E., Hartmann, L., Myers, P. C., Pipher, J. L., Stauffer, J., Young, E. T., & Fazio, G. G. 2012, AJ, 144, 192

Meixner, M., Gordon, K. D., Indebetouw, R., Hora, J. L., Whitney, B., Blum, R., Reach, W., Bernard, J.-P., Meade, M., Babler, B., Engelbracht, C. W., For, B.-Q., Misselt, K., Vijh, U., Leitherer, C., Cohen, M., Churchwell, E. B., Boulanger, F., Frogel, J. A., Fukui, Y., Gallagher, J., Gorjian, V., Harris, J., Kelly, D., Kawamura, A., Kim, S., Latter, W. B., Madden, S., Markwick-Kemper, C., Mizuno, A., Mizuno, N., Mould, J., Nota, A., Oey, M. S., Olsen, K., Onishi, T., Paladini, R., Panagia, N., Perez-Gonzalez, P., Shibai, H., Sato, S., Smith, L., Staveley-Smith, L., Tielens, A. G. G. M., Ueta, T., van Dyk, S., Volk, K., Werner, M., & Zaritsky, D. 2006, AJ, 132, 2268

Meixner, M., Panuzzo, P., Roman-Duval, J., Engelbracht, C., Babler, B., Seale, J., Hony, S., Montiel, E., Sauvage, M., Gordon, K., Misselt, K., Okumura, K., Chanial, P., Beck, T., Bernard, J.-P., Bolatto, A., Bot, C., Boyer, M. L., Carlson, L. R., Clayton, G. C., Chen, C.-H. R., Cormier, D., Fukui, Y., Galametz, M., Galliano, F., Hora, J. L., Hughes, A., Indebetouw, R., Israel, F. P., Kawamura, A., Kemper, F., Kim, S., Kwon, E., Lebouteiller, V., Li, A., Long, K. S., Madden, S. C., Matsuura, M., Muller, E., Oliveira, J. M., Onishi, T., Otsuka, M., Paradis, D., Poglitsch, A., Reach, W. T., Robitaille, T. P., Rubio, M., Sargent, B., Sewiło, M., Skibba, R., Smith, L. J., Srinivasan, S., Tielens, A. G. G. M., van Loon, J. T., & Whitney, B. 2013, AJ, 146, 62

Meynet, G. & Maeder, A. 2000, A&A, 361, 101

Minamidani, T., Mizuno, N., Y., M., Kawamura, A., Onishi, T., Hasegawa, T., Tatematsu, K., Ikeda, M., Moriguchi, Y., Yamaguchi, N., Ott, J., Wong, T., Muller, E., Pineda, J. L., Hughes, A., Staveley-Smith, L., Klein, U., Mizuno, A., Nikolić, S., Booth, R. S., Heikkilä, A., Nyman, L.-Å., Lerner, M., Garay, G., Kim, S., Fujishita, M., Kawase, T., Rubio, M., & Fukui, Y. 2008, ApJS, 175, 485

Minamidani, T., Tanaka, T., Mizuno, Y., Mizuno, N., Kawamura, A., Onishi, T., Hasegawa, T., Tatematsu, K., Takekoshi, T., Sorai, K., Moribe, N., Torii, K., Sakai, T., Muraoka, K., Tanaka, K., Ezawa, H., Kohno, K., Kim, S., Rubio, M., & Fukui, Y. 2011, AJ, 141, 73

Miocchi, P., Lanzoni, B., Ferraro, F. R., Dalessandro, E., Vesperini, E., Pasquato, M., Beccari, G., Pallanca, C., & Sanna, N. 2013, ApJ, 774, 151

Miura, R. E., Kohno, K., Tosaki, T., Espada, D., Hwang, N., Kuno, N., Okumura, S. K., Hirota, A., Muraoka, K., Onodera, S., Minamidani, T., Komugi, S., Nakanishi, K., Sawada, T., Kaneko, H., & Kawabe, R. 2012, ApJ, 761, 37

Mizuno, A., Onishi, T., Yonekura, Y., Nagahama, T., Ogawa, H., & Fukui, Y. 1995, ApJ, 445, L161

Mizuno, N., Yamaguchi, R., Mizuno, A., Rubio, M., Abe, R., Saito, H., Onishi, T., Yonekura, Y., Yamaguchi, N., Ogawa, H., & Fukui, Y. 2001, PASJ, 53, 971

Mizuno, Y., Kawamura, A., Onishi, T., Minamidani, T., Muller, E., Yamamoto, H., Hayakawa, T., Mizuno, N., Mizuno, A., Stutzki, J., Pineda, J. L., Klein, U., Bertoldi, F., Koo, B.-C., Rubio, M., Burton, M., Benz, A., Ezawa, H., Yamaguchi, N., Kohno, K., Hasegawa, T., Tatematsu, K., Ikeda, M., Ott, J., Wong, T., Hughes, A., Meixner, M., Indebetouw, R., Gordon, K. D., Whitney, B., Bernard, J.-P., & Fukui, Y. 2010, PASJ, 62, 51

Nagasawa, M. 1987, Progress of Theoretical Physics, 77, 635

Nakamura, F., Hanawa, T., & Nakano, T. 1993, PASJ, 45, 551

Nakamura, F., Sugitani, K., Tanaka, T., Nishitani, H., Dobashi, K., Shimoikura, T., Shimajiri, Y., Kawabe, R., Yonekura, Y., Mizuno, I., Kimura, K., Tokuda, K., Kozu, M., Okada, N., Hasegawa, Y., Ogawa, H., Kameno, S., Shinnaga, H., Momose, M., Nakajima, T., Onishi, T., Maezawa, H., Hirota, T., Takano, S., Iono, D., Kuno, N., & Yamamoto, S. 2014, ApJ, 791, L23

Nishimura, A., Tokuda, K., Kimura, K., Muraoka, K., Maezawa, H., Ogawa, H., Dobashi, K., Shimoikura, T., Mizuno, A., Fukui, Y., & Onishi, T. 2015, ApJS, 216, 18

Ntormousi, E., Burkert, A., Fierlinger, K., & Heitsch, F. 2011, ApJ, 731, 13

Ohama, A., Dawson, J. R., Furukawa, N., Kawamura, A., Moribe, N., Yamamoto, H., Okuda, T., Mizuno, N., Onishi, T., Maezawa, H., Minamidani, T., Mizuno, A., & Fukui, Y. 2010, ApJ, 709, 975

Ostriker, J. 1964, ApJ, 140, 1056

Parker, E. N. 1966, ApJ, 145, 811

Peretto, N., Fuller, G. A., Duarte-Cabral, A., Avison, A., Hennebelle, P., Pineda, J. E., André, P., Bontemps, S., Motte, F., Schneider, N., & Molinari, S. 2013, A&A, 555, A112

Piatti, A. E., Bica, E., & Claria, J. J. 1998, A&AS, 127, 423

Pietrzyński, G., Graczyk, D., Gieren, W., Thompson, I. B., Pilecki, B., Udalski, A., Soszyński, I., Kozłowski, S., Konorski, P., Suchomska, K., Bono, G., Moroni, P. G. P., Villanova, S., Nardetto, N., Bresolin, F., Kudritzki, R. P., Storm, J., Gallenne, A., Smolec, R., Minniti, D., Kubiak, M., Szymański, M. K., Poleski, R., Wyrzykowski, Ł., Ulaczyk, K., Pietrukowicz, P., Górski, M., & Karczmarek, P. 2013, Nature, 495, 76

Pirogov, L., Ojha, D. K., Thomasson, M., Wu, Y.-F., & Zinchenko, I. 2013, MNRAS, 436, 3186

Planck Collaboration. 2013, Planck Explanatory Supplement (Public Release 1; Noordwijk: ESA), http://wiki.cosmos.esa.int/planckpla/index.php/Main_Page

Points, S. D., Chu, Y. H., Kim, S., Smith, R. C., Snowden, S. L., Brandner, W., & Gruendl, R. A. 1999, ApJ, 518, 298

Rieke, G. H., Young, E. T., Cadien, J., Engelbracht, C. W., Gordon, K. D., Kelly, D. M., Low, F. J., Misselt, K. A., Morrison, J. E., Muzerolle, J., Rivlis, G., Stansberry, J. A., Beeman, J. W., Haller, E. E., Frayer, D. T., Latter, W. B., Noriega-Crespo, A., Padgett, D. L., Hines, D. C., Bean, J. D., Burmester, W., Heim, G. B., Glenn, T., Ordonez, R., Schwenker, J. P., Siewert, S., Strecker, D. W., Tennant, S., Troeltzsch, J. R., Unruh, B., Warden, R. M., Ade, P. A., Alonso-Herrero, A., Blaylock, M., Dole, H., Egami, E., Hinz, J. L., Le Floc'h, E., Papovich, C., Perez-Gonzalez, P. G., Rieke, M. J., Smith, P. S., Su, K. Y. L., Bennett, L., Henderson, D., Lu, N., Masci, F. J., Pesenson, M., Rebull, L., Rho, J., Keene, J., Stolovy, S., Wachter, S., Wheaton, W., Richards, P. L., Garner, H. W., Hegge, M., Henderson, M. L., MacFeely, K. I., Michika, D., Miller, C. D., Neitenbach, M., Winghart, J., Woodruff, R., Arens, E., Beichman, C. A., Gaalema, S. D., Gautier, III, T. N., Lada, C. J., Mould, J., Neugebauer, G. X., & Stapelfeldt, K. R. 2004, in Society of Photo-Optical Instrumentation Engineers (SPIE) Conference Series, Vol. 5487, Society of Photo-Optical Instrumentation Engineers (SPIE) Conference Series, ed. J. C. Mather, 50–61

Roberts, M. S. 1957, PASP, 69, 59

Rosolowsky, E. W., Pineda, J. E., Kauffmann, J., & Goodman, A. A. 2008, ApJ, 679, 1338

Sault, R. J. & Killeen, N. E. B. 2009, The MIRIAD User's Guide (Sydney: Australia Telescope National Facility)

Sault, R. J., Staveley-Smith, L., & Brouw, W. N. 1996, A&AS, 120, 375

Sawada, T., Hasegawa, T., & Koda, J. 2012, ApJ, 759, L26

Sawada, T., Ikeda, N., Sunada, K., Kuno, N., Kamazaki, T., Morita, K.-I., Kurono, Y., Koura, N., Abe, K., Kawase, S., Maekawa, J., Horigome, O., & Yanagisawa, K. 2008, PASJ, 60, 445

Schinnerer, E., Meidt, S. E., Pety, J., Hughes, A., Colombo, D., García-Burillo, S., Schuster, K. F., Dumas, G., Dobbs, C. L., Leroy, A. K., Kramer, C., Thompson, T. A., & Regan, M. W. 2013, ApJ, 779, 42

Schöier, F. L., van der Tak, F. F. S., van Dishoeck, E. F., & Black, J. H. 2005, A&A, 432, 369

Scoville, N. Z. & Solomon, P. M. 1974, ApJ, 187, L67

Seale, J. P., Looney, L. W., Wong, T., Ott, J., Klein, U., & Pineda, J. L. 2012, ApJ, 751, 42

Shu, F. H. 1974, A&A, 33, 55

Smith, R. C. & MCELS Team. 1999, in IAU Symposium, Vol. 190, New Views of the Magellanic Clouds, ed. Y.-H. Chu, N. Suntzeff, J. Hesser, & D. Bohlender, 28

Solomon, P. M., Rivolo, A. R., Barrett, J., & Yahil, A. 1987, ApJ, 319, 730

Sorai, K., Sunada, K., Okumura, S. K., Tetsuro, I., Tanaka, A., Natori, K., & Onuki, H. 2000, in Society of Photo-Optical Instrumentation Engineers (SPIE) Conference Series, Vol. 4015, Society of Photo-Optical Instrumentation Engineers (SPIE) Conference Series, ed. H. R. Butcher, 86–95

Stark, A. A. & Lee, Y. 2006, ApJ, 641, L113

Staveley-Smith, L., Kim, S., Calabretta, M. R., Haynes, R. F., & Kesteven, M. J. 2003, MNRAS, 339, 87

Storm, S., Mundy, L. G., Fernández-López, M., Lee, K. I., Looney, L. W., Teuben, P., Rosolowsky, E., Arce, H. G., Ostriker, E. C., Segura-Cox, D. M., Pound, M. W., Salter, D. M., Volgenau, N. H., Shirley, Y. L., Chen, C.-Y., Gong, H., Plunkett, A. L., Tobin, J. J., Kwon, W., Isella, A., Kauffmann, J., Tassis, K., Crutcher, R. M., Gammie, C. F., & Testi, L. 2014, ApJ, 794, 165

Takahashi, S., Ho, P. T. P., Teixeira, P. S., Zapata, L. A., & Su, Y.-N. 2013, ApJ, 763, 57

Tan, J. C., Kong, S., Butler, M. J., Caselli, P., & Fontani, F. 2013, ApJ, 779, 96

Tasker, E. J. & Tan, J. C. 2009, ApJ, 700, 358

Taylor, A. R., Gibson, S. J., Peracaula, M., Martin, P. G., Landecker, T. L., Brunt, C. M., Dewdney, P. E., Dougherty, S. M., Gray, A. D., Higgs, L. A., Kerton, C. R., Knee, L. B. G., Kothes, R., Purton, C. R., Uyaniker, B., Wallace, B. J., Willis, A. G., & Durand, D. 2003, AJ, 125, 3145

Tenorio-Tagle, G. 1981, A&A, 94, 338

Tenorio-Tagle, G. & Bodenheimer, P. 1988, ARA&A, 26, 145

Torii, K., Enokiya, R., Sano, H., Yoshiike, S., Hanaoka, N., Ohama, A., Furukawa, N., Dawson, J. R., Moribe, N., Oishi, K., Nakashima, Y., Okuda, T., Yamamoto, H., Kawamura, A., Mizuno, N., Maezawa, H., Onishi, T., Mizuno, A., & Fukui, Y. 2011, ApJ, 738, 46

Torii, K., Hasegawa, K., Hattori, Y., Sano, H., Ohama, A., Yamamoto, H., Tachihara, K., Soga, S., Shimizu, S., Okuda, T., Mizuno, N., Onishi, T., Mizuno, A., & Fukui, Y. 2015, ApJ, 806, 7

Tsuboi, M., Miyazaki, A., & Uehara, K. 2015, PASJ

Vallenari, A., Bomans, D. J., & de Boer, K. S. 1993, A&A, 268, 137

van der Marel, R. P. & Cioni, M.-R. L. 2001, AJ, 122, 1807

van der Marel, R. P. & Kallivayalil, N. 2014, ApJ, 781, 121

Wada, K., Spaans, M., & Kim, S. 2000, ApJ, 540, 797

Walter, F. & Brinks, E. 1999, AJ, 118, 273

Wang, K., Zhang, Q., Testi, L., van der Tak, F., Wu, Y., Zhang, H., Pillai, T., Wyrowski, F., Carey, S., Ragan, S. E., & Henning, T. 2014, MNRAS, 439, 3275

Wang, P., Li, Z.-Y., Abel, T., & Nakamura, F. 2010, ApJ, 709, 27

Weaver, R., McCray, R., Castor, J., Shapiro, P., & Moore, R. 1977, ApJ, 218, 377

Weisz, D. R., Skillman, E. D., Cannon, J. M., Walter, F., Brinks, E., Ott, J., & Dolphin, A. E. 2009, ApJ, 691, L59

White, G. J., Nelson, R. P., Holland, W. S., Robson, E. I., Greaves, J. S., McCaughrean, M. J., Pilbratt, G. L., Balser, D. S., Oka, T., Sakamoto, S., Hasegawa, T., McCutcheon, W. H., Matthews, H. E., Fridlund, C. V. M., Tothill, N. F. H., Huldtgren, M., & Deane, J. R. 1999, A&A, 342, 233

Whitney, B. A., Sewilo, M., Indebetouw, R., Robitaille, T. P., Meixner, M., Gordon, K., Meade, M. R., Babler, B. L., Harris, J., Hora, J. L., Bracker, S., Povich, M. S., Churchwell, E. B., Engelbracht, C. W., For, B.-Q., Block, M., Misselt, K., Vijh, U., Leitherer, C., Kawamura, A., Blum, R. D., Cohen, M., Fukui, Y., Mizuno, A., Mizuno, N., Srinivasan, S., Tielens, A. G. G. M., Volk, K., Bernard, J.-P., Boulanger, F., Frogel, J. A., Gallagher, J., Gorjian, V., Kelly, D., Latter, W. B., Madden, S., Kemper, F., Mould, J. R., Nota, A., Oey, M. S., Olsen, K. A., Onishi, T., Paladini, R., Panagia, N., Perez-Gonzalez, P., Reach, W., Shibai, H., Sato, S., Smith, L. J., Staveley-Smith, L., Ueta, T., Van Dyk, S., Werner, M., Wolff, M., & Zaritsky, D. 2008, AJ, 136, 18

Will, J.-M., Bomans, D. J., Vallenari, A., Schmidt, J. H. K., & de Boer, K. S. 1996, A&A, 315, 125

Wilson, B. A., Dame, T. M., Masheder, M. R. W., & Thaddeus, P. 2005, A&A, 430, 523

Wolfire, M. G. & Cassinelli, J. P. 1987, ApJ, 319, 850

Wong, T., Hughes, A., Ott, J., Muller, E., Pineda, J. L., Bernard, J.-P., Chu, Y.-H., Fukui, Y., Gruendl, R. A., Henkel, C., Kawamura, A., Klein, U., Looney, L. W., Maddison, S., Mizuno, Y., Paradis, D., Seale, J., & Welty, D. E. 2011, ApJS, 197, 16

Yamaguchi, R., Mizuno, N., Onishi, T., Mizuno, A., & Fukui, Y. 2001a, ApJ, 553, L185

—. 2001b, PASJ, 53, 959

Yamaguchi, R., Saito, H., Mizuno, N., Mine, Y., Mizuno, A., Ogawa, H., & Fukui, Y. 1999, PASJ, 51, 791

Yonekura, Y., Dobashi, K., Mizuno, A., Ogawa, H., & Fukui, Y. 1997, ApJS, 110, 21